The Dissertation Committee for Brent Michael Covele Certifies that this is the approved version of the following dissertation:

2-D Magnetic Equilibrium and Transport Modeling of the X-Divertor and Super X-Divertor for Scrape-Off Layer Heat Flux Mitigation in Tokamaks

Committee:

Swadesh M. Mahajan, Co-supervisor

Kenneth W. Gentle, Co-supervisor

Roger D. Bengtson

Richard Fitzpatrick

Gary A. Hallock

2-D Magnetic Equilibrium and Transport Modeling of the X-Divertor and Super X-Divertor for Scrape-Off Layer Heat Flux Mitigation in Tokamaks

by

Brent Michael Covele, B.S.

Dissertation

Presented to the Faculty of the Graduate School of

The University of Texas at Austin

in Partial Fulfillment

of the Requirements

for the Degree of

Doctor of Philosophy

The University of Texas at Austin

August 2014

Acknowledgements

There is no shortage of people to thank for making the completion of this dissertation and degree possible. First and foremost, to Swadesh Mahajan, Mike Kotschenreuther, and Prashant Valanju (UT-Austin), thank you for tirelessly lending your time and expertise so that I could become an asset to fusion research. Thanks to John Canik (ORNL) and Xavier Bonnin (CNRS-LSPM), who spent many hours in painstaking email collaboration with an irritatingly persistent graduate student. And thanks to the U.S. Department of Energy, whose grants made this research possible.

Of course, this career path started more than just a few years ago. A vigorous round of applause goes to Becky Kehler and Rich Perry at Greenwood Community High School (Greenwood, IN), whose unwavering enthusiasm and dedication to their work inspired me, and provided a top-notch science education unavailable to many other students of public schools. My profound appreciation goes to my horde of insanely dedicated friends, especially those in φφκα, who have been my emotional support network through all of this. Thanks to my loving boyfriend, who reminds me on a near-daily basis why I do what I do. And finally, my sincerest thanks go to my mother, because while she probably won't get past the first page of this tome, she has never failed to support me and my brothers with an ironclad sense of duty and love.

2-D Magnetic Equilibrium and Transport Modeling of the X-Divertor and Super X-Divertor for Scrape-Off Layer Heat Flux Mitigation in Tokamaks

Brent Michael Covele, Ph.D.

The University of Texas at Austin, 2014

Supervisors: Swadesh Mahajan and Kenneth Gentle

Intense heat fluxes from the divertor incident on material surfaces represent a "bottleneck" problem for the next generation of tokamaks. Advanced divertors, such as the X-Divertor (XD) and Super X-Divertor (SXD), offer a magnetic solution to the heat flux problem by (a) increasing the plasma-wetted area via flux expansion at the targets, and (b) possibly opening regimes of stable, detached operation of the divertor via flux tube flaring, as quantified by the Divertor Index. The benefits of the XD and SXD are derived from their unique magnetic geometries, foregoing the need for excessive gas puffing or impurity injection to mitigate divertor heat fluxes. Using the CORSICA magnetic equilibrium code, XDs and SXDs appear feasible on current- and next-generation tokamaks, with no required changes to the tokamak hardware, and respecting coil conductor limits. Divertor heat and particle transport modeling is performed in SOLPS 5.1 for XD or SXD designs in NSTX-Upgrade, Alcator C-Mod, and CFNS/FNSF. Incident heat fluxes at the targets are kept well below 10 MW/m^2, even for narrow SOL widths in high-power scenarios. In C-Mod and CFNS, parallel temperature profiles imply the arrestment of the detachment front near the targets. Finally, an X-Divertor for ITER is presented.

Table of Contents

I. AN OVERVIEW OF ADVANCED DIVERTOR APPLICATIONS IN TOKAMAKS

Since the 1950s, the tokamak has been the flagship device on the path to a fusion reactor and economical fusion energy (see Appendix A). Today's generation of tokamak experiments use powerful magnetic fields produced by poloidal field (PF) coils and toroidal field (TF) coils to confine a relatively low-density (n_e ~10^{20} m^{-3}), high-temperature (T_e ~10 keV) hydrogen plasma for a time on the order of seconds. In a reactor, this plasma would be confined at a sufficiently high triple product ($nT\tau_E$) such that fusion of the ions could take place. Because exhaust plasma from the tokamak core is both inevitable from anomalous transport and necessary for helium ash removal, the divertor was introduced to mitigate its intense heat loads and to keep them from the tokamak walls. Volume I presents a narrative on the exhaust heat problem posed by the tokamak divertor, and the promise that advanced divertors like the X-Divertor, Super X-Divertor, and Snowflake Divertor hold to address this problem.

Chapter 1:

The Tokamak Heat Flux Problem

1.1. The Diverted Plasma and the Discovery of the H-Mode

At the onset of magnetic confinement research, there was no reason *a priori* to think that plasma interaction with the tokamak wall would be particularly deleterious for fusion performance; in fact, the first tokamak plasmas were *limited* by the inner or outer wall, like the ASDEX-U plasma in Fig. 1. That is, the edge of the plasma was defined by the point(s) where the ions and electrons struck the solid wall, which acted effectively as an infinite particle sink.

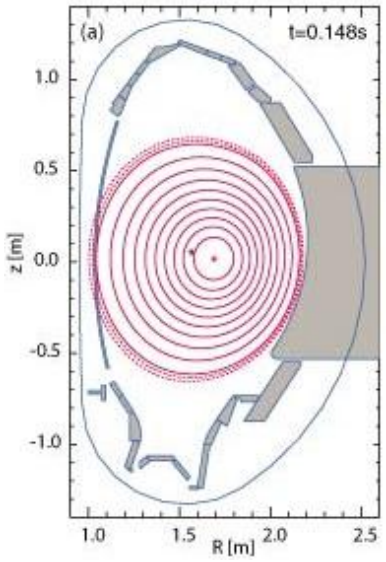

Figure 1: The cross-section of a limited plasma, represented by the pink, concentric field lines, in the ASDEX-Upgrade tokamak [1]. The edge of the plasma is defined by where it first strikes the surrounding wall.

As the triple product increased on the way to fusion, however, it quickly became apparent that the plasma edge could not be ignored. Even though the helical magnetic field inside the torus greatly improved the energy confinement time, hot plasma was inevitably transported outward radially toward the tokamak walls, admittedly for reasons that even today are not well understood. Such radial, cross-field transport is often referred to as *anomalous transport*. As fusion performance improved and plasma temperatures rose, increasingly intense heat fluxes grew at the walls, leading to excessive wall sputtering. These higher-Z, sputtered wall contaminants found their way into the plasma core, cooling it by radiating energy and polluting the D-T fuel. Furthermore, the wall was being eroded away. The wall-limited tokamak plasma had reached its plateau.

It was then decided that the magnetic "bottle" needed a fundamental design change. Using PF coils in addition to the TF coils, the magnetic geometry was altered so that the plasma was no longer incident on the wall, but instead was *diverted* into an exhaust channel outside of a certain minor radius. This was achieved by introducing a magnetic *x-point*, a singularity where the poloidal field is identically zero, and so named for its geometry (Fig. 2).

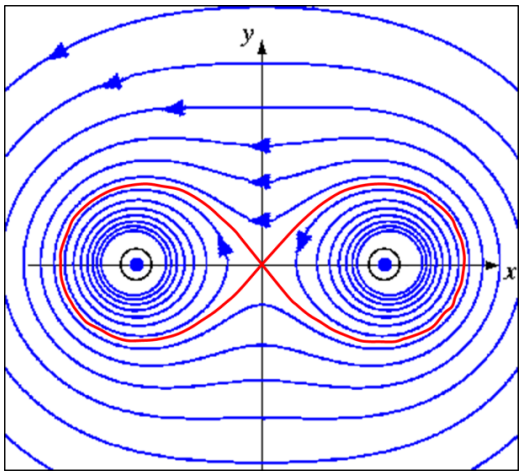

Figure 2: The magnetic field of two parallel currents will create an x-point between them, whose field line is highlighted in red. Picture courtesy of D. Kacprzak (University of Auckland) [2].

Diverted plasmas with an x-point have a *single-null* topology. Soon after, top-bottom symmetry was created to introduce a *double-null* topology as well (Fig. 3). Now, instead of the entire tokamak volume being occupied by the fusion plasma, three distinct types of regions were created around the x-point(s): the central core, where the plasma was concentrated along *closed* magnetic field lines, and fusion occurred; the scrape-off layer (SOL), where exhaust plasma was channeled out of the core and away from the walls along *open* field lines; and the private region, where virtually no plasma reached. The boundary for these three regions is the magnetic field line on which the x-point(s) lies, known as the *separatrix*.

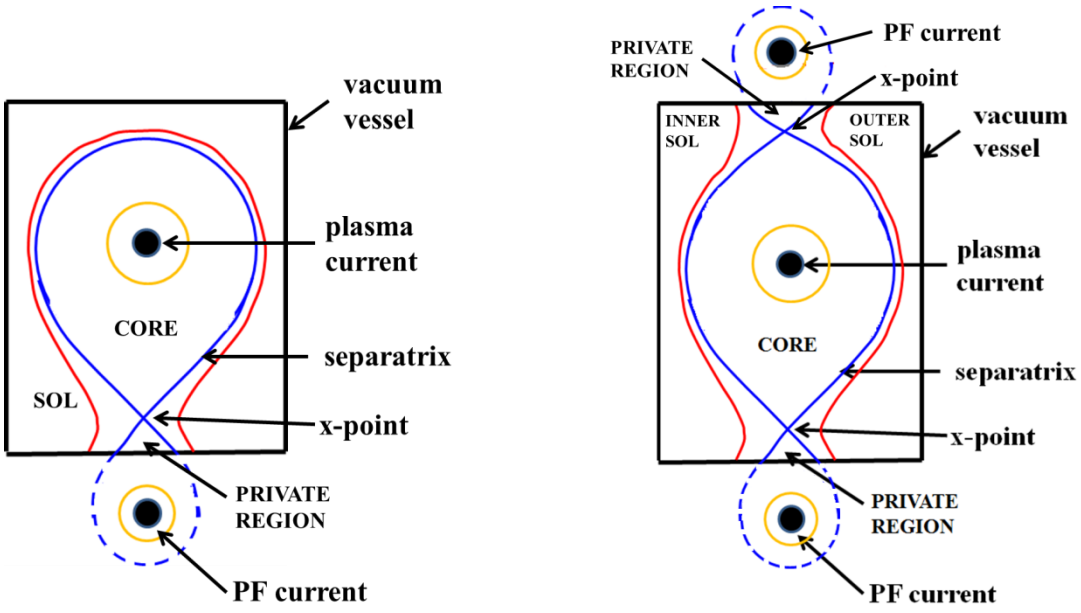

Figure 3: (Left) A simple cartoon of the cross-section of a diverted, single-null plasma. The creation of a single x-point creates three distinct regions in the magnetic geometry: a core, a scrape-off layer, and a private region. Plasma escaping the core is swept downstream in the SOL to where the field lines intersect special targets. (Right) A double-null plasma creates two physically separated SOLs and two private regions. The segments of the magnetic field lines outside of the plasma-populated regions (e.g., outside of the vacuum vessel) are shown with dashed lines.

The exhaust SOL plasma is incredibly narrow in radial extent, given that plasma transport along magnetic field lines (parallel) is several times stronger than transport across magnetic field lines (cross-field or radial). This makes the SOL incredibly effective at insulating the core plasma from the wall, even when the core is just a few centimeters from the wall. The SOL terminates at specially reinforced target plates that can withstand the incident heat fluxes; the region near these target plates is collectively known as the *divertor*. It is important to note that this innovation in plasma exhaust management was entirely magnetic in nature; it was the change in the magnetic field structure confining the plasma by way of the x-point that led to better heat load handling.

This revolutionary change did not come without compromise; the tokamak volume reserved for the SOL could no longer be used by the core, reducing the overall plasma volume available for fusion power. Nevertheless, with the plasma-wall interaction problem mitigated, the triple product could continue to be improved.

And improve it did, by a leap, in 1982 when the so-called "High-Confinement Mode," or H-mode, was discovered – completely accidentally – on the ASDEX tokamak [3]. By reaching a certain threshold in the heating power, the diverted ASDEX plasma spontaneously doubled its energy confinement time. This was due to a spontaneous, drastic reduction in edge turbulence, which greatly inhibited cross-field transport and created a *transport barrier*; plasma stayed in the core region much longer than it previously had. Nowadays, the H-mode is a commonplace phenomenon in tokamak experiments, though its mechanisms are still a hotbed of research 30 years after its discovery.

This discovery turned out to be something of a double-edged sword, however: while the H-mode meant great progress for core performance, the great reduction in cross-field transport carried over to the SOL as well. Lower cross-field transport meant that the plasma heat had less time to diffuse outward in the SOL as it approached the divertor targets, resulting in a smaller SOL width, a more concentrated flow of heat to the target plates, and a spike in their radial heat flux profiles. Furthermore, with the H-mode immediately came Edge-Localized Modes, or ELMs – abrupt, intermittent releases of energy into the SOL, resulting in time-dependent spikes of heat at the divertor targets as well.

So far, there has been no successful attempt to formulate a predictive, analytical model for the SOL width, given our lack of understanding of anomalous transport and the plasma turbulence that likely causes it. Consequently, there is strong interest in

developing empirical models for the SOL width based on existing tokamak data, and there is intense debate over such models' predictions for future tokamaks at larger scales, especially ITER. One recent heuristic model for the SOL width developed by R.J. Goldston at the Princeton Plasma Physics Laboratory, when extrapolated for the ITER tokamak, predicts its SOL width to be as small as 1-2 mm at the outer midplane [4], whereas the original design specifications were based on a width of 5 mm. Clearly, a fivefold decrease in the SOL width could have drastic consequences for heat fluxes at the ITER divertor targets.

1.2 Conventional Heat Flux Handling Techniques

Of course, divertor heat load handling has been a consideration since the advent of the divertor itself, and there is a conventional wisdom when dealing with it. For a given target material on a standard divertor, there are three conventional means of heat load handling: higher neutral density via cold gas puffing near the targets to cool the SOL plasma, high-Z impurity injection in the SOL to radiate some power away from the targets, and tilting the targets to be more oblique with the incident magnetic field, increasing the projected area of the SOL onto the targets.

Increased gas puffing, perhaps the most obvious choice to cool the SOL plasma, has diminished returns, however. Firstly, puffing in general is indiscriminate in where it affects the SOL, so while the neutral density may increase near the targets, it will also increase closer to the core, raising the edge plasma density. Because the transport barrier of the H-mode is marked by a significant gradient in plasma density and temperature near the edge, the high confinement of the H-mode becomes threatened by an increase in the

edge density and a reduction of this barrier. With excessive gas puffing, high confinement could be lost.

There is another less intuitive caveat to excessive gas puffing which has been observed experimentally. One can begin to consider this phenomenon by asking: "Why does the SOL plasma have to make contact with a target in the first place?" That is, why must the SOL be *attached* to the wall at all? In fact, it is possible to *detach* the plasma from the wall, making the issue of heat flux largely moot, by sufficiently cooling the plasma before it reaches the target. In this situation, a region of neutrals buffers the terminal end of the SOL plasma from the target, in the same way that the flame of a blowtorch gives way to un-ionized air molecules at the tip. This condition of the SOL plasma is known as *full detachment*, or just detachment. The problem, however, is that, in a standard divertor like those in Fig. 3, the neutral buffer, or detachment front, never stays near the targets; it migrates all the way back to the core plasma. This leads to core cooling and loss of energy confinement.

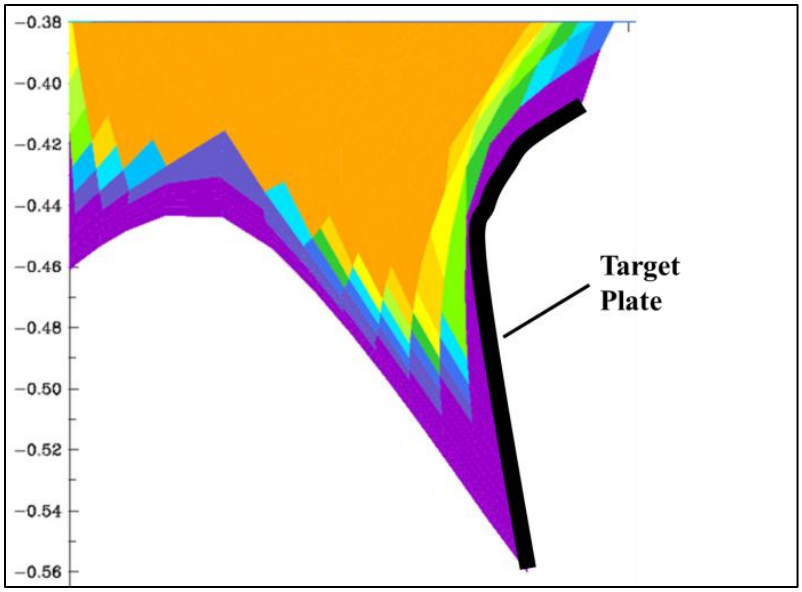

Figure 4: A color plot of plasma temperature in a simulated outboard divertor leg when it is in full detachment. Warmer colors (orange and yellow) represent higher temperatures, while dark colors (violent and blue) represent low plasma temperatures – less than 5 eV. The dominance of neutrals near the target (highlighted in black) has created a detachment front, where the temperature gradient is sharp.

Ideally, a detachment front stabilized somewhere in the SOL between the target and the core would definitively solve the divertor heat flux problem, but a stable, detached operation has never been achieved experimentally. Therefore, there is always some degree of interaction between the SOL plasma and the divertor targets in experimental tokamaks today. Detachment is currently a hot topic of research, and the possibility of its stabilization will be discussed in great detail in this dissertation.

Purposely injecting impurities, such as high-Z noble gases like neon and argon, is also a simple, non-invasive way to reduce heat loads on the target plates. Because of their large atomic numbers, these impurities strongly radiate energy isotropically when ionized and recombined, approximately according to the Z^2 relationship of the Rydberg formula. As with gas puffing though, impurity transport is indiscriminate, and just like with

impurities unintentionally sputtered from the wall, they find their way into the plasma core as well as the SOL. Excessive radiation in the core amounts to a substantial loss of energy for fusion

It's important to note further that impurity radiation by no means dissipates power in the SOL, but rather redirects it in all directions. Therefore, while impurities can be successfully used to reduce heat at the divertor targets, as much as 50% of that energy can fall back onto the targets in the form of radiation. It is important that this radiation be accounted for when calculating the total power at the targets.

Finally, the heat flux problem can be handled geometrically by making the targets themselves more oblique with respect to the incoming magnetic field of the SOL. This does nothing to cool the plasma or otherwise remove energy from the SOL; it merely spreads out the projected area of the SOL on the target over which the incoming heat is distributed, reducing its intensity.

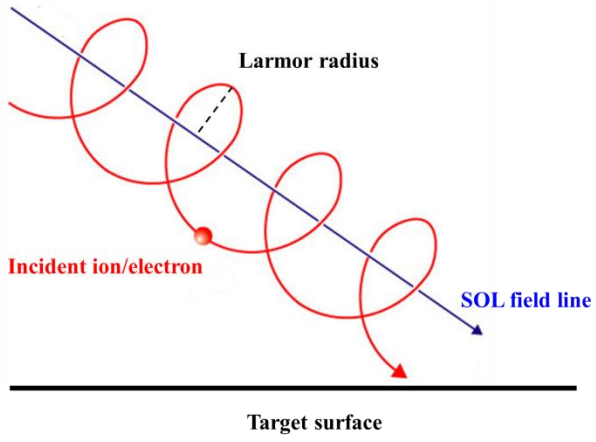

Figure 5: Gyrating ions and electrons in the SOL strike a specialized target downstream. They will collide with the solid target surface when it comes within the range of their Larmor radii.

Ideally, then, one would want to make the targets almost exactly parallel with the incident magnetic field, to allow the projected area to approach infinity. Practically though, this is not achievable, as the ions and electrons traveling toward the target gyrate with a finite radius about the magnetic field line – the Larmor radius (Fig. 5). If the target were, in fact, perfectly parallel to the field, the ions and electrons would still strike at the point where the target came within extent of their Larmor radii.

Often, not even this degree of target-field coincidence is practically feasible, given that the target is rarely a single, machined piece. Because the target extends toroidally around the entirety of the tokamak, it is often installed as several individual tiles, tiles with finite gaps between them. If the tile alignment is imperfect, as every feat of engineering is to within some tolerance, then a too-shallow incident field will instead see the side of a target tile, at an angle nearly perpendicular to the tile. This results in a concentration of heat on the side of the tile, and a "hot spot" forms (Fig. 6). To guarantee against hot spots, the incident field must therefore be kept above a certain threshold, the typically accepted value of which is 1-2°.

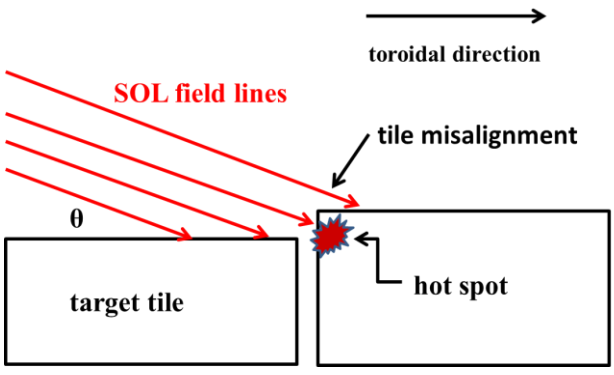

Figure 6: The reality of engineering tolerances means that target tiles are not perfectly aligned. As $\theta \rightarrow 0$, the SOL field lines will eventually "see" the side of the misaligned tile and strike it perpendicularly, leading to local, intense heat fluxes called hot spots.

So while there is a host of techniques to address heat flux problems in the divertor, each eventually develops drawbacks which become counterproductive to initiating fusion in the plasma core, or else becomes ineffectual at further reducing the exhaust heat flux. As the triple product is pushed to ever higher limits, it can only be expected that the heat flux problem in the SOL will become worse. So serious is the problem, and so hindering is it to future fusion progress, that the U.S. Burning Plasma Organization has gone so far as to label it a "bottleneck problem." To address this problem, we will have to look beyond conventional measures to a whole new class of *advanced divertors*, divertors that address the heat flux issue with fundamentally different magnetic geometries than that of the standard divertor.

Chapter 2:

Advanced Divertors: A Magnetic Solution to the Heat Flux Problem

2.1. Defining and Classifying Advanced Divertors

If conventional techniques to reduce divertor heat fluxes fall short of meeting next-generation tokamaks' needs, then the divertor itself needs to be redesigned – *magnetically*, from first principles. Just as the diverted plasma was envisioned to address the shortcomings of the limiter plasma, the geometry of the magnetic "bottle" can be redesigned to (1) allow the exhaust plasma to spend more time in the SOL, cooling it, (2) increase the area on the divertor target over which the SOL plasma is incident, reducing the heat flux, and (3) create conditions more conducive to stable detachment.

It was the x-point that defined the diverted plasma and the standard divertor (SD), and so it will be also with advanced divertors. Using one or more *additional* x-points, all advanced divertor schemes seek to manipulate the SOL by reducing B_P, the poloidal magnetic field, or B_T, the toroidal magnetic field, thereby expanding the three-dimensional SOL channel, or *flux tube*, through which exhaust plasma travels. If this so-called *flux expansion* occurs near the divertor targets, the benefit is obvious: the plasma-wetted area is increased at the target. A less obvious benefit to flux expansion in the SOL is an increase in *connection length*, the total distance an ion or electron travels to reach the target. Because B_P is made much smaller, B_T becomes even more dominant in much of the divertor region, causing ions/electrons to travel farther toroidally before terminating at the targets. The plasma therefore has more time to interact with cold neutrals and radiate energy to cool down.

Because advanced divertors employ multiple x-points, there is ambiguity when referring to "the x-point." To avoid this confusion, the x-point of the standard, diverted plasma – where the core, SOL, and private region intersect – will heretofore be referred to as the "main x-point," while additional x-points elsewhere will be referred to generically, or else be given identifying labels. Single-null plasmas have one main x-point, while double-null plasmas discussed in this work have two main x-points along the same separatrix, at the top and bottom of the core.

While all advanced divertors share the common characteristic of multiple x-points, they can be categorized into two general classes by their effect on the SOL. The first, the X-Divertor (XD), was published in 2004 by Kotschenreuther *et al.* at the University of Texas at Austin [5]. While a more rigorous definition is discussed in Section 5.2, generally speaking, an X-Divertor utilizes a second x-point in the SOL downstream of the main x-point. In so doing, B_P is reduced locally (since $B_P = 0$ at any x-point), and flux expansion is created near the target. Connection length along the entire divertor leg is also increased.

An extension of the XD, the Super X-Divertor (SXD) [6] takes the idea further by using *two* or more x-points to bend and extend the divertor leg to a greater major radius before it terminates at a target. Since the toroidal field B_T in a tokamak decreases proportionally to $1/R$, the SXD benefits from reductions in both the poloidal and toroidal field strength, resulting in very large flux expansion and increased connection length at the target. Both an XD and SXD are shown alongside a standard divertor in Fig. 7.

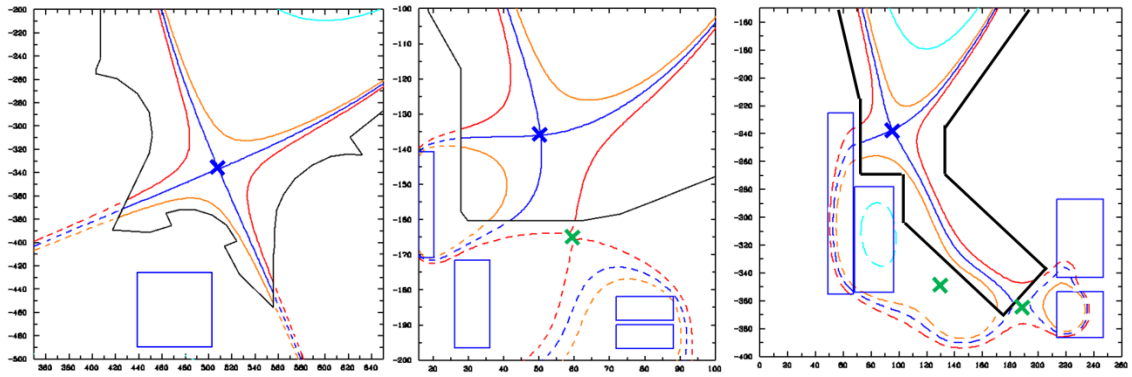

Figure 7: (left) A standard divertor has a single, main x-point (shown in blue). (center) An X-Divertor introduces a secondary x-point (shown in green) in the downstream SOL to increase poloidal flux expansion at the targets. (right) A Super X-Divertor draws the divertor leg out to a larger major radius to increase toroidal flux expansion, as well as poloidal flux expansion.

It is also hypothesized that the XD and SXD may create beneficial conditions for stable detachment, the third goal of advanced divertors highlighted at the beginning of this section. This possibility is discussed in great detail in Section 6.4.

The other category of advanced divertor is the Snowflake Divertor (SF), first published by Ryutov *et al.* at Lawrence Livermore National Laboratory (LLNL) in 2007 [7]. Unlike the XD or SXD, the Snowflake utilizes a second x-point in or very near the private region, often almost so as to be coincident with the main x-point. The resulting six-lobed magnetic geometry gives the SF its apt name (Fig. 8). By doing this, a large region is created where not only B_P is very small, but its gradient as well, leading to very large flux expansion in the immediate vicinity of the main x-point.

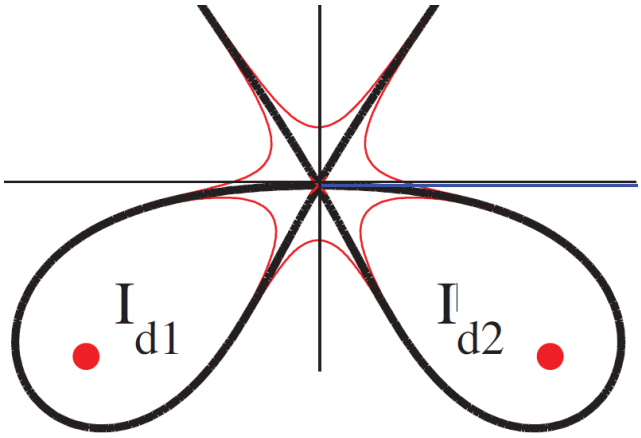

Figure 8: The Snowflake Divertor has its two x-points exactly coincident, canceling out not only B_P but its gradient as well, resulting in very large poloidal flux expansion at the x-points and a characteristic six-lobed geometry. Picture courtesy of D.D. Ryutov (LLNL) [7].

Two sub-categories of the SF exist: the Snowflake Plus (SF+) and Snowflake Minus (SF-) configurations. Because a "pure" Snowflake – with two coincident x-points – is topologically unstable, the x-points are always kept some finite difference apart. In the case of the SF+, the second x-point resides somewhere in the private region, while with the SF-, the second x-point almost lies on the separatrix, neither upstream nor downstream of the main x-point.

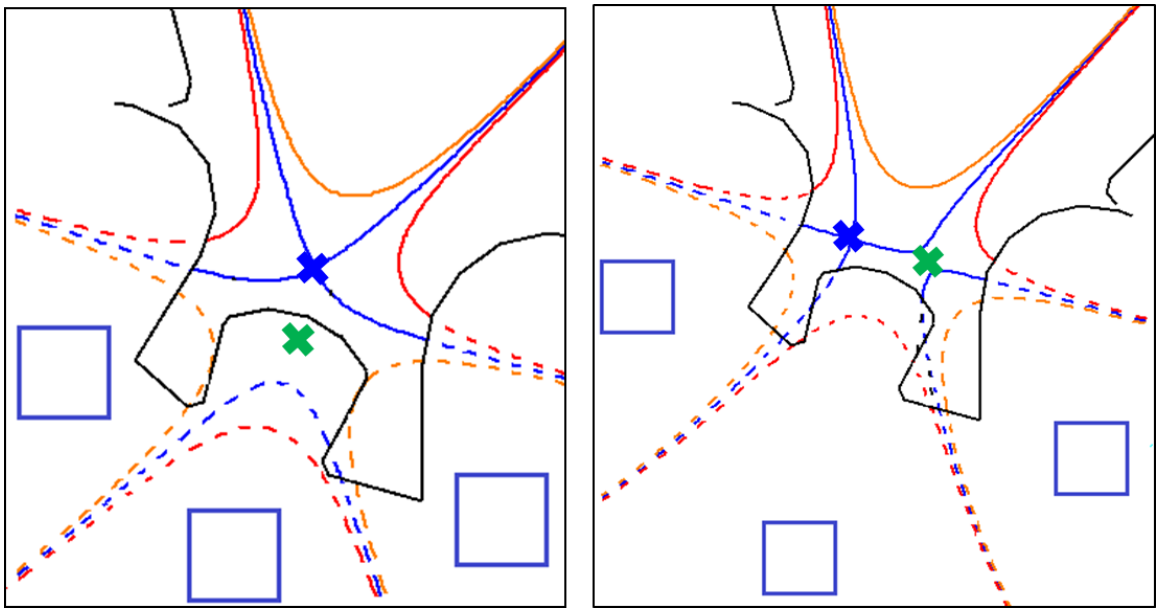

Figure 9: A "pure" Snowflake is topologically unstable, so the two x-points are always kept some finite distance apart, such as with the Snowflake Plus (left) and Snowflake Minus (right).

The qualitative distinction between advanced divertors becomes murkier when divertor legs are very short and all x-points are in close proximity. A new definition, needed to unambiguously characterize divertor behavior in a quantifiable way, is given in Section 5.2.

2.2. Applications of Advanced Divertors

The benefit of advanced divertors to tokamak research is clear. The fusion triple product cannot continue to be pushed higher in the plasma core if an unacceptable amount of heat is exhausted into the SOL without mitigation in the divertor, but heat mitigation in the divertor cannot result in degradation of fusion performance in the core. Advanced divertors offer a means to achieve both good core performance and SOL heat mitigation.

While the divertor heat flux problem is an issue for all tokamaks, it is of particular concern to spherical tokamaks (ST), tokamaks whose aspect ratio is near 1. Tokamaks so far have been the leaders of magnetic confinement devices in terms of increasing the triple product, but it is debatable whether expanding them to larger and larger sizes to push the envelope represents progress toward an economical power plant or not. Spherical tokamaks improve confinement efficiency by reducing the volume over which the magnetic "bottle" must extend (Fig. 10). Confinement accounts for much of the cost of a tokamak, due to both the size of the components and the required TF and PF coil currents.

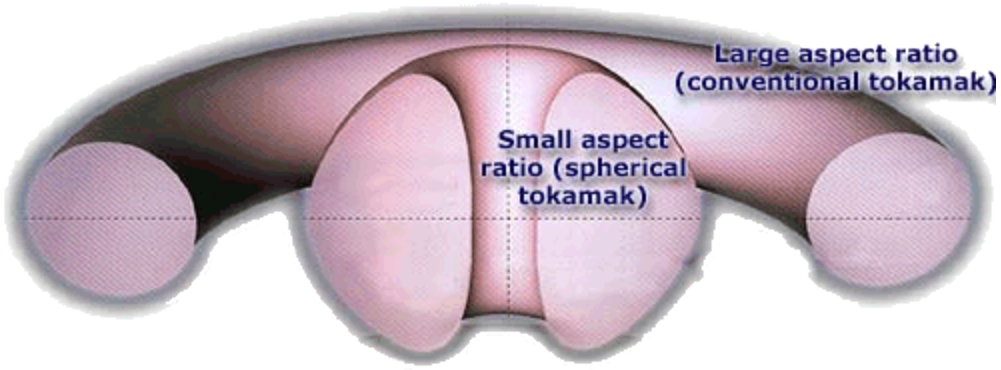

Figure 10: A comparison of the relative dimensions of a conventional tokamak and a spherical tokamak. A conventional aspect ratio, $A = R_o/a$, is much larger, resulting in the familiar doughnut shape. Spherical tokamaks are tighter, requiring less magnetic field strength to confine the plasma. Picture courtesy of the Culham Centre for Fusion Energy [8].

However, more efficient confinement in STs comes at a cost; the target area over which the exhaust heat may be spread is even smaller, further compounding the problem of intense heat fluxes in the SOL. Advanced divertors become even more imperative for STs.

While tokamaks have made incredible progress, the deadline to curb energy practices deemed to cause irrevocable changes to the global ecology seems still to outpace progress toward an economical reactor, according to many climate change experts. If "pure" fusion remains out of reach, then a fusion-fission hybrid reactor may offer an intermediate solution to reduce fossil fuel emissions while addressing some of fission's biggest problems, and advanced divertors could play a critical role.

In a hybrid scheme, the goal of fusion is not to produce net energy, but high-energy neutrons – neutrons to break down harmful waste from the fission process. The D-T reaction in particular deposits most of its energy in its product neutron, and it is the most easily attainable reaction in the practical temperature range, making a low-gain fusion reactor an attractive candidate as a cost-effective neutron source. Fission reactors, then, would remain the workhorses to produce energy, while the fusion reactor breaks down fission's waste more thoroughly and more *safely* than other fission-based methods, such as fast reactors. The uniquely high-energy neutrons of fusion relax the requirement that the fission waste be highly concentrated in order to be transmuted, making it much safer to handle and destroy.

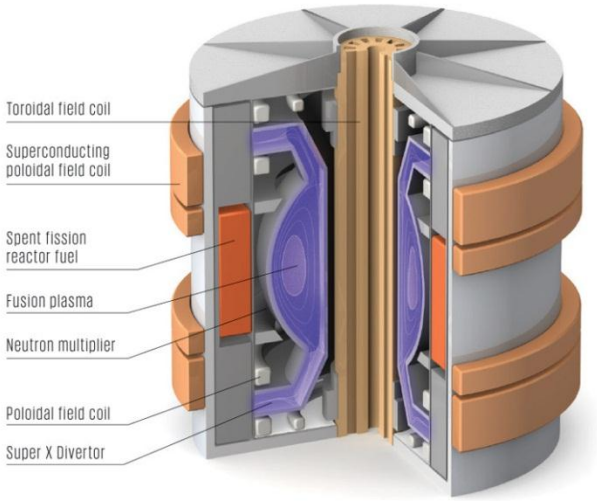

Figure 11: The CFNS "battery" is designed to be light, self-contained, and entirely removable from the fission waste system. High-energy fusion neutrons destroy fission waste, but the intense exhaust heat fluxes from the power-dense plasma inside will likely require a Super X-Divertor to be mitigated.

The coupling of two complex, nuclear technologies introduces its own host of risks, though. Therefore, it would be ideal if the fusion process were as separate from the fission process as possible, and vice versa. To this end, a UT-Austin IFS team, consisting of Swadesh Mahajan, Mike Kotschenreuther, and Prashant Valanju, has developed a hybrid concept in which a fission waste blanket is entirely separable from a compact fusion "battery (Fig. 11)." That is, the fusion neutron source is small and light enough to be able to be inserted and removed as a single unit via robotic handling. In this way, the machinery of the fusion source is entirely de-coupled from the machinery around the fission waste blanket, the fusion source can be easily removed for maintenance, and it is economically feasible to house two fusion "batteries" simultaneously – one always in operation, and one always under maintenance.

Even for a lower-gain fusion neutron source, however, the plasma triple product must be sufficiently high to yield a steady fluence of neutrons. Moreover, because compactness and lightness are such desirable goals, the fusion source must be low-aspect ratio as well, meaning that it could suffer many of the divertor heat flux problems of STs. Advanced divertors, then, are just as applicable to hybrid technologies as they are to traditional fusion research, and progress in divertor research is mutually beneficial.

Advanced divertors represent a new layer of complexity in tokamak science and technology, just as the diverted plasma was more complex than the limiter plasma. However, added complexity may be inevitable if extrapolations of the SOL width scaling laws prove true, as the consequences for unmitigated heat fluxes at the target plates are severe. If advanced divertors do in fact become necessary to address the SOL heat problems of the next generation of tokamaks, it is important from the onset of their implementation that we thoroughly understand their unique qualities, and the transport and cooling mechanisms at work in the SOL.

To do so, intensive experimentation will have to be performed on a diverse cross-section of tokamaks. However, even before experimentation can take place on such large-scale devices as tokamaks, their investigation needs to be motivated by compelling numerical modeling results. With this in mind, we seek to build accurate, robust, time-dependent models of advanced divertors on many tokamaks, both current and future, incorporating both the magnetics that define them and the transport physics that play out in their scrape-off layers. These models are very complex, integrating the calculations of several independently operating scientific codes. As a result, high-performance

supercomputers are required to yield any results in a timely fashion. Armed with supporting data from these numerical models, advanced divertors are poised to clear away a serious bottleneck in fusion research, using technology that exists today.

II. TOKAMAK MAGNETICS AND SCRAPE-OFF LAYER PLASMA PHYSICS

Chapters 4 and 5 of Volume II establish the foundations of magnetic field shaping specifically as it relates to tokamak confinement and divertor design. Basic quantities of magnetic field structures are defined. The criteria for force balance between the tokamak plasma and the magnetic field are established in the Grad-Shafranov equation. Finally, the Divertor Index is conceived to classify advanced divertors by their practical effects on the SOL flux tube.

Chapter 6 lays out the essential plasma physics in the SOL pertinent to understanding the divertor heat flux problem. The interplay between the plasma physics, neutral gas physics, and atomic physics in the divertor is described. A heuristic model for the power SOL width is given. Finally, a detailed description of detachment is given, including how the Divertor Index may play a critical role in determining the feasibility of detachment stabilization.

Chapter 3:

The Magnetic Geometry of the Diverted Plasma Equilibrium

3.1. PLASMA SHAPING

It is intuitive for one's first picture of the 3D tokamak magnetic field structure to be helical. Inside the tokamak, the solenoid-like TF current sources create a toroidal field, B_T, and the toroidal current running through the plasma creates a circular, poloidal field. The summation of these components forms a helix that closes (or nearly closes) back on itself after one or more revolutions around the torus, confining the plasma ions and electrons that gyrate about it according to the Lorentz force. The plasma current helps to stabilize the plasma against expanding outward, which happens naturally due to the inhomogeneity of B_T in the R-direction, which the ions and electrons see on opposing sides of their orbits as they gyrate about their field lines.

To examine the magnetic field structure, it is useful to adopt cylindrical coordinates: rectilinear coordinates *(R,z)* in the poloidal plane, and an assumption of axisymmetry in the toroidal direction for simplicity. The majority of our attention will therefore be focused on the 2D magnetic field projection in the poloidal plane, though there are important 3D effects to keep in mind, even in the simplest considerations.

The tokamak plasma cross-section may always be viewed as a perturbation from a perfect circle in the poloidal plane. However, experimental observations have overwhelmingly shown that plasma performance improves in several ways when the cross-section shape is purposely manipulated away from a circle. PF coils put specifically to this use are often referred to as "shaping coils." The two most common attributes to describe plasma shape are elongation (κ) and triangularity (δ). Elongation simply

quantifies the ellipticity of the plasma, taking the ratio of the plasma height (as measured from the midplane) over the minor radius a.

$$\kappa = \frac{y}{a} \tag{1}$$

Clearly, $\kappa = 1$ for a perfectly circular plasma, when $y = a$, and $\kappa > 1$ for a vertically elliptical plasma, with no theoretical upper bound. Elongated plasmas have been shown to have improved energy confinement time over circular plasmas, but elongation also increases the growth rate of the vertical instability – the tendency of the entire plasma to shift up or down. There is therefore a range of acceptable elongations, particular to every tokamak, where the desire for better confinement and the need to keep the plasma vertical instability growth rate within the time scale of active control systems have been balanced. Typically allowed values for κ have ranged anywhere between 1.5 and 3.3.

Triangularity, meanwhile, is a measurement of how the plasma shape detracts from an ellipse in favor of a more triangular shape, by allowing the topmost and bottommost endpoints of the plasma to migrate to the inboard side from their natural location at the plasma major radius R_o. Triangularity is defined as the ratio of this migration distance over the minor radius a.

$$\delta = \frac{R_o - R_{xpt}}{a} \tag{2}$$

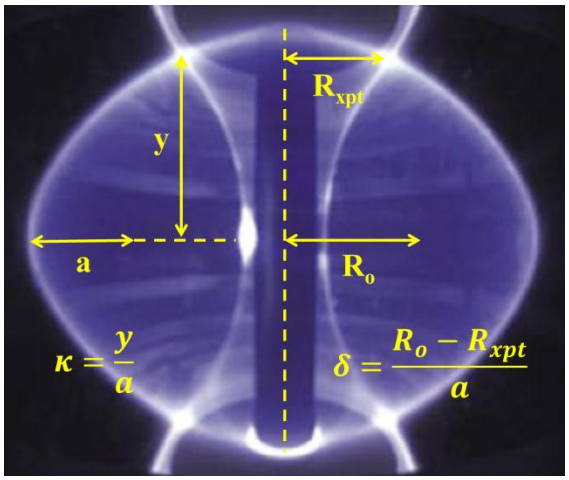

Figure 12: Plasma elongation and triangularity illustrated using the dimensions of the MAST double-null plasma. The bright, white lines outline the plasma's separatrix. MAST plasma photograph courtesy of HPCx (University of Edinburgh) [9].

A regular, elliptical plasma will therefore have a triangularity of 0 when its vertical endpoints reside at the plasma major radius, and a perfectly triangular plasma will have a triangularity of 1 when its vertical endpoints reside at the same major radius as the inner plasma boundary, $R_o - a$. Note that one can define separate triangularities for the top and bottom endpoints, particularly in a single-null plasma. Theoretically, δ could exceed 1, creating an inflection on the inboard side of the plasma, though this has never been pushed experimentally. Because higher triangularity pushes more of the plasma toward the inboard side, where B_T is higher (recall that B_T is proportional to $1/R$, so the inboard side is often called the "high-field side"), energy confinement and plasma stability tend to improve, with virtually no adverse effects. Therefore, triangularity is typically only restricted by the shaping capabilities of the PF coils of the particular tokamak. Typical values for the triangularity range from 0.4 – 0.9.

Both elongation and triangularity are illustrated in Fig. 12.

3.2. ANATOMY OF THE POLOIDALLY DIVERTED PLASMA

The introduction of the x-point added significant complexity to the tokamak geometry; no longer did it consist of concentric poloidal field lines all the way out to the first wall, but now three topologically distinct regions – the core, the private region, and the SOL – whose boundaries are marked by the x-point and the field line on which it lies, the separatrix.

The core region represents the conventional magnetic "bottle" of the tokamak, since field lines in this region are closed, confining trapped ions and electrons in an endless trajectory around the tokamak. "Closed" is a somewhat inaccurate term, however, for the vast majority of field lines do not perfectly close back on themselves after one or any number of toroidal revolutions, ending at the exact point where they began. After all, for a helical field line to close perfectly on itself in a tokamak, the ratio of its toroidal cycles to its poloidal cycles would have to be that of two integers (e.g., 3 poloidal cycles for every 1 toroidal cycle). This is the definition of a rational number, and within any given number range, there are far more irrational numbers than rational numbers. Because B_P and B_T must be continuous in space, their ratio must also be continuous, assuring us that there will be many more irrational ratios than rational ratios.

For irrational field lines, it becomes more descriptive to talk about *surfaces* rather than lines, as a single field line will eventually pervade the entire toroidal surface upon which its helical path lies. This descriptor can even be applied to rational field lines; on such surfaces, we simply have infinitely many starting points on which to draw self-closing field lines, as opposed to one field line of infinite length that passes through all points. We can therefore discuss field lines and surfaces interchangeably, depending on the behavior on which we are focusing. And regardless of the manner in which they do it,

both rational and irrational field lines in the core region are "closed" in that they are nested inside the separatrix.

Each surface can be uniquely identified by the total amount of magnetic flux, $\vec{B} \cdot \vec{A}$, encompassed in the surface area, since this quantity increases monotonically as one moves toward the edge of the core (Fig. 13). Hence, these magnetic surfaces are most often referred to as *flux surfaces*. This definition applies equally well for either toroidal or poloidal flux. Working backward, we can then define the surface that contains zero flux as the *magnetic axis*. At the magnetic axis, the trajectory of the field line is purely toroidal, the enclosed area is zero, and $B_P = 0$. The magnetic axis may be thought of as the magnetic center of the core region, though it is rarely at the geometric center of the core plasma.

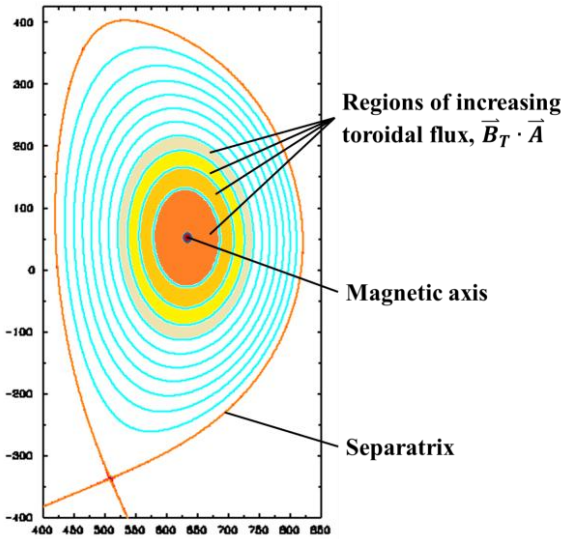

Figure 13: In the core region, flux surfaces are closed, and they can be defined by the amount of magnetic flux they encompass. The separatrix defines the boundary between the closes flux surfaces of the core and the open flux surfaces of the SOL.

The boundary of the core region in a diverted plasma is sharply defined at the separatrix, outside of which flux surfaces transition from being closed to being open – this is the SOL. All SOL field lines, no matter their length, begin at the material surface of one divertor target and end at the material surface of another target. This quality, of course, motivates our interest in heat fluxes incident on the targets. The connection length of an SOL field line between the two targets, or between one target and a point of interest, will clearly depend on the profiles of B_P and B_T, and thus the pitch, along that field line. For a given B_T, where B_P is relatively weak, the pitch of the field line is low, and the field line will travel much farther in the toroidal direction before striking a target, adding a large distance to the connection length. Where B_P is relatively strong, the pitch is high, and a more significant component of the field line trajectory is directed straight toward the targets; these areas add a much shorter distance to the connection length. This change in field line pitch according to changes in B_P and B_T is illustrated in Fig. 14. While the SOL cannot confine any plasma entering it indefinitely, it is in the interests of the divertor targets to make the connection length as long as possible, giving the SOL plasma more time to cool as it makes its way toward them.

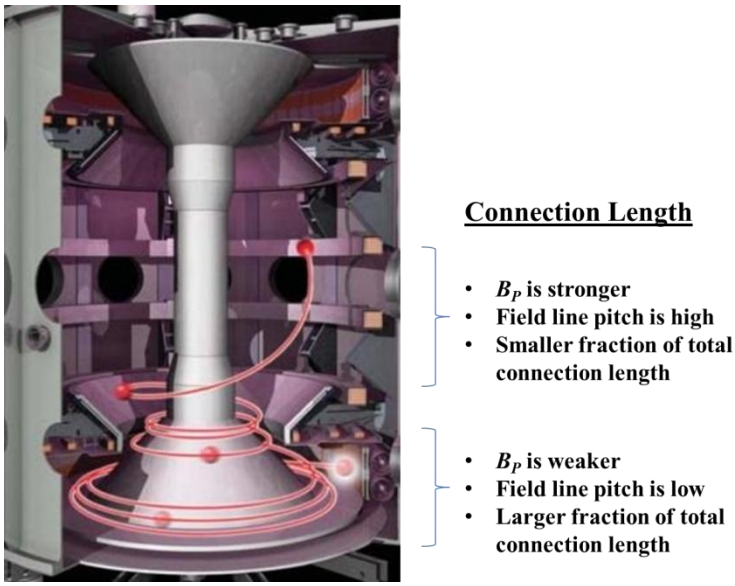

Figure 14: An illustration of an average particle trajectory along a field line in the MAST Super X-Divertor. By reducing B_P near the target below, the field line pitch is reduced, and the particle is able to make several more toroidal revolutions before striking the target. MAST picture courtesy of the University of York [10].

Because SOL field lines are open, we may loosely define direction along them as either moving toward (downstream) or away from (upstream) a target plate, with the understanding that this terminology flips when one is halfway between targets in the SOL. The divertor regions of the SOL are those segments downstream of the main x-point, where the core region ceases to be a neighboring region, and the private region begins.

To build the foundation for understanding the magnetics of advanced divertors, let us consider a 3D, tube-like layer in the SOL, sandwiched by two flux surfaces a finite radial distance apart, and terminating on its ends at two targets. Because $\nabla \cdot \vec{B} = 0$ according to Maxwell's Equations, the total magnetic flux entering this tube must be conserved. The flux tube will therefore alter its local surface area as it passes through gradients in B_P and B_T, expanding through low-field regions and contracting through

high-field regions, preserving its total magnetic flux. A reduction in the SOL magnetic field is therefore beneficial not only to the connection length, but for expanding the flux tube at the targets and increasing the area over which the exhaust plasma is incident, and this is precisely the goal of advanced divertor geometries.

The third and final region of the diverted plasma consists of the fourth lobe created by the x-point, the private region. Because this region is opposite the core at the x-point, very little plasma is transported into this region, the majority of which comes back over from the SOL in the divertor region. Consequently, the private region is often dominated by cold neutrals, and is highly important in the study of neutral-plasma interaction in the divertor. Many tokamak structures will conform tightly to the shape of the private region in order to maximize neutral density in the divertor, to help cool the SOL plasma.

3.3. Magnetic Equilibria and the Grad-Shafranov Equation

To continue further with our analysis of tokamak and divertor magnetics, we must now establish its mathematical foundations. That is, we seek a balance between the outward force of the plasma pressure and the inward force imposed by the magnetic field with toroidal symmetry – a *magnetic equilibrium*:

$$\nabla P = \vec{J} \times \vec{B} \tag{3}$$

Where P is the plasma pressure, $\vec{J}$ is the plasma current, and $\vec{B}$, of course, is the magnetic field. Eq. 3 is a vector equation, representing a system of equations, one for each spatial coordinate. Immediately, we can note that the pressure gradient is

everywhere perpendicular to $\vec{B}$. Toroidal symmetry of the pressure profile automatically guarantees this to be true of $\vec{B}_T$, so this must also be true of $\vec{B}_P$ independently, meaning that the pressure must be constant along any field line in the poloidal plane. Similarly, $\boldsymbol{\nabla} P$ is everywhere perpendicular to $\vec{J}$, but since $\boldsymbol{\nabla} P$ is also perpendicular to $\vec{B}_P$, $\vec{J}_P$ must point along field lines. Hence, there are no cross-field currents in a steady-state plasma equilibrium. These vector relationships are shown in Fig. 15.

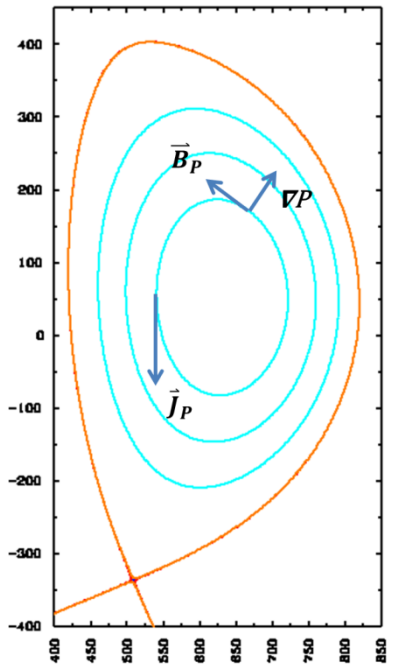

Figure 15: $\vec{B}_P$ and $\vec{J}_P$ are everywhere parallel to field lines, while $\boldsymbol{\nabla} P$ is perpendicular to field lines.

It is useful to define a scalar function $\psi \equiv RA_T$, where A_T is the toroidal component of the magnetic vector potential. It follows that $\vec{B}_P$ is everywhere perpendicular to $\boldsymbol{\nabla}\psi$ (see Appendix B); ψ is therefore an appropriate stream function for

the poloidal field. This is a very valuable simplification of the representation of the poloidal field. The total field is now written as:

$$\vec{B} = \frac{1}{R}\nabla\psi \times \hat{\varphi} + B_T\hat{\varphi} \tag{4}$$

As previously noted, ∇P is perpendicular to $\vec{B}_P$, and P is constant along any given field line, so it follows that P is an explicit function of ψ, $P(\psi)$. Furthermore, from our previous observation that ∇P must be perpendicular to $\vec{J}_P$, and that P is an explicit function of ψ, it also follows that the scalar function RB_T must also be an explicit function of ψ, $F(\psi)$ (see Appendix B). Eq. 3 can then be rewritten as:

$$\Delta^*\psi = -\mu_o R^2 \frac{dP}{d\psi} - F\frac{dF}{d\psi} \tag{5}$$

Where $\Delta^*\psi \equiv R\nabla \cdot \frac{1}{R}\nabla\psi$. Eq. 5 is the Grad-Shafranov (G-S) equation. In place of a vector-valued differential equation, there is now an equation of a single scalar function, ψ, with $P(\psi)$ and $F(\psi)$ as inputs. We will seek to solve this equation when searching for stable magnetic equilibria of advanced divertors. That is, any distribution of PF and TF currents we choose to design divertors are constrained by the requirement that their Lorentz forces balance against the thermodynamic pressure of the plasma, which is embodied in this equation.

Up to this point, B_T has been left as a given function. In tokamaks, it can be solved for explicitly. Because the toroidal field is approximately axisymmetric (bearing in mind that the magnitude will vary slightly in the gaps between TF coils), we may apply Ampere's Law to find the strength of the field along a concentric ring.

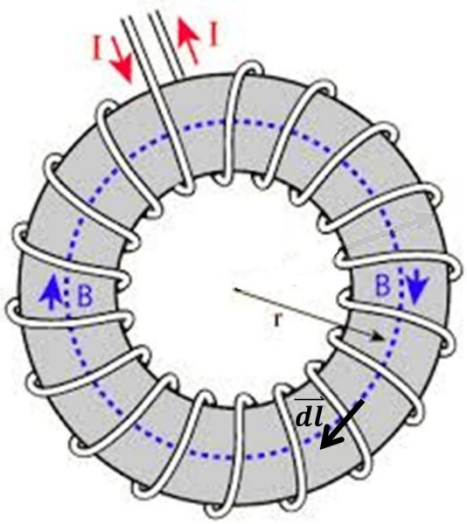

Figure 16: Ampere's Law can be readily applied in a tokamak to solve for B_T. Picture courtesy of Georgia State University [11].

The enclosed current in Fig. 16 is merely the current running through each TF coil times an arbitrary number of TF coils, so B_T is readily solved for everywhere inside the TF coils:

$$\oint \vec{B} \cdot \overrightarrow{dl} = \oint B_T dl = \int_0^{2\pi} B_T R d\varphi \approx 2\pi R B_T = \mu_o N I_{TF}$$

$$B_T \approx \frac{\mu_o N I_{TF}}{2\pi R} \tag{6}$$

Interestingly enough, there is a very simple relationship between our stream function ψ and the poloidal magnetic flux encompassed by an area inside the flux surface at ψ, which will be called ψ_p.

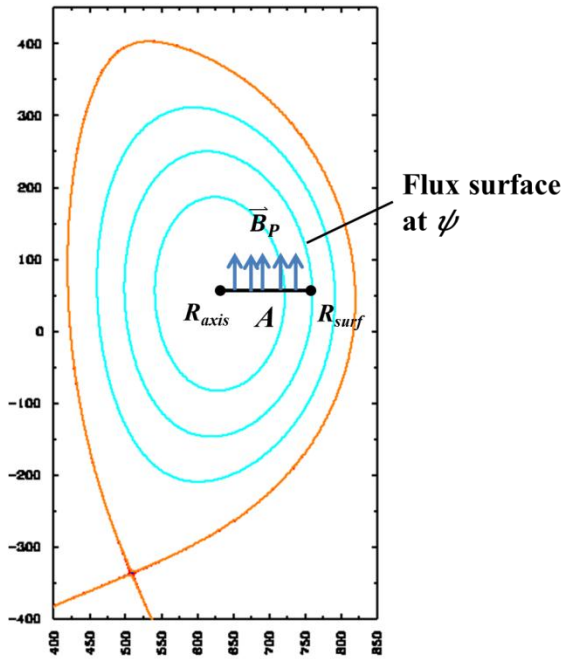

Figure 17: The poloidal magnetic flux through the annular area A (when including the toroidal dimension) from the magnetic axis to any flux surface of value ψ is equal to $2\pi\psi$.

We have already established that any flux surface is associated with a value of the stream function ψ. If we evaluate the poloidal flux through the annular area at the midplane bounded by this flux surface and the magnetic axis (Fig. 17), we get:

$$\psi_p = \oint \vec{B}_P \cdot \overrightarrow{dA} = \int_0^{2\pi} d\varphi \int_{R_{axis}}^{R_{surf}} RB_z dR$$

$$= 2\pi \int_{R_{axis}}^{R_{surf}} R\left(\frac{1}{R}\frac{\partial\psi'}{\partial R}\right) dR = 2\pi \int_0^{\psi} d\psi'$$

$$= 2\pi\psi \qquad (7)$$

The value of our stream function ψ at a given flux surface only differs by a factor of 2π from the total poloidal flux through the midplane area bounded by that flux surface, ψ_p. And since, as discussed in Sect. 3.2, ψ_p increases monotonically and can therefore be used to uniquely identify flux surfaces, so too can ψ. These kinds of coordinates are called *flux coordinates*, and functions that can be written explicitly in terms of ψ, such as the plasma pressure and the parallel current, are called *flux functions*.

The Grad-Shafranov equation is the mathematical foundation upon which we will base our research into the magnetics of advanced divertors: it is the equation that the magnetics code will need to solve numerically, and it is its stream functions in the SOL we will attempt to manipulate to increase the plasma-wetted area.

Chapter 4:

Magnetic Geometries of Advanced Divertors

4.1. Projection of the SOL Flux Tube

Having now established the foundations of magnetics for axisymmetric tokamaks, we turn our attention entirely to the SOL, the region relevant to divertors. Integrating $\nabla \cdot \vec{B}$ over the volume of a flux tube, it is easy to see that expansion of the tube is inversely proportional to the strength of the magnetic field passing through the cross-sectional area of the tube, to preserve magnetic flux. This must hold true at all points along the SOL, since the choice of flux tube is arbitrary. If we take one end of the flux tube to be upstream at the inner/outer midplane, where the plasma first enters the SOL, and the other end to be at the strike point(s) downstream (Fig. 18), then we see:

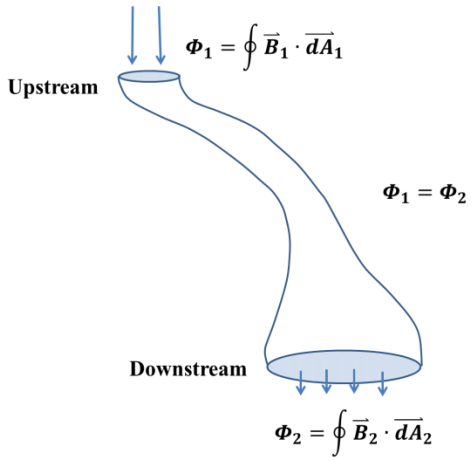

Figure 18: A model of the SOL flux tube, which is cylindrical in its topology. Because magnetic flux is conserved through any enclosed volume, and there is no flux through the lateral sides, a reduction in the field strength downstream expands the area of the flux tube.

$$\oint \nabla \cdot \vec{B} dV = \oint \vec{B} \cdot \overrightarrow{dA} = B_{up}A_{up} - B_{down}A_{down} = 0$$

$$A_{down} = \frac{B_{up}A_{up}}{B_{down}} = \frac{B_{up}A_{up}}{\left(B_{P,down}^2 + B_{T,down}^2\right)^{1/2}} \tag{8}$$

Being unable to affect the upstream end of the SOL flux tube without negatively affecting confinement in the core, it becomes imperative that the total magnetic field be reduced as much as possible downstream, at the strike points, to maximize flux expansion. This can be done either by reducing B_P, as with the X-Divertor and Snowflake; B_T, as with the Super X-Divertor; or both. To be clear, A_{down} is only the area of the flux tube incident on the target when the target is perpendicular to the flux tube (which is never the case); the true projected area of the flux tube incident on the target differs by a factor sinθ as the target is tilted:

$$A_{projected} = \frac{1}{sin\theta} \frac{B_{up}A_{up}}{\left(B_{P,down}^2 + B_{T,down}^2\right)^{1/2}} \tag{9}$$

Up to this point, our discussion has been limited to the topic of magnetics, but what about the plasma behavior in the SOL? What guarantees do we have that an expanded magnetic flux tube will be followed by a broadening of the exhaust plasma inside it? By the ideal MHD Ohm's Law (i.e., with perfect plasma conductivity):

$$\vec{E} + \vec{v} \times \vec{B} = 0 \tag{10}$$

We can show that the magnetic flux passing through the ends of a flux tube in the SOL is unchanging in time. In essence, the flux is frozen into the plasma, and the

magnetic fields lines must shift with the plasma, and vice versa. If we consider the total time derivative of the total magnetic flux through the area A of a flux tube:

$$\begin{aligned}
\frac{d\psi_{total}}{dt} &= \frac{d}{dt}\oint \vec{B}\cdot\overrightarrow{dA} \\
&= \oint\left(\frac{d\vec{B}}{dt}\cdot\overrightarrow{dA} + \vec{B}\cdot\frac{d\vec{A}}{dt}\right) \\
&= \oint\left[\left(-\nabla\times\vec{E}\right)\cdot\overrightarrow{dA} + \vec{B}\cdot\left(\vec{v}\times\overrightarrow{dl}\right)\right] \\
&= \oint\left[\left(-\nabla\times\vec{E}\right)\cdot\overrightarrow{dA} + \left(\vec{B}\times\vec{v}\right)\cdot\overrightarrow{dl}\right] \\
&= \oint\left[\left(-\nabla\times\vec{E}\right)\cdot\overrightarrow{dA} + \nabla\times\left(\vec{B}\times\vec{v}\right)\cdot\overrightarrow{dA}\right] \\
&= -\oint\left[\nabla\times\left(\vec{E}+\vec{v}\times\vec{B}\right)\right]\cdot\overrightarrow{dA} \\
&= 0
\end{aligned}$$

This is Alfven's theorem, and it shows that if we successfully manage to widen the SOL flux tube by reducing the magnetic field, the plasma heat and particle fluxes traveling downstream will actually broaden as well. If they didn't, broadening of the flux tube alone would not decrease the heat flux.

While flux expansion has its obvious benefits, it has recently been suggested that the spatial evolution of the SOL flux tube may also play an important role in handling the heat flux problem, by opening regimes of stable detachment [12]. That is, not only should we consider the size of the area of the SOL flux tube at the strike point, but we should also pay attention to its gradient as it approaches the strike point. Thus, we want to draw a distinction between the area of the flux tube at a given point, the *flux expansion*, and its gradient, which we will call *flaring* (Fig. 19).

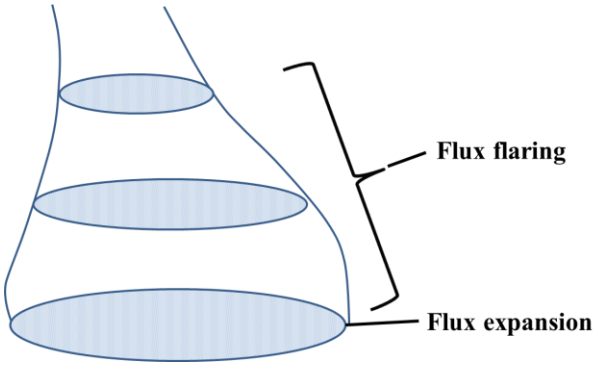

Figure 19: The difference between flux expansion and flux flaring illustrated. Flux expansion represents the area of the flux tube relative to the upstream SOL at any given point, while flux flaring describes the way flux expansion varies in space.

It should be intuitively clear that flux tube flaring itself has no bearing on the projected area at the target; after all, regardless of the changes in the flux tube area throughout the SOL, the only area that matters is the one we see at the strike point. Flux expansion and flaring are independent quantities, just as the value of a function and its derivative are independent. All advanced divertors – X-Divertor, Snowflake, and Super X-Divertor – achieve great flux expansion, but it is the nature of the flaring of the SOL flux tube by which we propose to distinguish them.

4.2. Formal Classification of the Advanced Divertors

In Sect. 2.1, an informal definition of an advanced divertor was given: a magnetic geometry which utilizes one or more secondary x-points to increase connection length and expand the SOL flux tube at the target plate(s). The three types of advanced divertors were then broadly categorized by the location of their secondary x-points in the SOL, and where in the SOL flux expansion was maximal. There are two problems with rigorously defining magnetic geometries in this way. First, these definitions rely on relative distance

between x-points, but x-point distances and divertor leg lengths can vary greatly from tokamak to tokamak (Fig. 20). Second, these definitions tend to rely on the characteristics of the magnetic field (such as the locations of x-points) *outside* of the SOL, characteristics which are not only irrelevant to the physics of the plasma, but which are also not unique (Fig. 21).

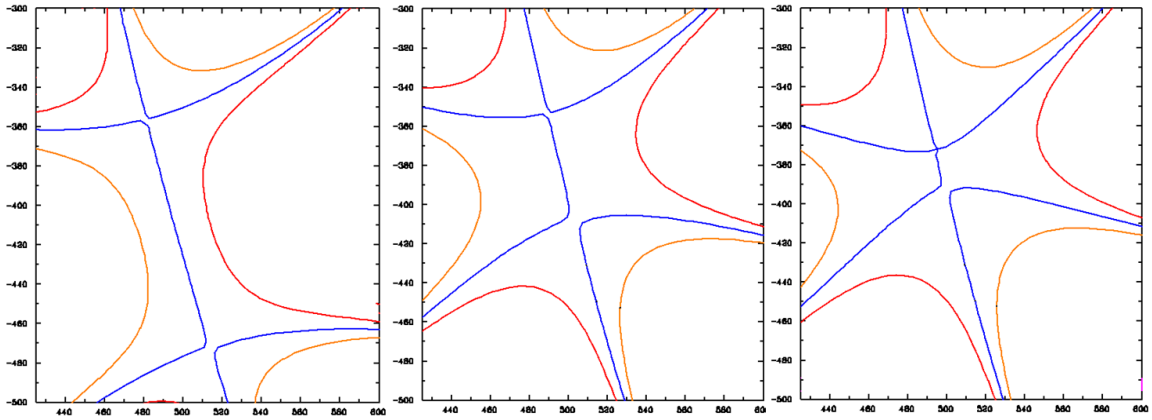

Figure 20: Three X-Divertors with different lengths of divertor leg. Regardless of leg length, the flaring of the SOL flux tube is qualitatively the same. Therefore, leg length is not a suitable criterion for advanced divertor classification.

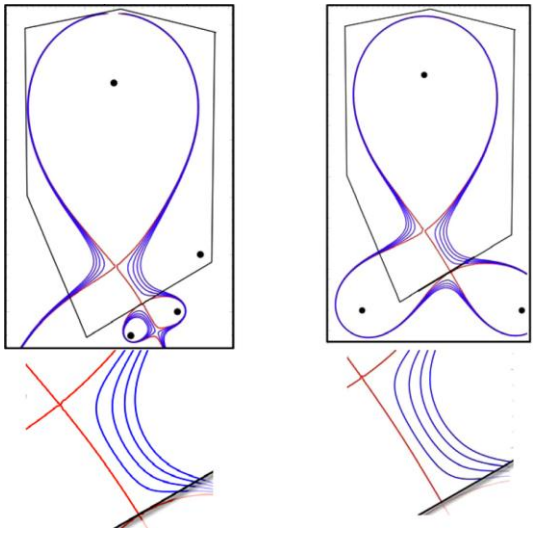

Figure 21: Two X-Divertors with identical qualities in the SOL, created with two different wire current configurations (shown as black dots). There are infinitely many magnetic configurations that can create identical geometries within the vacuum vessel, making the current distribution and the external magnetic configuration unsuitable (and irrelevant) criteria for advanced divertor classification.

It is in the search for a defining metric for advanced divertors that flux tube flaring becomes central. Let us examine how the SOL flux tube varies over space from the divertor throat (i.e., at the main x-point) downstream to the target. In Fig. 22, three representative cases – a standard divertor, an X-Divertor, and a Snowflake Plus Divertor – are presented.

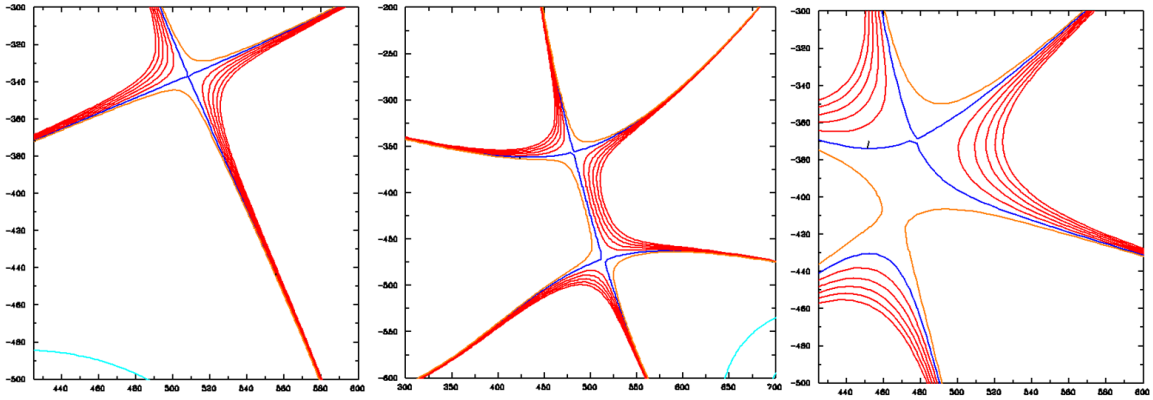

Figure 22: Three representative divertor geometries with which to examine advanced divertor classification: a standard divertor (left), an X-Divertor (center), and a Snowflake Plus Divertor (right).

It makes sense that we should first examine the standard divertor, as it is the simplest geometry, and will provide the basis for our new metric. B_P vanishes at the main x-point of the SD and increases linearly with distance d away from it, toward the target:

$$B_{P,SD} = \alpha d \tag{11}$$

Where α is some proportionality constant. We know that flux expansion is inversely proportional to B_P, so flux expansion in the SD is decreasing as one moves away from the main x-point, and the flux tube is contracting, not flaring. We will quantify this change in B_P over distance by the ratio d/B_P.

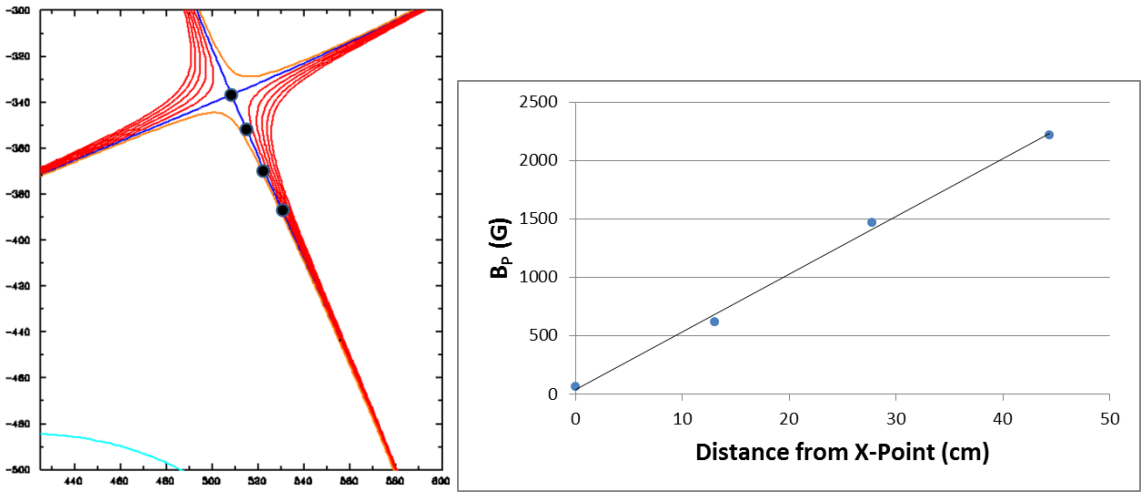

Figure 23: In a standard divertor, B_P increases linearly as one moves away from the main x-point. Because B_P increases, by flux conservation, the area of the SOL flux tube contracts downstream.

For an SD, this ratio is constant at $1/\alpha$. If B_P increases more rapidly over d, then the ratio will be smaller, and the flux tube will contract more rapidly than for the SD. If B_P increases less rapidly over the length scale d, then this ratio will be larger, and the flux tube will contract less rapidly than the SD. If B_P actually begins to decrease downstream, then the ratio will be larger still, and the flux tube will flare out, rather than contract. In this way, when calculated from the target strike point, we obtain a simple way to quantify the net contraction or flaring of an advanced divertor's flux tube relative to that of a standard divertor. This ratio is the rudiment of a classifying metric to be called the Divertor Index (DI) [12].

To normalize the divertors of different tokamaks at different length scales, we can divide the ratio d/B_P at the target by d/B_P at the point nearest the main x-point along the same flux surface, at the beginning of the divertor region (Fig. 24). In this way, the rate of change of the flux tube at the target is measured against its initial rate of change at the main x-point, without units. This normalized ratio is known as DI_{SOL}.

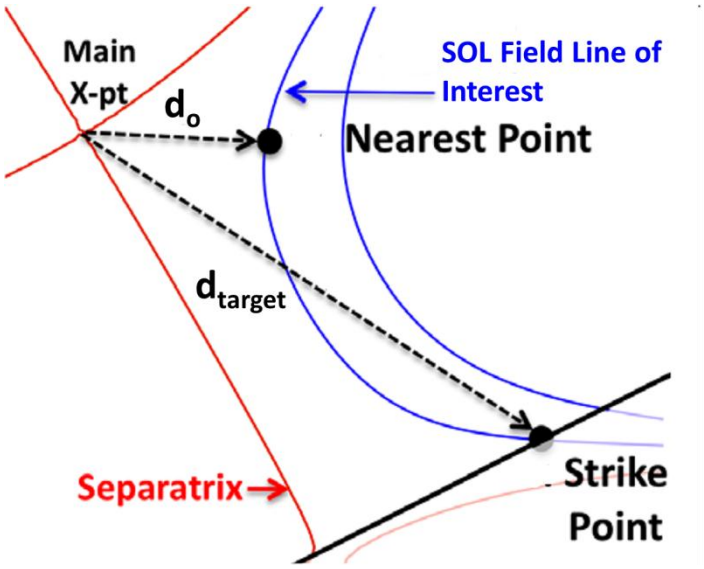

Figure 24: An illustration of the lengths relevant to calculating DI_{SOL} and measuring flux tube flaring. DI_{SOL} is a normalization of the rate of $d_{target}/B_{P,target}$ by $d_o/B_{P,o}$ at the divertor throat. To specify distances, a field line of interest has to be specified. This is usually the field line corresponding to the point of peak heat flux at the target.

$$DI_{SOL} \equiv \frac{d_{target}/B_{P,target}}{d_o/B_{P,o}} = \frac{d_{target}}{d_o}\frac{B_{P,o}}{B_{P,target}} \tag{12}$$

Because B_P of an SD increases linearly away from the main x-point, the normalizing factor $B_{P,o}/d_o$ will always equal α, and therefore $DI_{SOL,SD} = 1$ always. For an advanced divertor whose flux tube contracts less rapidly than an SD, $1 < DI_{SOL} < \infty$, and for an advanced divertor whose flux tube contracts more rapidly than an SD, $0 \leq DI_{SOL} \leq 1$. From this perspective, advanced divertors are divided into two all-encompassing classes based on the poloidal flaring in the divertor SOL, with the standard divertor serving as the base case.

Not knowing exactly the point of closest approach to the main x-point along a particular flux surface, it may be more practical to consider the limit when this point coincides with the main x-point. That is, let $d_o \to 0$:

$$\lim_{d_o \to 0} DI_{SOL} = \frac{d_{target}}{B_{P,target}} \lim_{d_o \to 0} \frac{B_{P,o}}{d_o} = \frac{d_{target}}{B_{P,target}} \lim_{d_o \to 0} \frac{\left|\nabla B_{P,o}\right|}{1} = \frac{d_{target}}{B_{P,target}} \left|\nabla B_{P,xpt}\right|$$

Where the normalizing factor $B_{P,o}/d_o$ has now been replaced by $\left|\nabla B_{P,xpt}\right|$, the square root of the Jacobian determinant of the poloidal field at the main x-point:

$$\left|\nabla B_{P,xpt}\right| = \left|\frac{\partial B_R}{\partial R}\frac{\partial B_z}{\partial z} - \frac{\partial B_R}{\partial z}\frac{\partial B_z}{\partial R}\right|_{xpt}^{1/2}$$

This version of the Divertor Index is known simply as *DI*, and it is the version that will be used for the remainder of this work:

$$DI \equiv \left|\nabla B_{P,xpt}\right| \frac{d_{target}}{B_{P,target}} \tag{13}$$

Let us now examine our three advanced divertor geometries through the lens of the Divertor Index with its focus on flux tube flaring.

The X-Divertor utilizes a secondary x-point located in the downstream SOL of the divertor to achieve flux expansion at the target; what effect does this have on flux tube flaring? Because the x-point is located downstream of the main x-point, B_P is forced to decrease as the secondary x-point is approached (where $B_P = 0$). Depending on how close the secondary x-point is to the target, this means that the plasma-relevant flux tube

upstream of the target will once again flare out, or at least contract less rapidly compared to the SD (Fig. 25). An X-Divertor is then any advanced divertor where $DI > 1$, per our previous characterization of flux tube flaring.

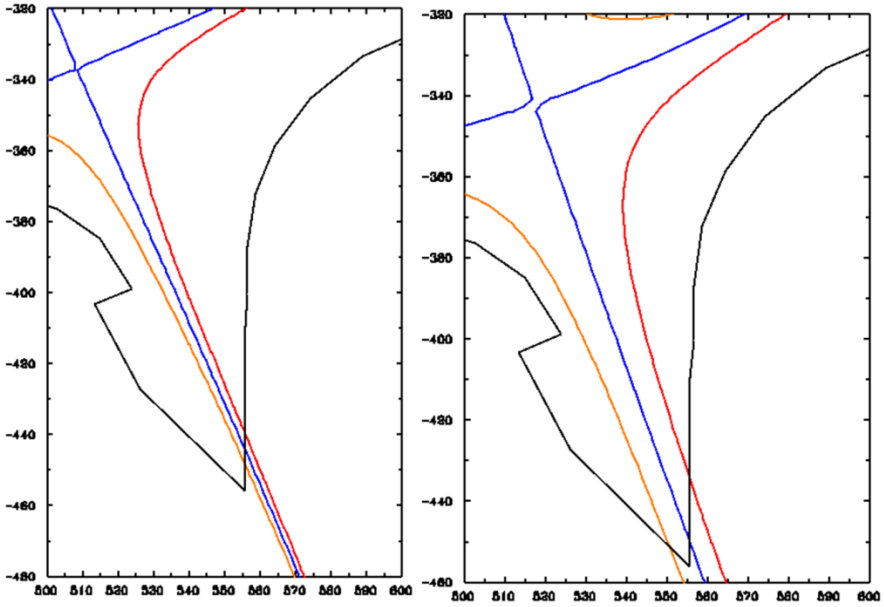

Figure 25: By our definition of *DI*, not all X-Divertors have to show visible flaring of the flux tube – merely more flaring than a standard divertor. The X-Divertor on the right is only slightly more flared than the standard divertor on the left, and *DI* is only slightly greater than 1.

By contrast, the flux tube of all variations of Snowflake Divertors will do quite the opposite. Large flux expansion at the main x-point is followed by a rapid contraction of the flux tube downstream toward the target. It should be re-emphasized that this does not imply poor flux expansion at the targets; all advanced divertors have the ability to improve flux expansion at the target over the standard divertor. But, because flux expansion in a Snowflake is maximal at the main x-point, the relative contraction of the flux tube is much more rapid than for an SD. A Snowflake Divertor is then any advanced divertor where $DI < 1$.

If the SD, XD, and SF run the gamut of *DI*, then where does a Super X-Divertor fit into the spectrum? It's important to note in the definition of *DI* that changes in the magnetic field are restricted to the poloidal plane, the implicit assumption being that $B_T \propto R^{-1}$ will not change appreciably in the relatively short leg of an SD, XD, or SF. Because the SXD uses multiple secondary x-points to take the divertor leg out to a larger major radius, however, its flux tube does see an appreciable drop in B_T. This is significant, as B_T is the dominant component of B at the target, causing a more rapid increase in the projected flux tube area of Eq. 9 than poloidal flux expansion can alone. Thus, a Super X-Divertor can be characterized as having a flaring flux tube in the poloidal plane due to its multiple, downstream x-points (i.e., $DI > 1$), but also having significant toroidal flux expansion as well due to its strike point's large major radius. Starting from Eq. 9 and assuming $B_T >> B_P$, one can show that this toroidal flux expansion is approximately proportional to R_{target}/R_{up}, the major radius at the strike point over the major radius at the point of entry of the exhaust plasma upstream.

It is clear that the value of *DI* for a divertor will vary greatly depending on the location of the strike point, i.e. where the target intersects the SOL. This is only natural, since our interest is in the physical behavior of the SOL plasma, and not anywhere outside it. Therefore, it's logical to think that moving the target to a different region of the SOL will result in different interaction with the flux tube, and *DI* reflects this difference in its choice of strike point. In fact, were the target brought right up to the main x-point, all three classes of divertors would be barely distinguishable, as the limit of *DI* for all three cases approaches 1. This is sensible, for if there's hardly any length to the divertor leg, there can hardly be any significant flaring or contracting of the flux tube in such a short interval.

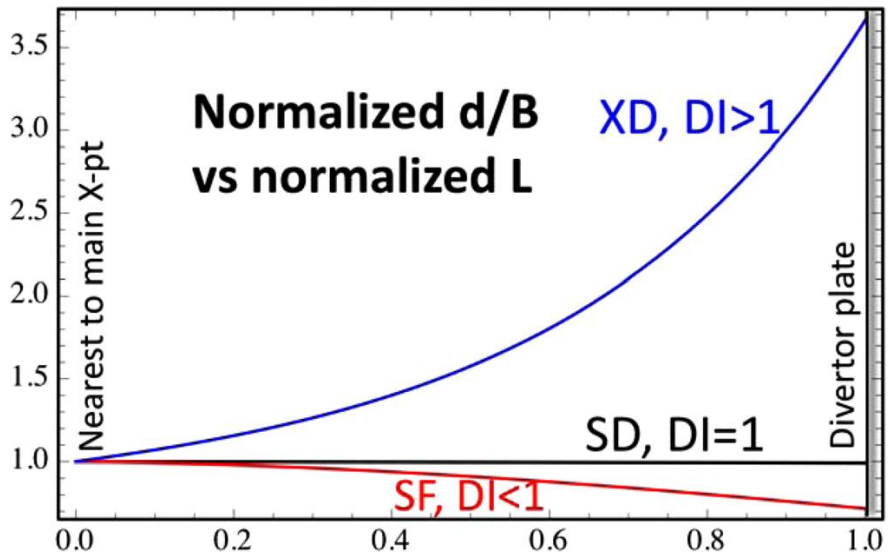

Figure 26: A profile of *DI* along the normalized length of a standard divertor, XD, and SF. The value of *DI* depends greatly on where one measures it, and the character of the different advanced divertors is revealed in the divergent behavior of their respective profiles downstream. Conversely, all of the divertors approach the same limit of *DI* of 1 close to the main x-point, making them virtually indistinguishable there.

This is precisely the sort of practical characterization of divertors *DI* offers us which our previous, informal characterizations could not – one based on the actual divertor action in the SOL.

The continuous nature of *DI* also offers us a different kind of glimpse of advanced divertors – namely, that they do *not* represent any sort of phase transition in the magnetic geometry, but can be derived in a continuous sequence of small changes to the magnetic field. That is, an advanced divertor with *any* strength of flux expansion and flaring is theoretically possible, and one can make perturbative changes to a standard divertor to improve flux expansion and flaring, bound only by the particular, practical constraints of the PF coil system of the tokamak. Viewed in another way, the standard divertor is simply a special type of advanced divertor whose secondary x-point is infinitely far away,

and the transition to an advanced divertor like an XD or a Snowflake is simply a matter of bringing that x-point to within a finite distance of the tokamak. That distance, and the improvement in performance it brings, ultimately depends on the allowances of the PF coil currents. Practically speaking, this means that almost any tokamak can stand to reap some benefit from the rearrangement of the current distribution in its PF coils. The notion that any degree of flux expansion or flaring from advanced divertors necessitates major changes to the PF coil system is incorrect, a fact that may benefit the operation of several tokamaks.

Chapter 5:

Essential Physics of the Scrape-Off Layer

5.1. A Brief Description of the SOL

In some sense, the physics of the magnetic field structure is simple compared to the plasma physics taking place within it. In the SOL plasma, ions and electrons are guided by their gyro-orbits along magnetic field lines, approximated in this work by magnetohydrodynamic multi-fluid theory. Beyond the extent of the SOL plasma, "cold" neutral gases exchange energy with the plasma, the wall, and each other, governed by ordinary statistical mechanics. And everywhere, a zoo of atomic processes is pervasive: recombination, ionization, scattering, charge exchange, atomic and molecular radiation, physical sputtering, chemical sputtering, deposition, etc. For each such process, atomic data for every charge state of every species present must be available to accurately model the interaction.

It will come as no surprise then that analytical understanding of these collective processes is extremely limited, and the vast majority of input that goes into numerical models comes from empirical relationships derived directly from experimental data. Consequently, the characterization of the SOL plasma presented here will be largely based on observation and not on first principles.

The SOL is, of course, the connection between the hot plasma core and the cold tokamak wall. Consequently, there must be large, parallel gradients in plasma density and temperature to insulate one from the other. In simpler models, the SOL can be reduced to one dimension parallel to the field lines; while crude, this visual is illustrative for understanding the journey of plasma into and through the SOL.

On the upstream end of our 1D picture, exhaust plasma may cross the separatrix and enter the SOL flux tube anywhere along the edge of the core. Obviously, a colder, denser exhaust plasma upstream would provide more favorable conditions for heat flux mitigation downstream, but this desirable SOL condition conflicts with the hot, H-mode-confined plasma we seek in the core, like that of Fig. 27. Typically, to help maintain the H-mode transport barrier, the edge density does not exceed ~1/3 the peak density in the core.

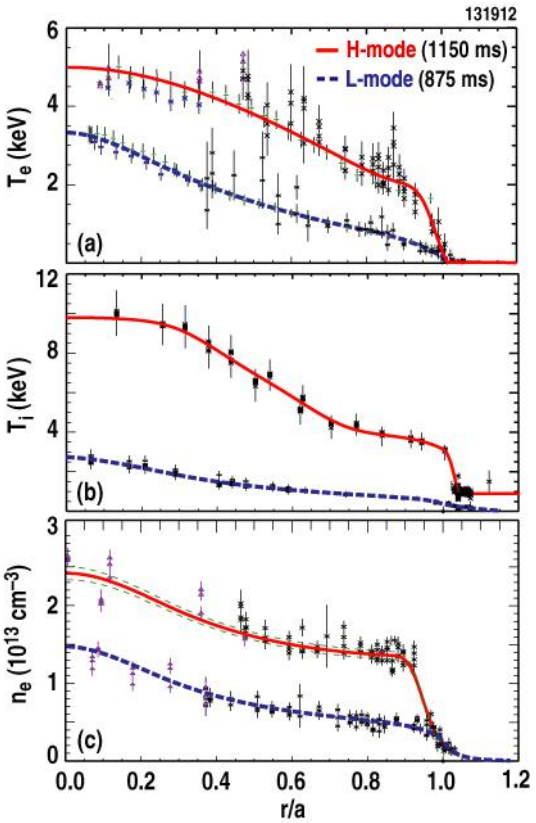

Figure 27: H-mode plasmas are defined by sharp gradients in density and temperature near the edge of the plasma, indicative of a transport barrier that prevents the cross-field migration of plasma. Figures courtesy of L. Schmitz (UCLA) *et al* [13].

Besides constraints on edge density, we can also expect a minimum power into the SOL, P_{SOL}, as a result of the heating power needed to maintain the H-mode. This value varies greatly from tokamak to tokamak, but from energy conservation we can expect that:

$$P_{SOL} \cong P_{heat} + P_{\alpha} - P_{rad} \tag{14}$$

Where P_{heat} is the heating power into the plasma core, P_{α} is the power generated from fusion alpha products, and P_{rad} is the power leaving the core in the form of radiation.

Aside from steady-state power fluxes, H-modes have also introduced ELMs to the SOL, which can drastically spike the incident heat at the targets in short, intense bursts. ELMs are quasi-periodic, and have been shown to coincide with a temporary relaxation of the H-mode transport barrier, releasing more energy from the core into the SOL. To date, ELM mitigation is limited to methods that increase their frequency, thereby decreasing their intensity.

At the other end of the SOL flux tube, the plasma interacts with the material surface of the targets. The environment here is notably different than that upstream; ideally the plasma has cooled due to radiation and neutral interaction along its connection length. The ionization fraction is lower, and neutral densities tend to be higher, making the region around the strike points desirable for pumping. The plasma forms a sheath at any material interface, a very narrow region at the solid surface notably un-fluid-like in its behavior. At the initiation of the plasma, the far less massive electrons move ahead of the ions and inject themselves into the solid targets. This causes a negative electrostatic charge to build up on the surface, repelling electrons and accelerating ions. A dynamic

equilibrium is quickly reached, and the sheath is established. The extent of the sheath, also known as the Debye sheath, is only a few Debye lengths, where the Debye length is given as $\lambda_D \approx \sqrt{\frac{\varepsilon_o k_B T_e}{n_e q^2}}$ when neglecting ion mobility. The most important consequence of the Debye sheath is that the traditional plasma fluid equations will not apply in this region, since the ions and electrons are not collisional there. Therefore, the sheath region will have to be treated specially in models of the SOL.

If the plasma fluid equations cannot accurately model the Debye sheath due to un-fluid-like behavior in that region, it's worth questioning whether there are other regions of the SOL where a fluid approach is inappropriate, or whether the entire SOL itself is suitably modeled as a fluid. For a fluid approach to be valid in the SOL, the plasma must be collisional and conductive; that is, all the characteristic length scales in the fluid equations must be smaller than the connection length. This includes the ion and electron mean free paths, as well as the heat conduction length. For this work, this does *not* include the mean free path of neutrals, since neutrals will be modeled separately via stochastic modeling. That the plasma is collisional and conductive is generally satisfied in the SOL, with the possible exception of the ends of the flux tube of interest – at very high temperatures at the upstream midplane, and at very low temperatures near the targets downstream. In such cases, some source terms in the energy equation may become inaccurate. To counter this, a simple correction is available in our transport modeling code to place limits on the ion heat fluxes, electron heat fluxes, and viscosity sources in the plasma. However, there is a dearth of experimental knowledge with which to choose appropriate values for these limits, and their values may affect heat flux and temperature profiles at the targets (Fig. 28). Therefore, parametric scans of these limits are necessary to draw any predictions from modeling results.

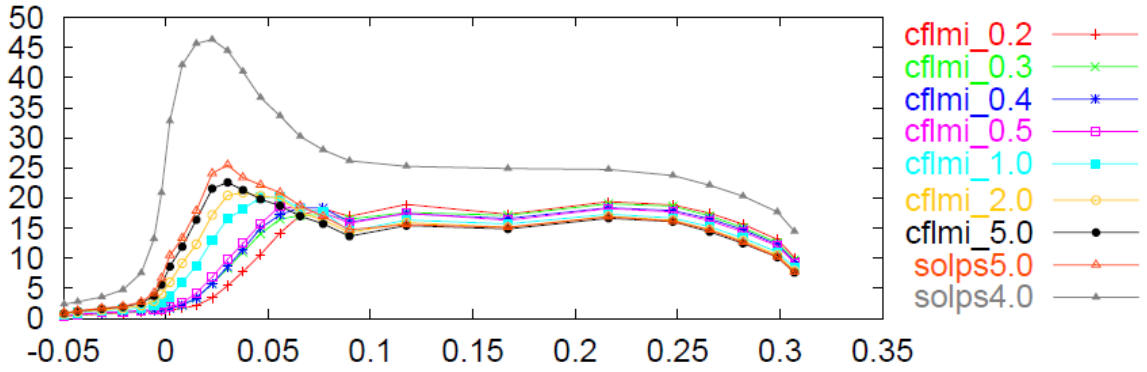

Figure 28: The choice of different values for the ion flux limit can result in differences in the profiles at the targets. Figure available in the SOLPS manual [14].

Despite the fact that the plasma near the targets is colder and denser than upstream, intense heat fluxes and temperatures can still exist. Physical sputtering of the targets occurs when fast-moving ions and electrons inject themselves into the solid surface, ejecting target material atoms into the plasma. Chemical sputtering occurs when plasma species interact chemically with target material atoms, especially carbon, to form new compounds. Left unchecked, both types of sputtering contribute to the erosion of the targets and the contamination of the core plasma with high-Z impurities.

5.2. The Role of Impurities

Though they may only comprise about 1% of the ions present, impurities can have a strong effect – either beneficial or harmful – on the power balance in a tokamak plasma. Because of their much higher atomic numbers over hydrogen, impurities have the potential to strongly radiate energy isotropically. The intensity of this radiation increases rapidly with atomic number by $\sim Z^2$. In the SOL, this effect is beneficial in directing energy away from the divertor targets, but it also removes energy from the core, by Eq.

14. Naturally, impurities don't discriminate where they travel; in some cases, impurities actually tend to collect in the core.

Impurities are an inevitable reality in fusion plasmas due to physical and chemical sputtering, especially at the targets. For targets comprised mostly of carbon, where $Z = 6$, impurity radiation from the core can be relatively weak, where the carbon ions are fully stripped of their valence electrons. However, a recent shift in interest to tungsten targets, where $Z = 74$, reinforces concerns about high plasma temperatures in the divertor leading to impurity contamination and excessive core radiation. As a compromise, some tokamaks employ boronization, where a thin coat of boron is applied over the higher-Z wall/target material. The expectation is that the higher-Z metal will still be able to absorb the divertor heat fluxes, while the boron layer will be eroded away first, which is preferable to the erosion of the metal itself.

Despite these downsides, almost all tokamaks employ systems to purposely inject high-Z noble gases, such as neon and argon, as radiating impurities. These impurities can effectively redirect energy in the SOL away from the targets by radiation. It is important to remember, however, that the radiation is isotropic, so as much as 50% of the radiated power can be incident back on the target (Fig. 29); a responsible assessment of divertor power loads should take this figure into account. Furthermore, the power radiated away from the targets does not simply vanish; one must determine whether the radiation loads on the surrounding first wall components is acceptable.

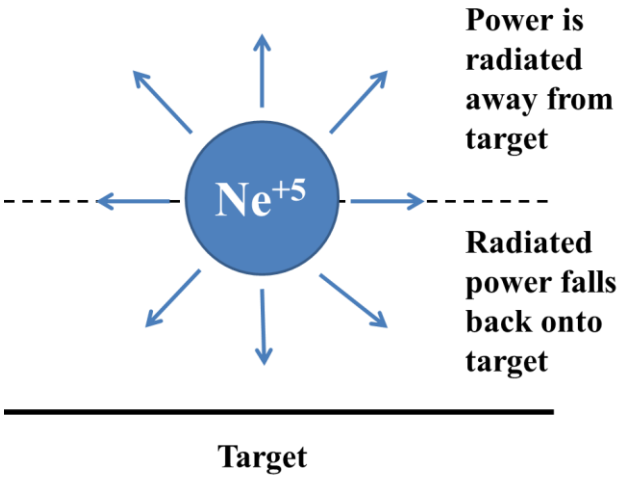

Figure 29: Radiating impurities serve to redirect power in the SOL away from the targets, but because this radiation is isotropic, as much as 50% of the radiated power can end up back at the target anyway.

. Because of the strong relationship between radiation and Z, it becomes important to keep track of the effective Z of the core plasma:

$$Z_{eff} = \frac{\sum_i n_i Z_i^{\,2}}{\sum_i n_i Z_i} \tag{15}$$

Where the n_i and Z_i are the densities and atomic numbers of each atomic species present, no matter the charge state. If only deuterium and tritium ions are present in the core, then Z_{eff} is, of course, exactly 1. But with the addition of higher-Z impurities, Z_{eff} will begin to increase according to their relative density in the plasma. A typical range for the maximum Z_{eff} in the core is 1.3 – 2.0. Beyond this, core radiation usually becomes unacceptably high.

5.3. THE SOL WIDTH

Accepting that exhausted energy and particles into the SOL are inevitable, it becomes pertinent to ask: to what extent does this exhaust plasma pervade the SOL? We know from the Lorentz force, $\vec{F} = q\vec{v} \times \vec{B}$, that ions and electrons freely travel parallel to the magnetic field, but what about travel perpendicular to the field? The Lorentz force alone does not permit perpendicular travel, so it's unsurprising that $v_{perp} \ll v_{parallel}$, where $v_{parallel}$ can be of the order of the sound speed, while v_{perp} may only be a few millimeters per second. How far then do ions and electrons manage to travel in the radial direction before they collide with the targets downstream, and what mechanisms dominate their travel in this direction? That is, what is the effective width of the SOL, beyond which no appreciable amount of plasma and/or heat can be found?

The exhaust plasma into the SOL doesn't necessarily constitute a heat flux problem itself; it is the narrow channel through which the heat is concentrated that creates the problem. As better confinement has, by definition, reduced cross-field transport in the core, so too has it reduced cross-field transport in the SOL, narrowing the SOL width and exacerbating the divertor heat flux problem. What's worse, predictive scaling laws for the SOL width of various tokamaks have been difficult to formulate, and those that exist today are not without controversy, given that the SOL width is determinant of a tokamak's allowable operating window.

There is a distinction between the cross-field transport of particles and the cross-field transport of energy. The e-folding width of the cross-field electron density profile has been experimentally observed to be much longer than the power width, about 3.5 times longer. Unsurprisingly, it is the power SOL width that is relevant to the heat flux problem, though the density SOL width becomes an important factor in our SOL modeling effort later. Virtually nothing is known about the individual cross-field heat and

particle diffusivities, X and D, including how they may vary throughout the plasma. For most modeling purposes, their values are taken to be constant. In fact, most cross-field transport is *anomalous* – as of yet unexplained – the prevailing school of thought being that it arises from turbulence driven by microinstabilities in the plasma.

In 2011, R.J. Goldston developed a heuristic model for the power SOL width [4]:

$$\lambda_q = 5671 \cdot {P_{SOL}}^{1/8} \frac{(1+\kappa^2)^{5/8} a^{17/8} B^{1/4}}{{I_P}^{9/8} R_o} \left(\frac{2\bar{A}}{1+\bar{Z}}\right)^{7/16} \left(\frac{Z_{eff}+4}{5}\right)^{1/8} \quad (SI\ units) \qquad (16)$$

where

$$\bar{A} \equiv \frac{\sum_i n_i A_i}{\sum_i n_i}$$

and

$$\bar{Z} \equiv \frac{n_e}{\sum_i n_i}$$

Where A is the atomic mass, B is measured at the plasma major radius, and summations are over all ion species and charge states. In this model, the electron drift speed sets the radial extent of the density SOL width. If instead the ion drift speed sets the extent, then there is an extra factor $\bar{Z}^{-7/8}$ on the expression in Eq. 16. It is ambiguous at this time which drift speed is more important.

Even measurement of the power SOL width carries with it some ambiguity. From where along the separatrix does one measure the radial power profile? Energy is being deposited into the SOL everywhere around the core edge, so where is it appropriate to say that all of the energy is accounted for? One could be tempted simply to look downstream at the target heat flux profiles, but not all the SOL energy is represented there either.

After all, if the divertor is doing its job properly, a significant fraction of the SOL power should be dissipated before it reaches the targets.

While there is no universally agreed upon method to measure the SOL width, in this work, it is measured directly from the outboard midplane upstream. At this location, the power SOL width will be defined as the radial distance from the separatrix at which the peak heat flux drops by a factor 1/*e* in the radial heat flux profile (Fig. 30). In this way, we do not lose power to radiative and cooling processes in the divertor itself, muddling the heat profile. The downside to this definition is that we cannot be sure the upstream peak heat flux will map directly to the same flux surfaces downstream, at the targets. This is, after all, the practical concern over the SOL width – how the heat is distributed over the target plate. Nevertheless, it is the least ambiguous way to standardize measurement of the SOL width over many tokamaks, and one that is available in a simulation environment.

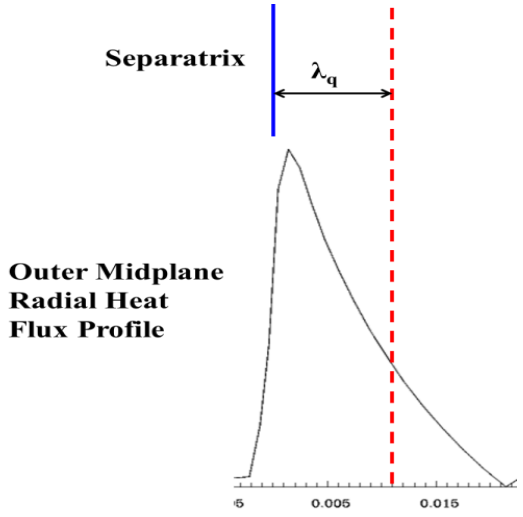

Figure 30: In this work, the power SOL width is measured as the e-folding width of the radial heat flux profile at the outer midplane.

5.4. DETACHMENT

Aside from cooling the SOL plasma and increasing the plasma-wetted area on the divertor targets, the third stated goal of advanced divertors is to open operating regimes for stable, full detachment. Experimentally, detachment is observed, at the target, by a marked drop in the ion and electron fluxes, an increase in neutral gas pressure, increased radiation, plasma temperatures < 5 eV, and a reduction in the peak heat flux. All of these phenomena are consistent with the SOL plasma "detaching" from the targets, and a neutral gas buffer zone forming between them.

Acceptable divertor heat loads brought upon by stable, full detachment is the "holy grail" of divertor physics and design; it not only represents a state in which the core has been isolated from the tokamak walls, but also in which the SOL plasma has been isolated. This also serves to eliminate the concern over "hot spot" formation at the targets; if the plasma is no longer attached to the targets, then the anisotropy of the parallel heat flux is eliminated, and target-field angle of inclination becomes a moot point (Fig. 31).

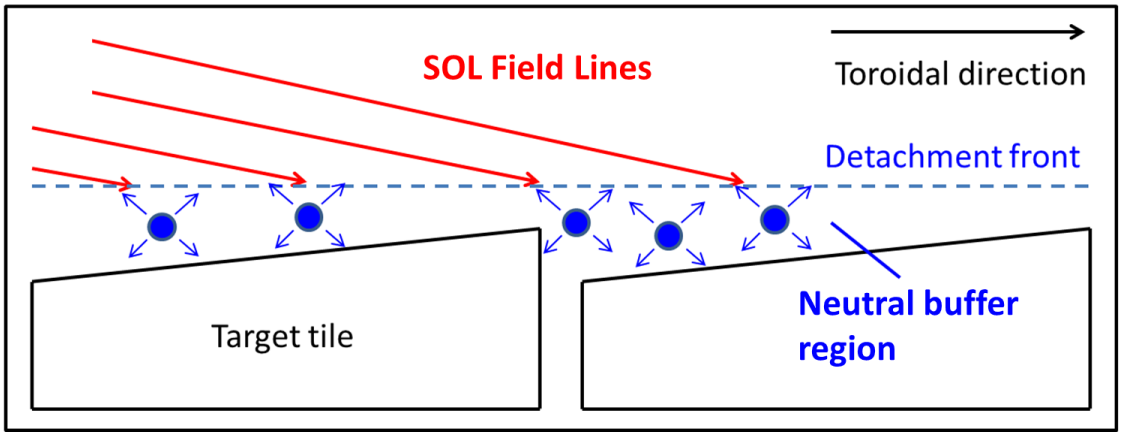

Figure 31: A stably detached plasma theoretically makes the heat flux issue moot by separating the SOL plasma from the targets. The issue of the target angle and hot spot formation also becomes moot, as neutrals in the buffer region are not influenced by magnetic field lines.

Full detachment has been achieved experimentally, but never stably. By closely controlling gas puffing rates, tokamak plasmas have been observed to alternate between attached and detached states in an oscillatory fashion. Long periods of time in detachment, however, have led to loss of energy confinement in the core, particularly near the main x-point. Detachment may also be responsible for the onset of MARFEs, or "multifaceted asymmetric radiation from the edge."

It is hypothesized that loss of energy confinement from the core during detachment may result from migration of the detachment front away from the divertor target, back to the main x-point. In other words, a detachment front in a standard divertor is not observed to be content residing somewhere near the divertor target, but instead moves inward to quench the entire divertor leg, until ultimately even the core is negatively impacted. In this dissertation, it is hypothesized that there is a readily understood, *magnetic* cause behind the instability of the detachment front in a standard divertor. Indeed, our earlier effort to make a sharp distinction in flux tube flaring, and not

just flux expansion, between different classes of advanced divertors may be critically important to detachment front stabilization.

Let us first build a simple illustration of the onset of detachment in a standard divertor, based on readily grasped physics principles. Detachment begins at the targets when a neutral-dominated layer buffers the SOL plasma from the solid surface. From our previous description of the standard divertor via the Divertor Index, we know that its flux tube contracts as one moves *downstream* toward the target, meaning that if one were to move *upstream* from the targets instead, as the detachment front would, one would see a flaring of the flux tube. Let us consider the potential consequences of this geometry on the divertor plasma as the detachment front migrates upstream, as it does in Fig. 32:

1. The divertor plasma, with some given energy coming downstream, is distributed over an ever-widening surface area at the detachment front, reducing its local energy density and enhancing cooling via radiation. This further encourages recombination and expansion of the neutral buffer region.
2. Because the surface area at the detachment front widens, there is also more contact area between the divertor plasma and the neutral buffer, increasing the rate of heat exchange and cooling of the divertor plasma. This further encourages recombination and expansion of the neutral buffer region.
3. The upstream migration of the detachment front erases in its wake part of the SOL plasma's trajectory toward the targets, reducing total connection length. Consequently, the parallel plasma pressure is decreased, reducing the rate of heat exchange between plasma and neutrals at the detachment

front. This effect actually *discourages* expansion of the neutral buffer, and is a stabilizing force against the migrating detachment front.

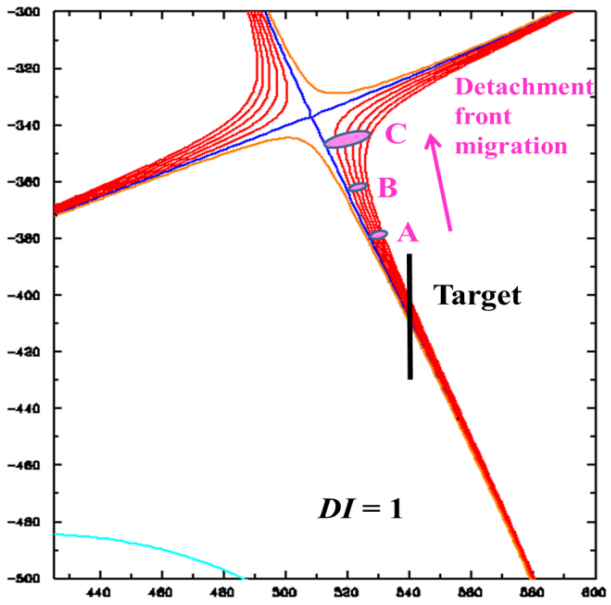

Figure 32: In a standard divertor geometry, as the detachment front moves upstream from Point A to Point B to Point C: (1) there is reduced energy density as the plasma front is spread out over a larger area, and (2) there is greater contact area between the plasma and the neutral buffer, encouraging further cooling. These mechanisms serve as positive feedback for unstable upstream migration of the detachment front.

With the exception of Point #3, it becomes clear then why divertor detachment may lead to MARFEs and loss of core energy confinement: the magnetic geometry of the standard divertor gives positive feedback to the growth of the neutral-dominated region. If this is the case, then flux tube flaring and the Divertor Index become more than a means of classifying divertors; they become indicators of detachment behavior.

Extrapolating what we've learned from the standard divertor, we conclude that Points #1 and #2 provide an even stronger positive feedback for detachment front migration if $DI < 1$, as in the Snowflake Divertor (Fig. 33). Because the divertor flux tube

contracts even more rapidly downstream, a detachment front will see a more rapidly flaring flux tube as it pushes upstream, resulting in a bigger contact area between the plasma and neutrals, and a lower plasma energy density. As for Point #3, while the loss of connection length will always provide negative, stabilizing feedback against runaway detachment, a smaller portion of the total line length is lost near the targets in the Snowflake, where B_P is rapidly increasing. The negative feedback near the targets is weaker than for the standard divertor. All of these points suggest that operation of a Snowflake Divertor in detachment would be even less stable than for the standard divertor, for which there is already no known stable window.

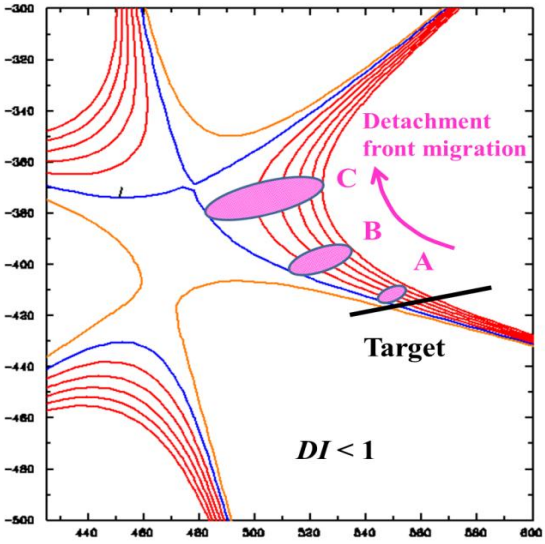

Figure 33: Even though the Snowflake offers the benefit of flux expansion at the target over the SD in Fig. 32, its rapidly contracting flux tube downstream suggests an even more rapidly migrating detachment front upstream.

Conversely, the flared geometry of a strong X-Divertor, where $DI >> 1$, works against the detachment front, encouraging it to stabilize between the target and the divertor throat (Fig. 34). Starting from the target, the detachment front sees a narrowing

flux tube upstream, where plasma energy density is increased, the plasma-neutral contact area is decreased, and the plasma is encouraged to keep "burning through" the detachment front. Finally, a larger percentage of the total connection length is erased by a migrating detachment front in an XD, due to the lower poloidal field in the vicinity of the target. Per Point #3, the parallel plasma pressure is decreased more rapidly, and the stabilizing feedback is strengthened. This beneficial geometry is a direct consequence of the secondary x-point being located in the downstream SOL, closer to the strike point.

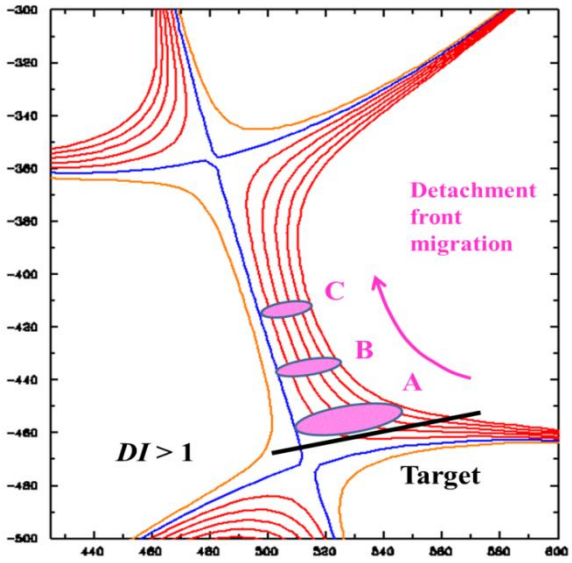

Figure 34: Unlike the standard divertor and the Snowflake Divertor, the flaring geometry of the X-Divertor causes the detachment front to contract (or at least, expand less rapidly than an SD) as it migrates upstream. From A to B to C, the front sees a concentration of the energy density in the plasma, and a reduced area of interaction between the plasma and the neutral buffer, working against the continued upstream migration of the front.

At the very least, for *DI* only modestly greater than 1, where the flux tube still contracts downstream, but less so than for the standard divertor, the positive feedback acting on the detachment front is less strong. In such a case, where greater values of *DI*

cannot be feasibly obtained, stabilization of the detachment front could possibly be brought within the realm of active gas feedback controls.

The arguments in favor of the X-Divertor as a means of achieving stable detachment are stronger still for the Super X-Divertor, where all of the same physics principles apply, but now the toroidal field at the strike point is reduced as well. As an outboard SXD detachment front migrates upstream, it sees a strong increase in the toroidal field according to the R^{-1} relationship, and a contraction of the divertor flux tube in the toroidal direction.

If the evolution of detachment is indeed affected by magnetic geometry, specifically flux tube flaring, then advanced divertors with terrific flaring and $DI >> 1$, the XD and SXD, may be able to arrest the detachment front before it migrates to the plasma core.

We have now established what we need to know to understand the interplay between the external magnetic fields produced by the tokamak coils and the plasma via the Grad-Shafranov equation, and how this relationship affects fusion performance. We have rigorously developed a metric by which to distinguish advanced divertors, the Divertor Index. Having laid out a framework for understanding the mechanisms of detachment, and having found that such mechanisms may rely heavily on flux tube flaring to stabilize the detachment front, we are now strongly motivated to investigate X-Divertors and Super X-Divertors as possible means to open windows for stable divertor detachment on several different tokamaks. Not only do these divertors create flux expansion and reduce target heat fluxes, as all advanced divertors do, but for the first

time, they may actually allow the SOL plasma to isolate itself completely from the tokamak wall. For these reasons, and because of well-known modeling difficulties in the simulation codes, this work will from this point on exclude Snowflake Divertors, and will focus solely on X-Divertors and Super X-Divertors.

III. METHODS IN ADVANCED DIVERTOR MODELING

Volume III details the methods and procedures used to set up and run the scientific codes that create the computational models for advanced divertors. Furthermore, an intuition is developed for understanding how the advanced divertors are designed using real PF coils. Chapter 7 follows the entire modeling process, from the magnetic equilibrium in CORSICA, to mesh generation in CARRE and DivGeo, to transport modeling in B2.5-Eirene. Chapter 8 introduces the concept of lobes as a means of explaining x-point creation and control, as it pertains to both plasma shaping and poloidal and toroidal flux expansion.

Chapter 6:

Numerical Simulation Software and High-Performance Computing

6.1. On the Necessity for Simulations in Tokamak Research

It's worth stopping to ask where computer simulations fit into the advancement of scientific understanding. The behavior of computer models must, at their foundation, be governed by the relevant equations of theory, but very often they also rely directly on empirical data from experiments to fit parameters for which no analytical formula is available. Furthermore, because the solutions to the equations are numerical, performing a calculation becomes tantamount to collecting data, as there is no way to know *a priori* what type of solution will develop, whether that solution will have good convergence, or whether it will even be consistent with experimental findings.

Why have computational models then? Simply put, the theoretical equations involved in modern research are, for the most part, nonlinear, nasty, and almost completely lacking in known analytical solutions for realistic conditions. This is certainly no less true of magnetohydrodynamics, which already represents a simplification of the true complexity of plasma physics arising from the kinetic equation. Yet still, analytical solutions are elusive. In this way, numerical models and simulations are in a position to propel the validation of plasma theory by offering a glimpse of the form and evolution of numerical solutions. If there is some debate over whether a particular assumption is justified, or whether two different approaches to a problem are equivalent, then their numerical solutions can be directly compared.

On the experimental side, it is critical when testing out an advanced concept or design to have some assurances that the experiment won't take a disastrous toll on the

testing apparatuses. This is of particular concern in fusion research, where the damaging of multi-million- or even multi-billion-dollar tokamaks with unvetted technology is completely unacceptable. In many ways, progress in fusion over the last three decades is thanks in large part to the tremendous advances in high-performance computing, where intuition and a knowledge base of parameters based on computer models have been able to grow faster than they otherwise could have relying solely on theoretical breakthroughs and tokamak facilities several years in the making. And while the correlation should be taken with appropriate lightness, the paced progress of the fusion triple product and processor power in Fig. 35 is striking:

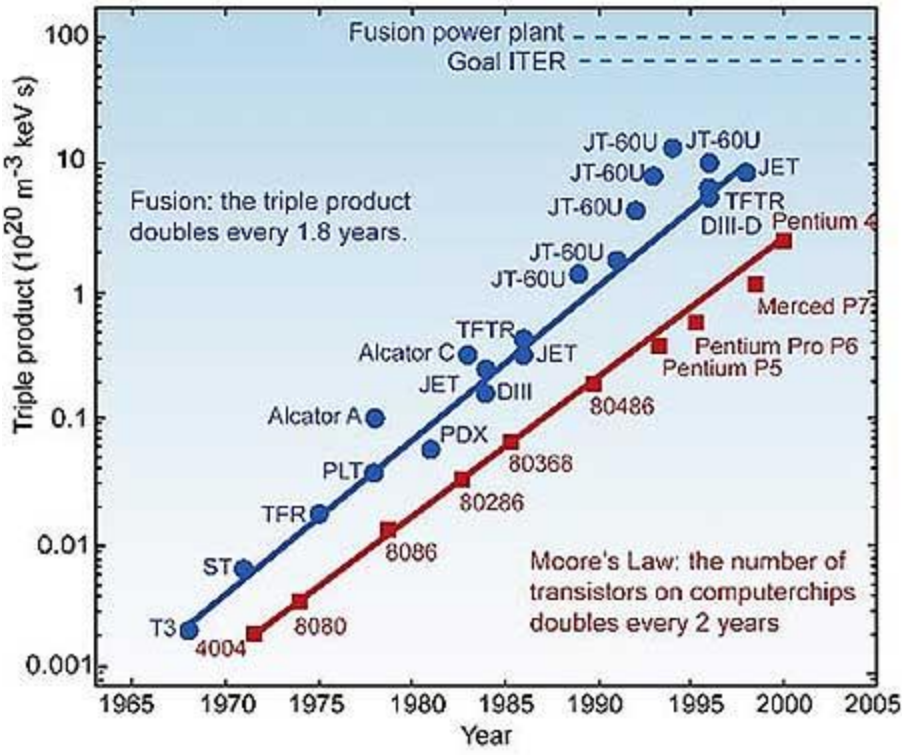

Figure 35: Progress in fusion since the 1960s as measured by the triple product. There is a strong correlation with the advancement of high-performance computing. Figure courtesy of the European Nuclear Society [15].

For the types of spatial domains we intend to model, a finite element approach is appropriate. There are definite advantages to finite element methods; the class of solutions to the weak formulation of a differential equation is much broader than its class of analytical solutions. Often, these solutions are more robust as well. Finite element methods aren't without their own pitfalls though. The accuracy of a finite element model can depend greatly on the resolution of the mesh, the grid of discrete cells on which the numerical approximations are made.

To check the accuracy of a particular solution, it must be plugged back into the differential equation it purports to solve, and then the residual, the difference between the left-hand side and the right-hand side, is calculated. For a solution to be appropriately convergent, its residual must fall and stay below some acceptable fraction of the order of magnitude of the equation terms, depending on the desired level of accuracy. An example of residual tracking is shown in Fig. 36.

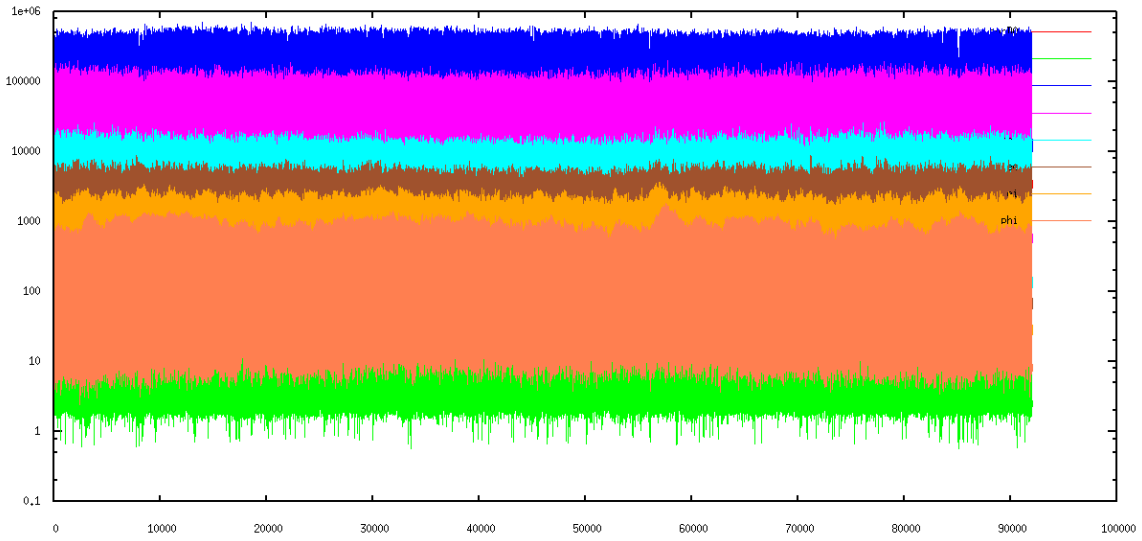

Figure 36: Residuals of the Braginskii and Maxwell's equations in a SOLPS simulation. When the solution is convergent, and the plasma is at a steady state, the residuals show no further trends over time.

Even with a well-converged solution, it's important to remember that a numerical model must always be viewed with a healthy level of skepticism. As with theory, it is critical that models be benchmarked against real experimental results. This practice not only serves to validate the model, but it also helps to refine the model by updating parameters and boundary conditions to more realistic values.

6.2. MAGNETIC EQUILIBRIA IN CORSICA

The magnetic equilibria for the XDs and SXDs were developed using the TEQ portion of the CORSICA code, originally developed at Lawrence-Livermore National Laboratory. TEQ iteratively solves the Grad-Shafranov equation for the stream function ψ on a rectangular *(R,z)* mesh in the poloidal plane, with the toroidal magnetic field at a single point specified as input to define $F(\psi)$. The solution algorithm used is based on the Grad-Hogan approach [16].

Flux profiles such as the pressure $P(\psi)$ and the parallel current $J_{parallel}(\psi)$ are also specified as input. These profiles are given as discrete points on an arbitrary number of normalized poloidal flux coordinates (ψ_{norm} = 0 on the magnetic axis, 1 at the separatrix), with the expectation that all profiles go to zero at the separatrix.

For boundary conditions, a free-boundary method is applied. That is, the location of the separatrix is not known *a priori*, and must be iteratively found. First, the total flux contributions from the plasma current, PF coils, and any passive structures are calculated so that an x-point (i.e., where $\frac{\partial \psi}{\partial R} = \frac{\partial \psi}{\partial z} = 0$), or x-points, in the case of a double-null, can be identified. It's not unreasonable that many points may exist within the mesh where $B_P = 0$, typically near the PF coils, but especially because our advanced divertors will be guaranteed to have additional x-points in their geometries. Therefore, we specify an x-

point search box for TEQ to limit its search and avoid confusion. If more than the specified number of x-points is located within the search box, the code can crash, and has. Once the x-points are properly located, the flux surface on which they reside is identified as the separatrix. The only condition applied beyond this is that $\psi(R,z)$ behave well at infinity.

Any number of additional constraints can be applied in an attempt to narrow the scope of the problem to focus on the types of solutions in which we're interested, such as those shown in Fig. 37. For example, one can specify "rigid" points, points through which the separatrix is required to pass. Obviously this is a rather hard constraint, so rigid points are usually used sparingly. Instead, "fuzzy" points may be used to provide a target shape for the separatrix. TEQ will attempt to minimize the error between the fuzzy points and the separatrix. For inductive plasmas, the total flux within the plasma can be specified, to ensure that the flux swing required by the solenoid is fixed.

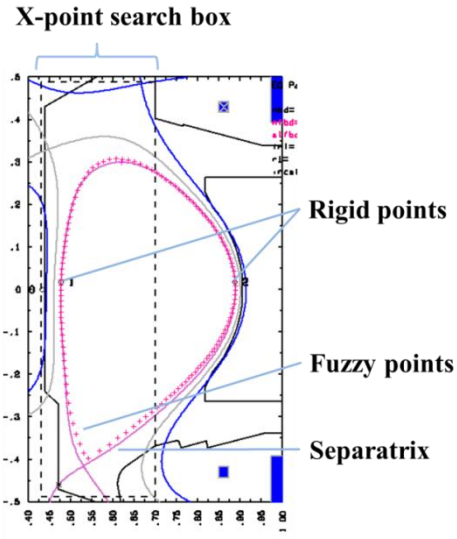

Figure 37: The use of rigid and fuzzy points provides a target for TEQ to find the separatrix. The x-point search box limits the range in which TEQ will search for the main x-point.

Finally, for disconnected double-nulls, where the two main x-points do not lie on the same separatrix, the desired distance between the inner and outer separatrices can be specified. This can also apply to single-nulls, since a single-null can be thought of simply as a disconnected double-null where the separatrices are widely separated. Often, a second x-point is used outside of single-nulls to improve triangularity.

Obviously, the more hard constraints we apply, the more degrees of freedom TEQ needs to find a solution. These degrees of freedom usually come in the form of PF coil currents. Any number of parallelogram-shaped PF coils of any size may be introduced, usually to model the coils of a real-life tokamak, like those in Fig. 38. It is in the PF coil currents that the use of TEQ becomes an art; the user must decide which coil currents to fix, and which currents to allow TEQ to vary on its way to a solution.

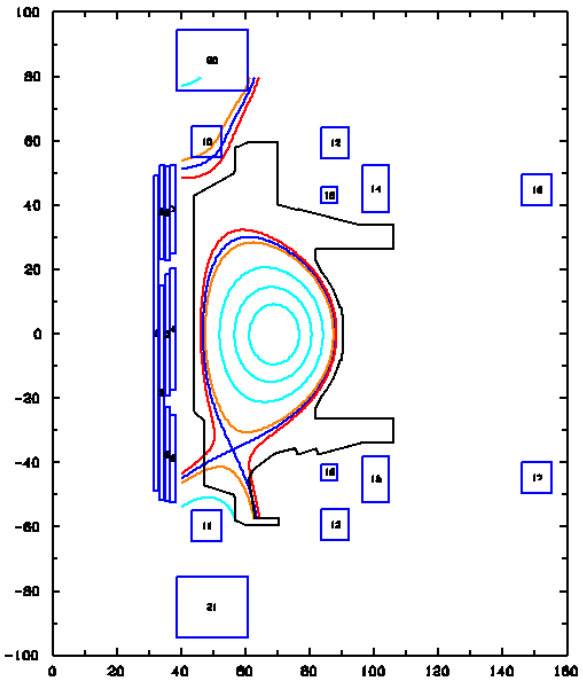

Figure 38: TEQ controls the currents of PF coils (shown as blue rectangles) to find solutions to the G-S equation. Currents are also controlled manually.

It would seem reasonable to allow TEQ to control all coil currents, but as there are limits to the specificity of the constraints, there are likely many solutions, many of which are divergent and will cause the code to crash. In other words, even the desired form of our solution is, to some degree, ambiguous, and manual control of some coil currents helps to keep the TEQ-varied coils from wandering to farcical currents. This is particularly relevant to advanced divertor development, as the original thrust of TEQ was only for the modeling of standard divertors. Therefore, we must take a particularly high degree of manual control, which makes the design process highly experiential; the user must learn to predict the topological consequences of making small changes to coil currents.

Once a suitable equilibrium has been found, the $\psi(R,z)$, the flux profiles, and the coil currents can be saved as a CORSICA file. Alternatively, they can be saved in a more universal EQDSK file, which is readable by several different MHD equilibrium codes.

6.3. MESH GENERATION IN DIVGEO AND CARRE

The equilibrium is then exported as an EQDSK file to SOLPS (Scrape-Off Layer Plasma Simulation), the suite of codes responsible for SOL plasma modeling. SOLPS consists of Carre, the quadrilateral mesh generator for B2.5; B2.5, the 2D axisymmetric MHD equation solver; TRIANG, the triangular mesh generator for Eirene; Eirene, the 3D Monte Carlo neutral modeler; and a host of smaller utilities that prepare or reformat input for use between the different codes. Because SOLPS couples the solver of the MHD equations to the Monte Carlo neutral simulator, it is arguably one of the most sophisticated axisymmetric SOL modelers in the world today. It is also the flagship SOL code for the ITER project.

As the development of SOLPS is itself an active research project, it has gone through many versions and added many new levels of sophistication, sometimes in parallel. Therefore, some versions which are still actively used include code refinements, such as drifts or neutral-neutral collisions, which other versions do not. Consequently, it can be challenging to compare two results generated by different versions of the code. An effort is currently underway to streamline the code development effort into a single version for ITER, which will be dubbed SOLPS-ITER [17]. For the purposes of this research project, where detachment modeling is so important, SOLPS 5.1 is used, which uses Eirene 2008 and includes neutral-neutral interactions. No matter the version, one thing is clear: SOLPS is *not* a user-friendly series of codes. It requires over a dozen formatted input files, and hundreds of flags and arrays are available for tweaking the physics in the code, sometimes with great effect on the end result. Close collaboration with developers and other users is highly fruitful.

The first step in SOL modeling is to generate a mesh on which the MHD equations will be solved by B2.5. A graphical user interface, called DivGeo (DG), is used to set the parameters for the mesh generator, Carre. First, the appropriate topology (SN, DN, etc.) is specified so that DG can correctly identify the different regions of the plasma on the ψ grid. Then, a series of line segments defines the structure of the surrounding vacuum vessel, first wall, and divertor targets. These lines can be created on the spot or imported. The structure defines the bounded region in which Carre will seek to generate the mesh.

For most cases, the structure is fixed and must be taken as is, but in future tokamaks, there is much greater flexibility, such as with the divertor targets. In such a case, a script was written to automatically generate target line segments which conform to a specified angle of incidence between the target and the 3D magnetic field vector at the

strike point (Fig. 39). There is one degree of freedom with this process, as a target line segment can satisfy its angle constraint by being oriented either at an angle θ_P or its supplement, $\pi - \theta_P$, in the poloidal plane. Traditionally, the target is oriented such that the end located in the SOL points toward the separatrix, not away from it. This usually requires less space, allows for more shielding, and improves neutral pressure near the targets for better pumping efficiency.

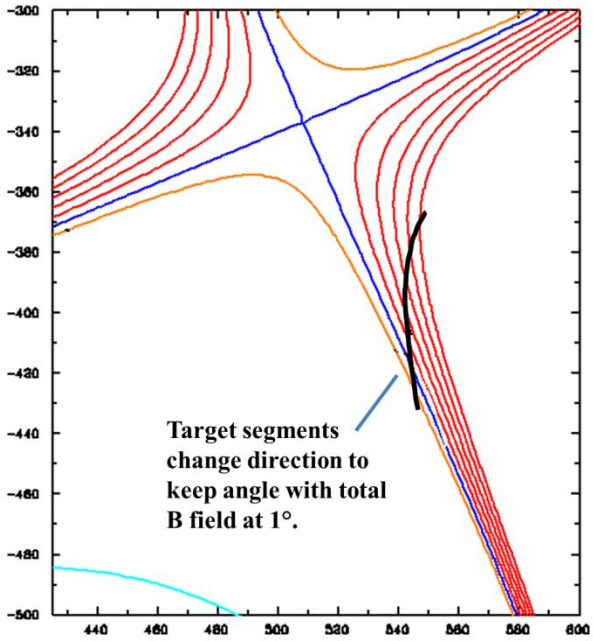

Figure 39: For future tokamaks with flexibility in their target designs, a script can be used to generate a target that maintains a specified angle with the incident field everywhere.

The resolution of the quadrilateral B2.5 mesh is specified radially by choosing flux surfaces in the SOL that will serve as the parallel-field sides of the mesh cells. To specify poloidal resolution, points along the separatrix are chosen, where the cross-field sides of the cells will be cut. Both surfaces and grid points are shown in Fig. 40. In this way, the cells are made to be orthogonal, and transport along and across the field lines is

easily distinguished. However, because the mesh must also conform to the targets at its ends, at some point, the cells must break orthogonality. The *tgarde* variable controls the distance in centimeters away from an impending target at which it is permissible to break orthogonality, as can be seen in Fig. 41. Obviously, a value of 0 is ideal for a perpendicular target, so one tries to find mesh solutions that minimize *tgarde*.

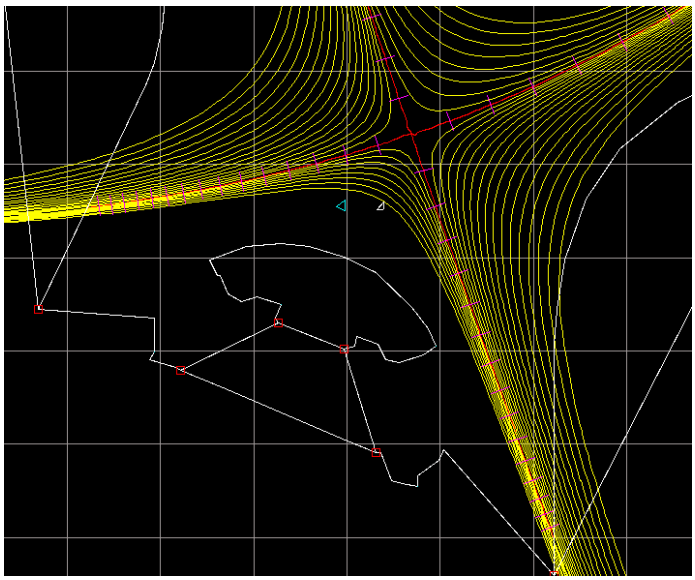

Figure 40: Flux surfaces in DivGeo (in yellow) specify the radial resolution of the B2.5 mesh. Grid points along the separatrix (in pink) specify resolution along the flux surfaces.

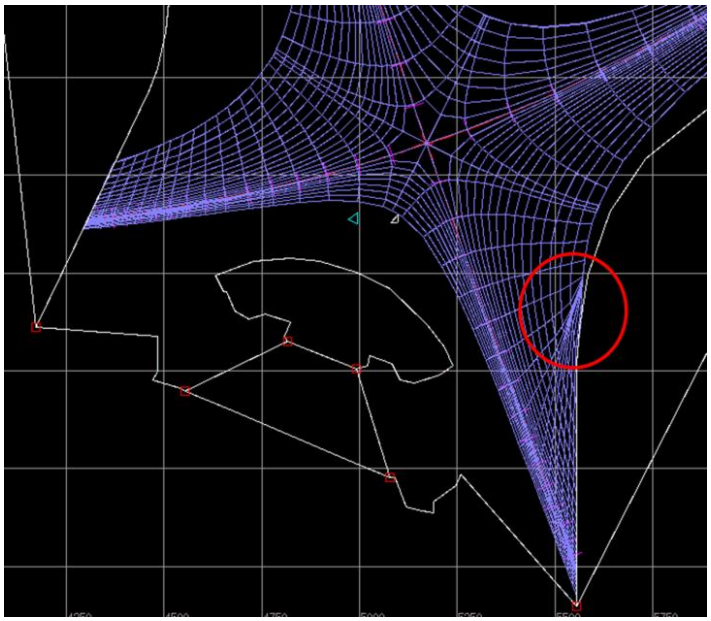

Figure 41: The resultant mesh from the flux surfaces and grid points specified in Fig. 40. The value of *tgarde* specified the length away from the target in which the mesh is allowed to break orthogonality to conform with the target. The effect of this break is visible in the red circle. Clustering of the mesh cells can be avoided with larger values of *tgarde*, but then parallel and cross-field transport are not as easily distinguished.

In an ideal world, every mesh would have very high resolution in all parts of the spatial domain, but as one would expect, this can greatly increase computer run times. Our goal then must be to make the mesh fine enough to resolve the physics we're interested in, while minimizing the time it takes to get a result.

The computational domain of the mesh is rectangular, with North, South, East, and West boundaries. The South boundary is comprised of the edge of the private region on the inner leg, the core boundary, and then the edge of the private region on the outer leg. The North boundary is comprised of the entire mesh edge in the SOL. The inner and outer targets form the West and East boundaries, respectively. All of these boundaries are illustrated in Fig. 42. In the case of double-nulls, there is a break in the mesh to allow for

two extra targets, so the North and South boundaries are broken into twice as many sections (Fig. 43).

To enforce boundary conditions, small, special boundary cells are generated everywhere along the boundary. The choice of where to draw the mesh boundaries is a critical issue. SOLPS is not equipped to model features deep in the core region, such as the pedestal, so where to choose the flux surface that will be the edge of the core boundary is ambiguous. Usually, the core boundary is not specified within the 95% flux surface (ψ_{norm} = 0.95). The same conundrum applies to the SOL and private region boundaries: one wants to make sure that the radial extent of the mesh is sufficient to encompass all of the plasma, but adding cells increases computation time. The extent of the mesh we choose varies with the idiosyncrasies of each tokamak.

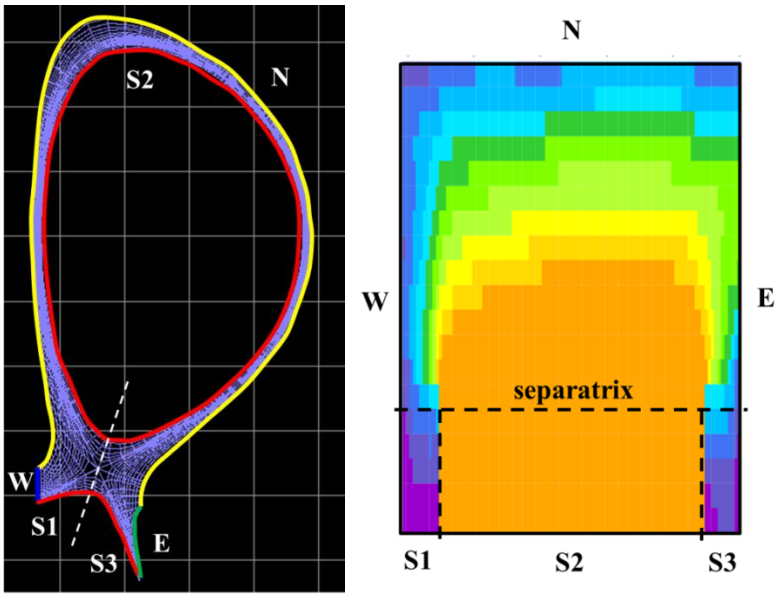

Figure 42: The single-null B2.5 mesh in the physical domain (left) is mapped to a rectangular grid in the computational domain (right). Boundary conditions are enforced along North, South, East, and West boundaries. A break exists in the private region, so the mesh cells there are discontinuous in the physical domain.

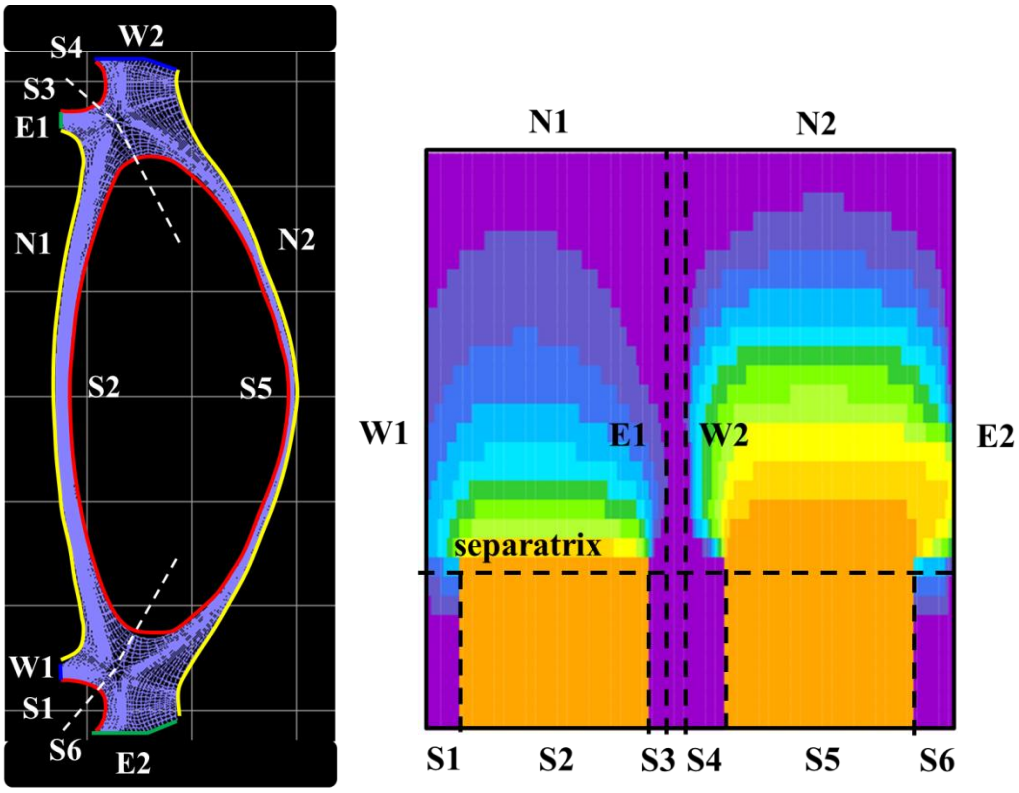

Figure 43: The double-null mesh has an additional break to account for the extra boundary conditions needed at the upper targets. The boundary mesh cells at the E1 target neighbor the boundary cells at the W2 target in the computational domain.

There is only one hard restriction on the specification of mesh cell resolution. Because the mesh must be contiguous in the computational domain, and the South boundary contains both the private region and core boundaries, both the private region and the core must have the same number of radial flux surfaces specified, even though they are separate regions in the physical domain. The same restriction exists between the inner and outer SOLs in a double-null.

Otherwise, problems in DG usually stem from the program misinterpreting the equilibrium, either from insufficient resolution in $\psi(R,z)$, or from topology confusion

caused by multiple x-points. As DG and Carre were originally developed only for standard divertors, they only expect to identify three regions in single-nulls (core, SOL, private region) or five regions in double-nulls (core, 2 SOLs, 2 private regions), differentiated by the separatrix. The presence of additional x-points can, however, cause the appearance of flux surfaces in the private region which have the same ψ values as those in the SOL. While this entire region is, of course, the private region, the programs' interpretation of the regions is based purely on the magnetic data, and these areas can be incorrectly interpreted as the SOL. Hence, careful equilibrium cropping may be needed to remove these problematic areas from the view of DG and Carre (Fig. 44).

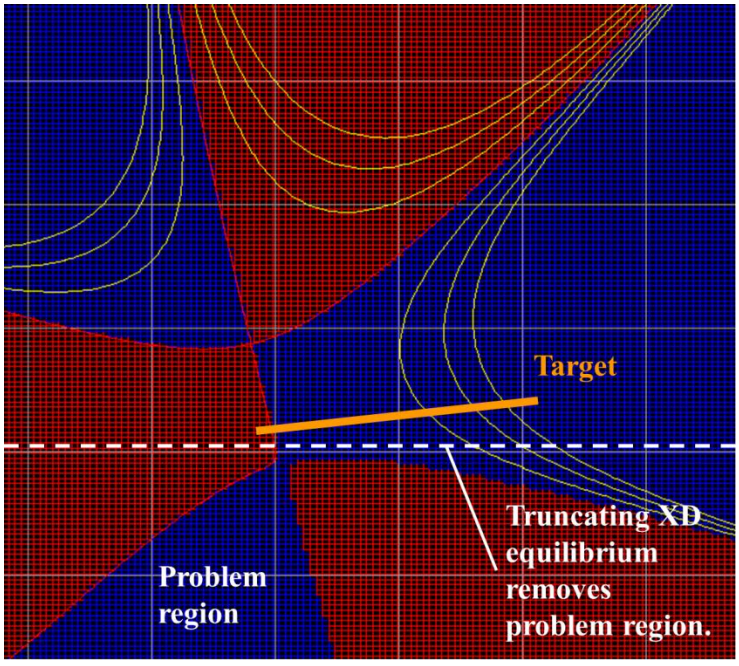

Figure 44: The more complex geometry of the X-Divertor creates a region problematic to DivGeo. To avoid this problem, the problem region must be removed by truncating the equilibrium.

It is for this reason that Snowflakes are often difficult or even impossible to model in SOLPS. Because the available cropping tools are only able to make cuts in the R and z directions, and because the second x-point is often located in the private region very near the main x-point, it is often impossible to crop out the entire problem area without also removing necessary parts of the SOL around the targets (Fig. 45). By contrast, XDs and SXDs are fortuitous to have their x-points in the downstream SOL, often behind the target plates, where the equilibrium can be safely cropped.

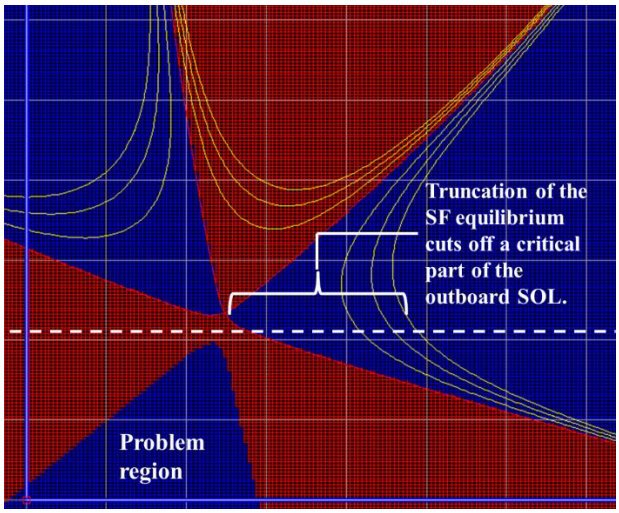

Figure 45: Equilibrium truncation for Snowflakes is more problematic, since the two x-points must be close to each other to fully exploit poloidal flux expansion. A critical part of the SOL gets truncated as well.

Once all of the mesh parameters are specified in DG, output is generated for the Carre mesh generator, which proceeds to run automatically. The output mesh can then be imported back into DG for visual inspection. If there were any convergence problems in Carre, they will be apparent in DG, usually as overlapping cells (Fig. 46). If the mesh is satisfactory, then it is ready to be incorporated into the B2.5 input.

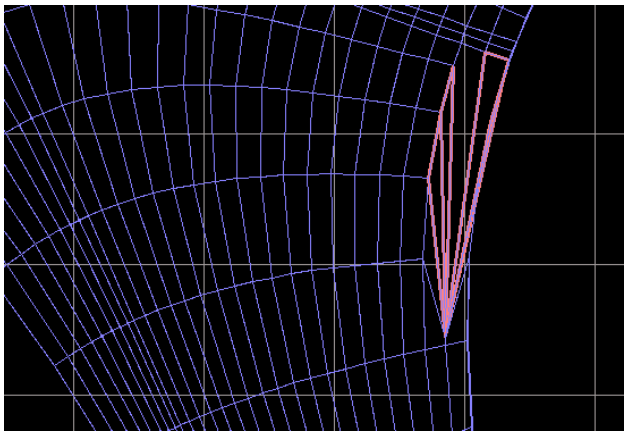

Figure 46: Errors in the mesh generated by Carre are highlighted in pink in DivGeo.

Eirene 2008 uses its own separate, triangular mesh to track neutrals, a feature of SOLPS 5.1. Using the same structure specified in DG, and now the B2.5 mesh, the bounding perimeter for the Eirene mesh is defined. The mesh can be refined to any degree locally with the use of "refinement zones" in DG. With both meshes generated, the entire space inside the vacuum vessel is covered (Fig. 47).

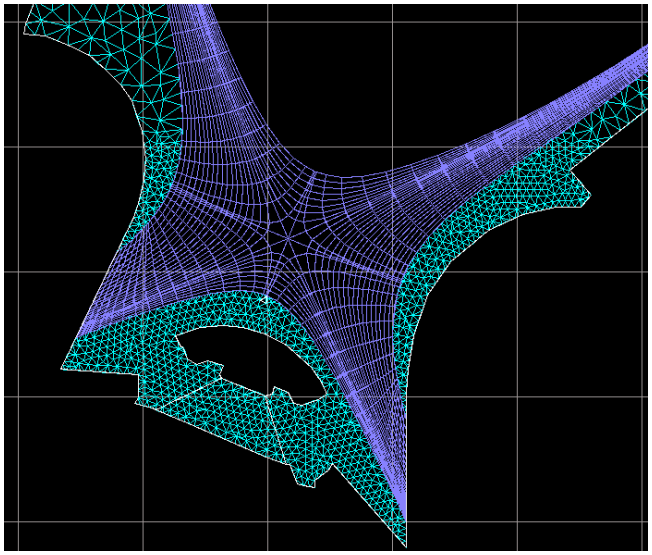

Figure 47: The entire vacuum vessel space is mapped out by a combination of the B2.5 (violet) and Eirene (green) meshes.

6.4. SCRAPE-OFF LAYER MODELING IN B2.5-EIRENE

For transport modeling, the B2.5 and Eirene codes work in tandem as a coupled code.

The B2.5 code models the plasma physics by finding numerical solutions for the classic Braginskii equations on the 2D, discretized mesh provided by Carre. Each ion charge state is modeled as a separate fluid. To evolve the plasma in time, a fully implicit method is used; this is computationally more intensive, but has the benefit of being unconditionally stable for different time steps.

In contrast to the fluid approach of B2.5 for the plasma, Eirene models neutrals stochastically via Monte Carlo methods in a fully 3D environment. Because it tracks individual particle histories to develop the distribution function of the neutrals, it is far more accurate – though more computationally intensive – than the neutral fluid model of B2.5, which only considers a finite number of moments of the distribution function.

B2.5 and Eirene communicate with each other during each time step in a semi-implicit fashion. More specifically, B2.5 serves as a plasma background through which Eirene neutrals travel, while Eirene provides the particle and energy sources for the Braginskii equations in B2.5. Because we are opting to supplant the B2.5 neutral code with Eirene, some features in B2.5 may be overridden by Eirene when running the coupled code.

To prepare the B2.5 input, several files need to be written. First, an initial plasma state is generated. This plasma has uniform density and temperature. Obviously this state is nothing like what we expect the final plasma state to be, so we anticipate the solution to evolve. Consequently, it is beneficial to use any *a priori* information we have about the

tokamak SOL to carefully specify an initial state; the fewer time steps B2-Eirene has to take to find a convergent solution, the less overall computation time is required.

Next, boundary conditions are specified. In the boundary input file, each section of the North, South, East, and West boundaries are delineated by the range of radial/poloidal mesh cells that comprise them. The choice of boundary condition along the core boundary is highly important to the final result, as this condition specifies how much energy and how many particles enter the SOL from the core. For this work, the total power into the SOL is specified, equally distributed between electrons and ions. To reflect experimental observations, for double-nulls, twice the power is exhausted into the outer SOL than into the inner SOL. Boundary conditions are also critical for the East and West boundaries, at the target plates, because B2.5 cannot model the sheath conditions there. Those conditions are approximated by the choice of boundary condition. Conditions at the edge of the SOL and the private region are more ambiguous. One may choose to specify a density SOL width, a particle flux loss, or any other number of conditions. This is what motivates us to increase the radial extent of the mesh in DG; if the plasma is guaranteed not to make it to the edge of the mesh, then we can specify exactly that – i.e., that all profiles go to zero far away from the separatrix.

Next, parameters for neutrals are set. Even though Eirene overrides the B2.5 neutral fluid model, the B2.5 input files still specify select parameters, such as the chemical sputtering yield, and the particle flow rate from gas puffing sources. All of the atomic species, their masses, and their charge states must also be declared in B2.5. These species will be checked to make sure they match with those declared in Eirene.

Coefficients for various transport processes are specified in the transport input file. As previously mentioned, there are currently no models for the heat diffusivity and the density-driven particle diffusivity, X and D. Consequently, for this work, four

different types of cases, each with different transport coefficients, are run simultaneously to develop a parameter space: $X = 1.0$, $X = 0.5$, $X = 0.2$, and $X = 0.1$. Per experimental observation, D is always kept at 30% the value of X. For this work, these values are kept constant everywhere throughout the mesh, though a ballooning option is available to vary the coefficients spatially according to the local magnetic field strength, which may be preferable in some areas and wildly inaccurate in others. Once a convergent solution is found, the resultant power SOL width is measured from the outer midplane. In this way, results for the expected width can be compared to results from the more optimistic and pessimistic width predictions. The viscosity coefficient is also specified here and given a nominal value of 0.2.

Eirene input is prepared in a wholly different file, as Eirene is a wholly separate code. There, all of the structure surface data, plasma background, and atomic and molecular interaction data are specified. For each surface, the particle recycling coefficient, absorption, and even transparency are specified. Links are specified to an extensive list of atomic and molecular physics libraries available as part of the SOLPS download. Relative CPU time is allocated to each source, or stratum, of neutrals, including the target surfaces, the edges of the B2.5 mesh, volumetric recombination, and any gas puffing sources specified.

In truth, the Eirene input file is quite extensive, unintuitive, and fickle about formatting. This is because Eirene was written to handle a myriad of neutral physics scenarios other than tokamaks, but eventually customized to couple with B2.5. Consequently, the Eirene input file is rarely prepared by hand; nearly all of the aforementioned neutral physics parameters may also be specified using the much more user-friendly DG, then written as output to the UINP utility, which finally generates the input file.

6.5. HIGH-PERFORMANCE COMPUTING

It goes without saying that due to the complexity of the problems at hand and the large meshes involved, the amount of computing time to reach a convergent solution for most tokamaks can be enormous. Consequently, supercomputers capable of high-performance computing are required to yield results in a timely fashion. Even with such resources, the real time to reach a convergent solution can be anywhere from a few days to several months. This doesn't include the human time that goes into advanced divertor design, and the inevitable tweaking of gas puffing sources to hit a target edge density and impurity concentration.

For its part, at least, the TEQ code in the CORSICA suite is not computationally intensive. For developing the advanced divertor magnetic equilibria, a Dell desktop computer with an Intel i7 quad-core processor was used. Typical TEQ run times for each change made to the input parameters (e.g., manually controlled PF coil currents) are only about 5-30 seconds. However, many hundreds of input changes may occur in the process of designing the divertor, extending the CORSICA phase of the modeling effort to several days or weeks.

Naturally, B2.5-Eirene is the biggest time sink, specifically Eirene. For these jobs, the Lonestar supercomputer at the Texas Advanced Computing Center (TACC) was used. Lonestar harbors 22,656 cores, most of which are housed on 12-core Dell PowerEdge M610 nodes. Each set of 12 cores is contained in two Xeon 5680 Series 3.33GHz hex-core processors. Each node offers 24 GB of RAM and 12 MB of L3 cache memory. Jobs are submitted via the SGE batch submission environment, with a maximum of 24 hours of runtime for a single job [18].

Typically, the real advantage of supercomputers is that the subroutines of a single job can be divided amongst several cores, a process known as parallel computing. Unfortunately, at this time, the B2.5-Eirene is not highly parallelizable, so each problem can only be assigned to a single core – this is known as serial computing. The advantage of Lonestar, therefore, is not to reduce computing time for a single job, but to be able to run several dozen jobs simultaneously using many cores. In this way, a large volume of results can be collected at once, if not faster. To do this, the pylauncher utility is used to "wrap" 12 serial jobs and submit them collectively to a single node.

Chapter 7:

Lessons of Advanced Divertor Design

The rest of this work details the application of the CORSICA and SOLPS codes to an array of tokamaks of interest, where the use of XDs and SXDs is very promising. Early results from the models are discussed in turn, though much work remains to be done.

Before individual tokamak designs are considered, however, it is perhaps even more important to enumerate the general principles of advanced divertor design, principles which are based entirely on experience with TEQ, and which would make for a most challenging optimization problem. We already know well what constitutes an XD, SXD, or Snowflake, but how does one control x-point position? Elongation? Triangularity? It is this hard-learned intuition that will be described here in subjective terms.

One is tempted from the 2D simplification that the Grad-Shafranov equation offers to view PF current sources as current filaments in the poloidal plane. This is most certainly *not* the case; the off-axis magnetic fields of toroidal current loops are considerably more complicated. However, as a means of developing a basic intuition for magnetic field manipulation, viewing PF currents as filaments suffices. We begin by examining a single PF current filament. The field generated by this filament is circular, whose strength decreases inversely with distance. If we single out a field line, beyond which we consider the field to be too weak to be influential, then we can view the current filament as having created a "lobe," or an area of influence, about it. If the strength of the

current increases, then the field line of the same strength which we'd previously singled out is found at a larger radius. Hence, the size of our lobe increases.

When two parallel PF current sources are placed sufficiently within each other's influence, their respective lobes link together. That is, at a distance roughly of the order of the distance between the current sources, there are now field lines which encompass both lobes. As one would expect, at large distances, the two parallel currents have a similar effect to one filament with the sum of their currents. Of course, at shorter distances, along the path between sources, the respective fields work against each other. At some point, an x-point is formed inside the compound lobe, as we've seen before in Fig. 2. Like a reversed center-of-mass argument, the location of the x-point depends on the relative strength of the currents, moving away from the stronger current. This makes sense; the stronger current has a greater influence at larger distances, and thus zeroes the field closer to the weaker current.

By contrast, the lobes of antiparallel currents will tend to repel each other, resisting the creation of mutually encompassing field lines. The effect of two antiparallel currents in close proximity depends on their relative magnitude. Obviously, if both currents are equal in magnitude, then the field at great distances away is negligible, while the field between them is reinforced. However, if there is a sufficient disparity in the current strengths, then lobes of antiparallel currents can exist inside each other (Fig. 48).

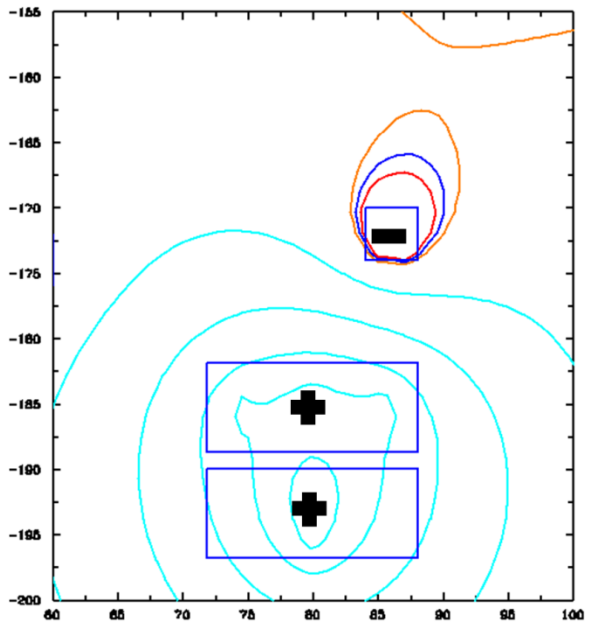

Figure 48: A coil with a negative (antiparallel) current can create a lobe within the lobe of a positive current source.

Based on these simple principles of lobes, one can now make sense of several tokamak magnetic field structures, often even being able to deduce the current distributions that likely created them. We may consider the plasma itself to act as a simple PF current source, though the real toroidal current is distributed throughout the plasma and can be quite complicated. Naturally, the lobe of interest for the plasma is bounded by the separatrix, the border between the core and the SOL. For simplicity, we will define the direction of the toroidal plasma current, and any other parallel PF current, as being in the positive direction.

The creation of the plasma's main x-point then becomes elementary; simply introduce a positive PF current of sufficient strength to link lobes with the plasma, such that the x-point created along the path between the two currents is in the desired location. This location determines the elongation of the plasma. As we just discussed, the location

of the x-point between two positive currents depends on the currents' relative strength. It should come as no surprise then that when the plasma current is increased, the main x-point tends to move away from the plasma center, and the elongation increases. To reduce the elongation again – i.e., to push the main x-point more toward the plasma – the PF current will have to increase proportionally. This is something we observe for all magnetic geometries: if the plasma current increases, then the total current in the PF coils which play a significant role in shaping the plasma must increase proportionally, in order to maintain the plasma shape.

What about triangularity? Triangularity is essentially the control of the major radius of the x-point. Based on our previous arguments, one can then quickly envision two ways to increase triangularity: (a) introduce an inboard, positive PF current to attract the plasma current lobe toward the inboard side, or (b) introduce an outboard, negative PF current to push the plasma current lobe toward the inboard side. Depending on the limits on the coil conductors, both approaches may need to be applied in tandem to achieve high triangularity (Fig. 49). Furthermore, for these PF currents to be maximally influential on the main x-point, their distance from the main x-point should be minimized, meaning that the PF currents should be at roughly the same z as the main x-point.

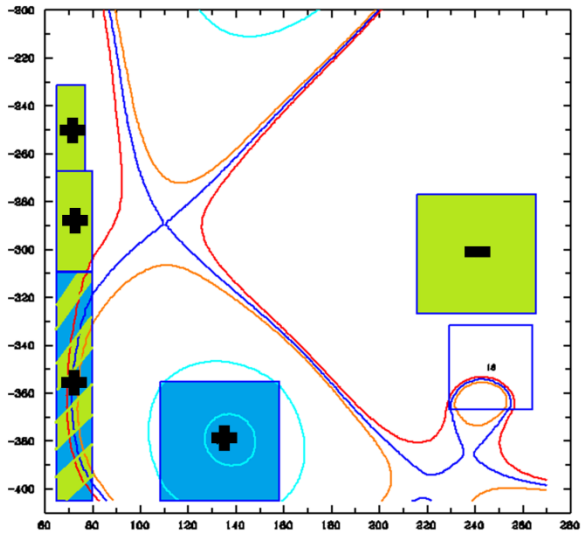

Figure 49: PF coils are color-coded to show their strong influences on the main x-point. Green coils strongly influence triangularity, such as the inboard coils with positive currents, or the outboard coil with a negative current. Blue coils strongly influence elongation, such as the positive coil that creates the main x-point. Some coils serve dual purposes.

These principles apply not only to the main x-point, but also to the additional x-points we introduce to create advanced divertors, such as in Fig. 50. It's easy enough to create a new x-point along the line between two positive currents, but we may also use a negative current to push that x-point off the line to another location. One of our goals in XD and SXD design then is to use the PF currents available to us to place x-points precisely where we want them – namely, near the point of peak heat flux at the target plates, so that flux expansion and flaring of the SOL are maximal. Naturally, the more closely we can place coils to the divertor targets, the more effectively we can influence the field there; barring that, we will require larger coil currents acting at greater distances.

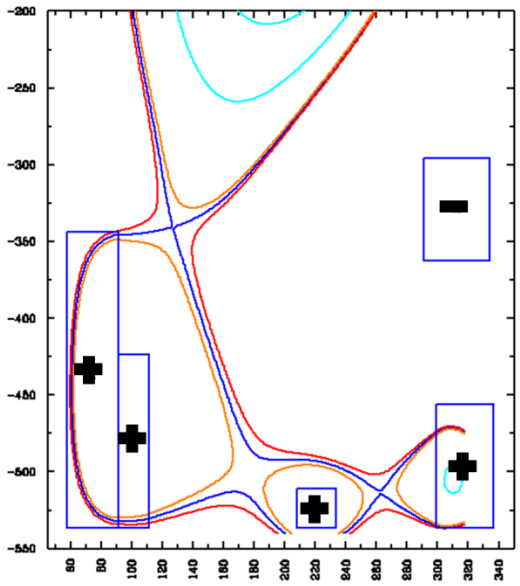

Figure 50: By chaining together the lobes of successive, positive coils and creating multiple new x-points, it's easy to control the path of the divertor leg and create flux expansion, as in this basic Super X-Divertor.

The other, no-less-important goal of advanced divertor design is to have minimal impact on the core plasma. We seek to make lobes that create additional x-points, but if we are not careful, these lobes are just as likely to pull on the plasma as they are to benefit the SOL. This can easily lead to undesirably high elongations or reduced triangularities. The ideal divertor scheme de-couples the roles of divertor and plasma shaping as much as possible, keeping the affected region of the SOL close to the targets and far from the plasma, and keeping dual purposing of the shaping coils to a minimum. The closer the main and secondary x-points, the higher the PF currents will be to keep the plasma separated from the divertor region. Conversely, the standard divertor, with no secondary x-point, will always require the minimal PF current in a flexible PF coil system. This qualitative assertion is given quantitative credibility by the efforts of Lackner and Zohm, whose models of a "pure" Snowflake Divertor (i.e., where the main and secondary x-points are coincident) for ITER required exorbitant PF coil currents to

maintain the plasma shape characteristics [19]. Thus, the allowable proximity of the main and secondary x-points will always be dictated by the current limits in the PF coils.

One important point in the discussion that's been tacitly put aside until now is the distinction between inboard and outboard divertor legs. Until now, our treatment of the heat flux at a target by introducing more x-points has focused on a single divertor leg. But if we, say, flare the outboard SOL without doing the same to the inboard SOL, have we really accomplished anything? After all, it only takes one problematic divertor leg to constitute a heat flux problem. Is it possible to create separate x-points for each leg simultaneously, creating a so-called "dual" X-Divertor? These are not easy questions, and while secondary x-points have been created on both inboard and outboard legs simultaneously, their close proximity often requires high PF currents. Thus, dual x-points may only be routinely suited for Super X-Divertors, where the inboard and outboard targets enjoy a farther radial separation. However, an exceptional result may be found in the X-Divertor for Alcator C-Mod, in Sect. 9.2.

For cases where dual XDs are not feasible, the inboard divertor may still turn out to be unproblematic. As has been mentioned, the power balance in most tokamaks has been observed to be asymmetric, sending more power to the outboard SOL by a factor of 2:1 or even 3:1. This is true even for single-nulls, where the inboard and outboard legs are topologically connected. Thus, for most cases, we assume we have the luxury of focusing only on the outboard divertor leg for our advanced divertor designs. Furthermore, it is often such that a secondary x-point in the outboard leg still lends benefits of flux expansion to the inboard leg. Hopefully, these two facts are sufficient to mitigate inboard heat fluxes.

Armed with the principles of magnetic lobes, advanced divertor design almost seems simplistic; we know how to create x-points, and how to influence the plasma, so what's the difficulty? Simply put, we can rarely place PF currents where we want them, or with the strength we'd desire. Coil current limits, limited vacuum vessel space, and radiation shielding are just a few of the many practical constraints that may sharply restrict the use of PF coils to expand the SOL flux tube, making every tokamak a unique optimization and design problem. It will thus be attempted to develop several X-Divertors or Super X-Divertors with maximal flux expansion and flaring, always respecting the constraints of the given tokamak throughout the modeling process in CORSICA and B2.5-Eirene.

IV. ADVANCED DIVERTOR DESIGNS FOR TOKAMAKS

Volume IV presents a diverse range of tokamaks for which X-Divertors or Super X-Divertors have been designed. Preliminary heat flux and plasma temperature results from SOLPS 5.1 are given. Chapter 9 discusses NSTX-Upgrade, Chapter 10 discusses Alcator C-Mod, Chapter 11 discusses a Compact Fusion Neutron Source or Fusion Nuclear Science Facility, and Chapter 12 discusses ITER.

Chapter 8:

NSTX Upgrade

8.1. The NSTX-U Tokamak

The first tokamak considered for advanced divertor design is the planned upgrade to the National Spherical Torus Experiment (NSTX), dubbed NSTX-U, at the Princeton Plasma Physics Laboratory. Following the very successful run of NSTX (Fig. 51) as the premiere low-aspect ratio tokamak in the United States, several major overhauls are currently underway so that NSTX-U may serve as a precursor to a Fusion Nuclear Science Facility (FNSF). Significant changes include a doubling of the plasma current, toroidal field, and neutral beam heating power, as well as increasing the plasma pulse length from 1-1.5 seconds to 5-8 seconds [20].

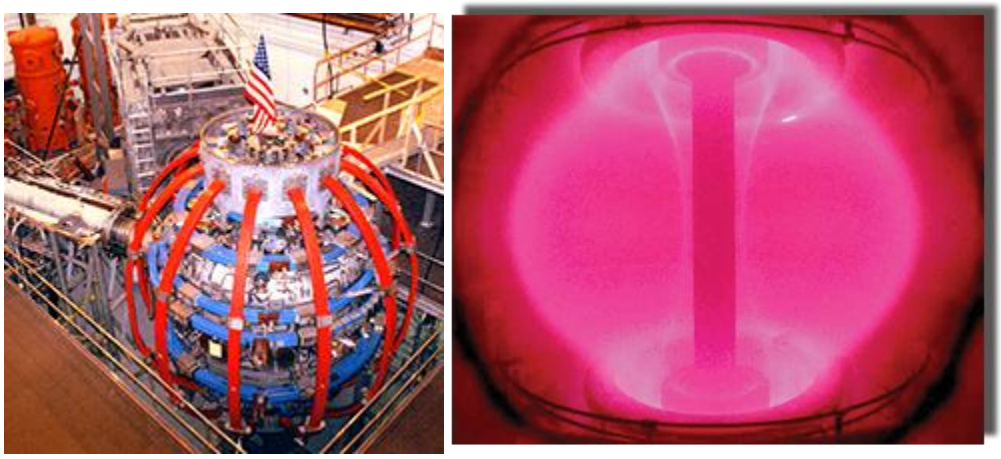

Figure 51: The NSTX spherical tokamak at the Princeton Plasma Physics Laboratory is planned for a major upgrade, NSTX-U. Pictures courtesy of PPPL [21].

As previously discussed, advanced divertors are particularly important for spherical tokamaks; due to their compact nature, there is even less area available at the targets for heat flux dispersal than in a standard tokamak. The NSTX-U design has already been finalized, so any advanced divertor we design must utilize only the planned PF coils, with currents within their respective limits.

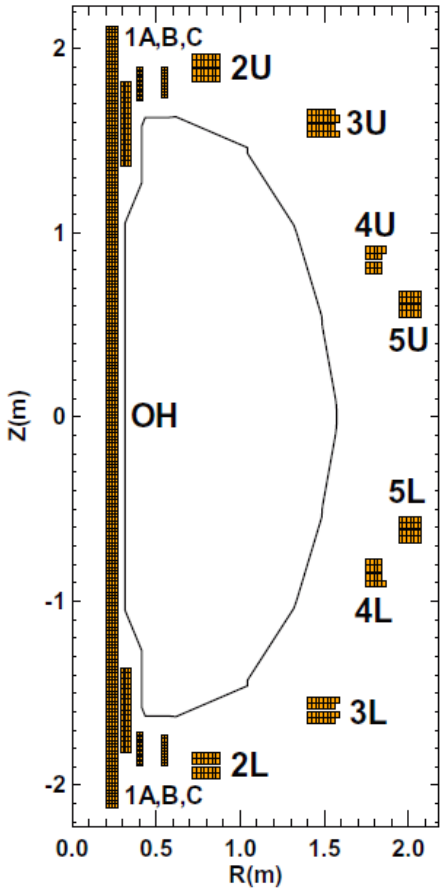

Figure 52: The planned PF coil set and solenoid for NSTX-U [22].

From Fig. 52, one can see that the PF coils consist of smaller stacks of conductors, which are all in series with respect to each other, so they must carry the same current per turn. Furthermore, the PF4 and PF5 stacks on the top of the machine are also

in series with their counterparts on the bottom, requiring that they carry the same current at all times. The scenario plasma we seek to model is fully non-inductive, so we are restricted from using the center solenoid to shape the divertor.

Fortunately, in NSTX-U, the outer divertor plate is extensive, so strike point control is not as critical as in other tokamaks, giving us more leeway in our search for flaring magnetic geometries. NSTX-U also benefits from having its PF1 and PF2 coil sets unusually close to the targets, which will allow us to expand the SOL flux tube with relatively small changes in current.

NSTX-U will be capable of running both single-nulls and double-nulls; for this work, we have chosen to focus on a symmetric double-null. While there are many operational scenarios envisioned for NSTX-U, the most extreme for the divertor predict as much as 19 MW entering the SOL, and the power SOL width to be as low as 1-3 mm [20]. Naturally, we choose to test the mettle of advanced divertors in this scenario. For atomic species, we include deuterium for the plasma, carbon for sputtering, and neon for injected impurities.

8.2. AN X-DIVERTOR FOR NSTX-U

Figs. 53 and 54 show the TEQ free-boundary equilibrium of an X-Divertor developed for NSTX-U, using only planned PF coils and respecting coil current limits.

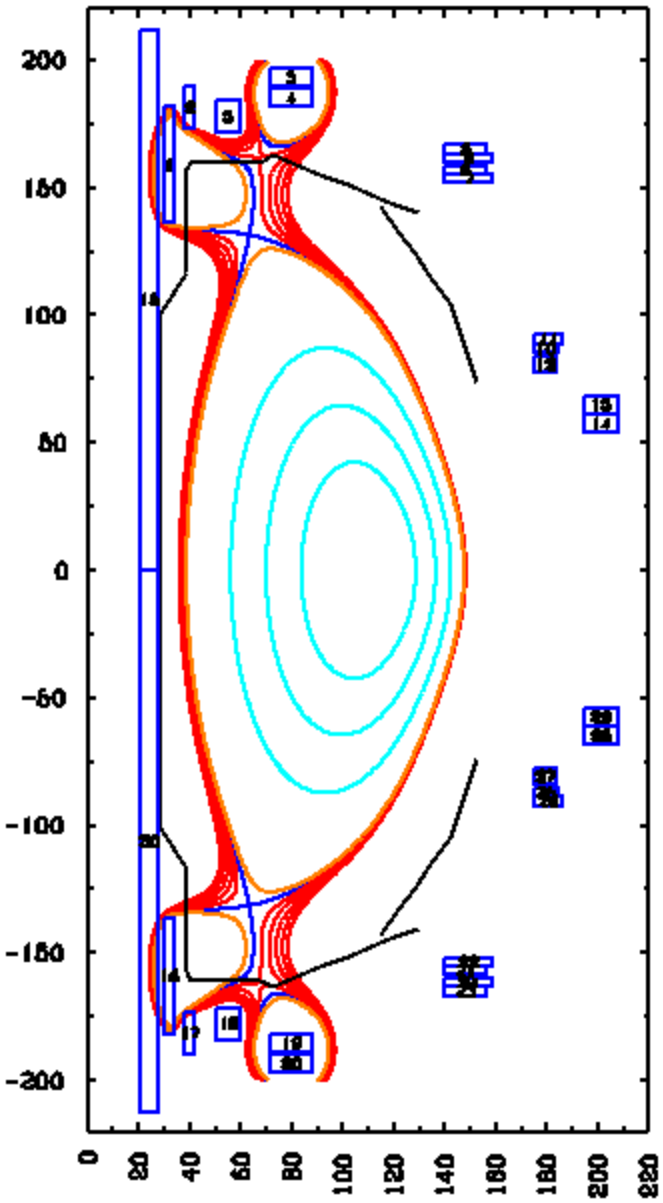

Figure 53: An X-Divertor for NSTX-U, respecting coil current restrictions. For this case, a double-null was modeled. Terrific flux expansion and flaring are accomplished at the outboard targets.

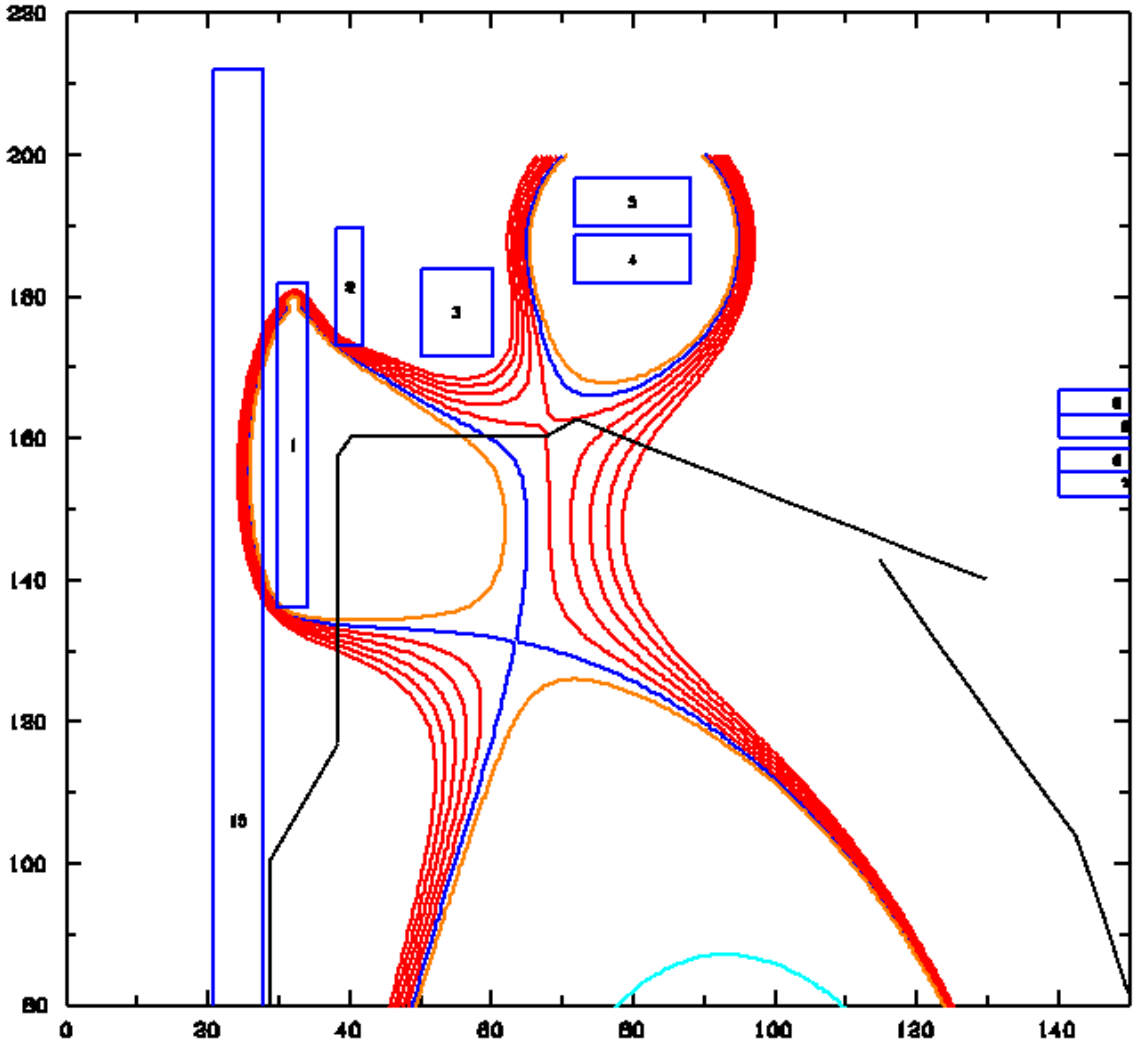

Figure 54: A close-up of the upper X-Divertor on NSTX-U. Each successive flux surface (in red) on the inner and outer SOL represents a 1-mm increment of the outboard SOL width.

NSTX-U XD Plasma Attributes	
R_o (m)	0.93
a (m)	0.55
I_p (MA)	2.00
B_T @ R_o (T)	1.01
κ	2.39
δ	0.48
β_T	24.5%
P_{SOL} (MW)	19
Outer flux exp.	63.4
Outer DI	14.23
Outer conn. length (m)	17.5

Table 1: Parameters for the NSTX-U core plasma, and flux expansion and Divertor Index for the outboard X-Divertor.

Following our principles of advanced divertor design, we have used the coil PF1A and the PF3 stack to control the main x-point and thus plasma elongation and triangularity. The positive lobe generated by PF1A is coupled with the lobe of the plasma current, forming the main x-point. With PF2, a third positive lobe has been made to form a secondary x-point with the PF1A lobe, creating a remarkably strong X-Divertor. PF1C uses a negative current to push this x-point extremely close to the target plate (represented along with the first wall by the solid, black lines), maximizing flux expansion and flaring at the strike point.

The SOL flux surfaces shown in red in Fig. 54 represent incremental outboard SOL widths from 1 mm to 5 mm, with the separatrix highlighted in blue. Because we chose to optimize the X-Divertor for the most pessimistic SOL width, the secondary x-point resides almost right on the 1-mm surface, so that flux expansion is maximal near the peak heat flux. The effectiveness of this choice is evident by the divergence of the flux surfaces and highly visible flaring of the flux tube near the target plate, the hallmark

of a strong XD. Values for *DI* and flux expansion are given for the outboard divertor leg in Table 1. The outboard flux expansion is a whopping 63.4, and *DI* is over 14. True to form from our previous discussion, though there was no attempt to create an x-point at the inboard target, it nevertheless sees some flux expansion as well. *DI* at the inner leg, however, actually falls below 1. This is indicative of a rapidly converging flux tube, and that much is evident in Fig. 54. This will be of some concern to us as we try to bring on a detached state in the outboard leg in B2.5-Eirene; if the inboard leg detaches as well, the inboard detachment front may migrate back to the main x-point and cause loss of energy confinement in the core.

8.3. HEAT FLUX HANDLING AND DETACHMENT IN NSTX-U

Fig. 55 shows how the NSTX-U XD has been discretized by the B2.5 and Eirene meshes.

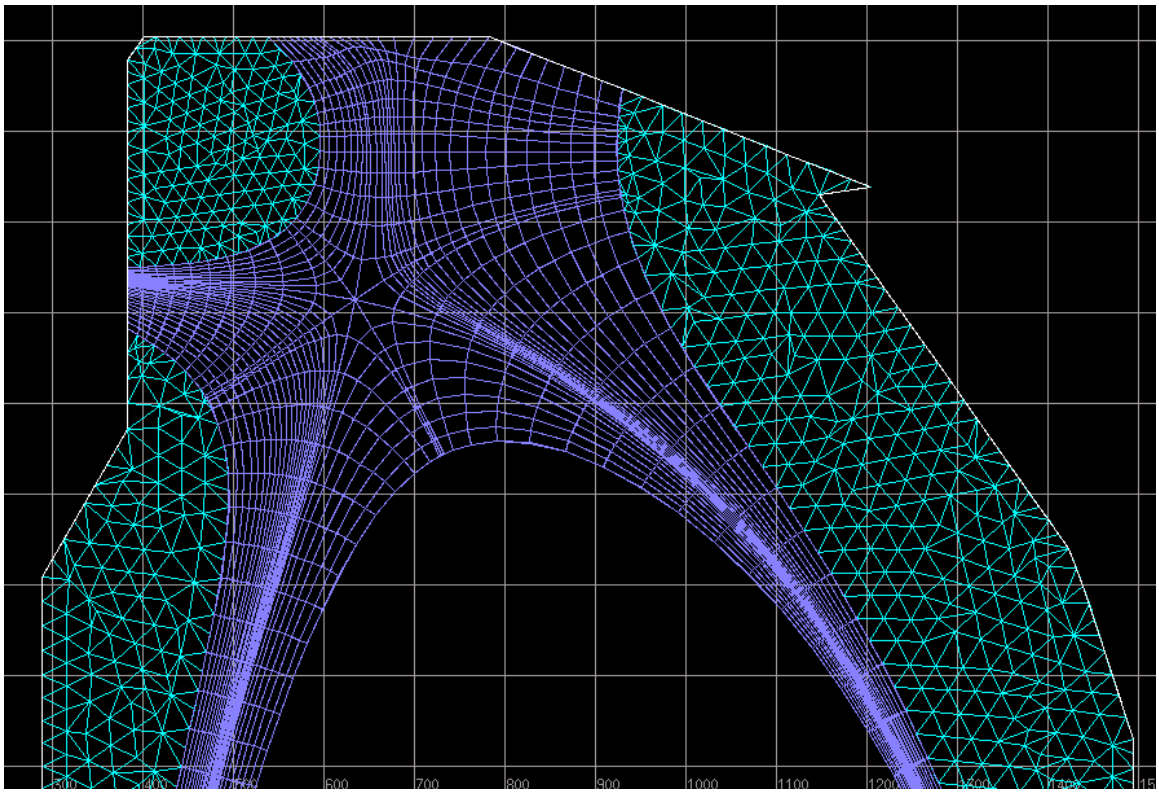

Figure 55: The B2.5 and Eirene meshes for NSTX-U in DivGeo.

Using this mesh in B2.5-Eirene, a range of X (and D, always equal to $0.3X$) was chosen to model cross-field particle and energy transport, not knowing ahead of time which values will yield the desired power SOL width near 1 mm at the outboard midplane. Furthermore, a range of deuterium and neon gas puffing rates were employed to generate a spectrum of plasma edge densities, as well as to encourage detachment. To respect the integrity of the H-mode, edge densities were attempted to be kept in the range of 0.25-0.4 of the Greenwald density limit, and Z_{eff} was kept below 2.0 in the core.

As it turned out, X = 1.0 resulted in a width of almost exactly 1.0 mm, while the lowest D_2 gas puffing rate yielded an edge density of about $0.2n_G$, leaving plenty of leeway for the peak density in the core to stay below the Greenwald limit. Z_{eff} in the core

peaks at about 1.65. Under these conditions, the X-Divertor plasma temperatures are shown in Fig. 56:

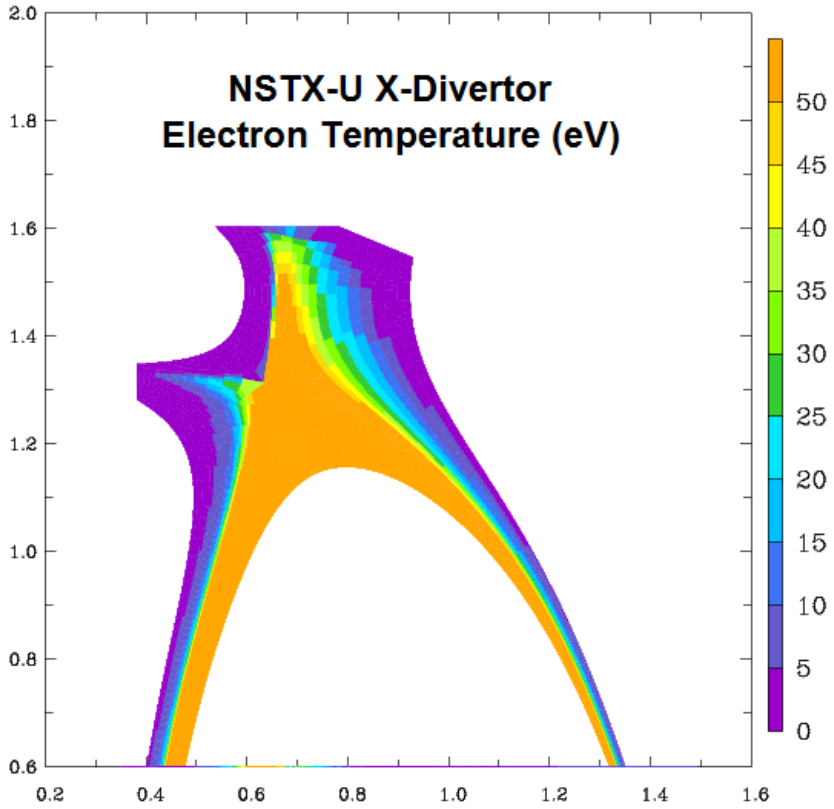

Figure 56: A color plot of the electron temperature in the upper half of the NSTX-U X-Divertor. The outboard leg is still attached, and temperatures are low at the outboard targets. The inboard leg may be excessively cooled by gas puffing, and may be fully detached. Further puffing may detach the inboard leg entirely and cool the core plasma, as *DI* is less than 1 here.

From the temperature plot, one may deduce that the outboard SOL plasma is still attached. That is, while the temperatures along most of the plate have dropped to small values, there is still a small, peaked temperature profile near the separatrix, where the plasma remains attached to the target (Fig. 57). This reduction in plasma temperature stays very close to the target over a steep parallel gradient, which we can see in the

parallel temperature profile in Fig. 58. These observations are consistent with our assertions about the Divertor Index, where divertor legs with $DI > 1$ will be better able to localize plasma cooling effects, and keep them near the target.

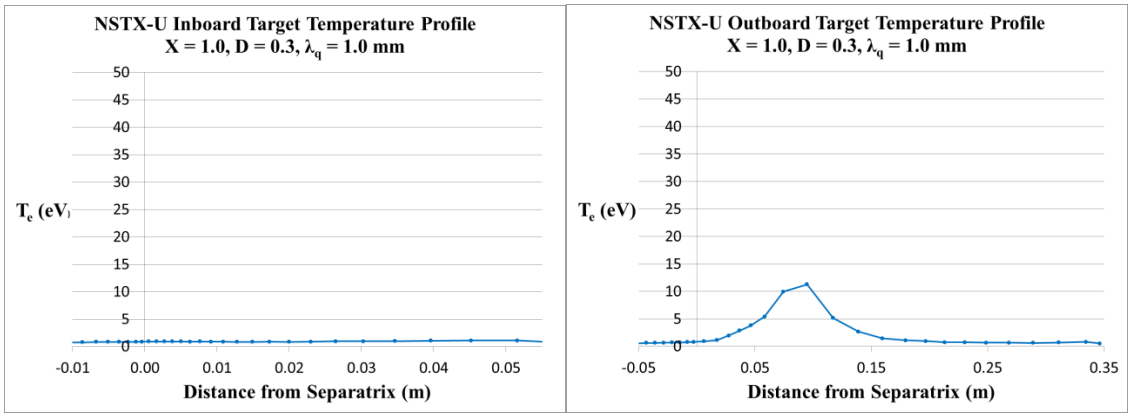

Figure 57: Temperature profiles at the inboard (left) and outboard (right) targets indicate that the inboard leg has fully detached, but the outboard leg has not, though temperatures are manageable.

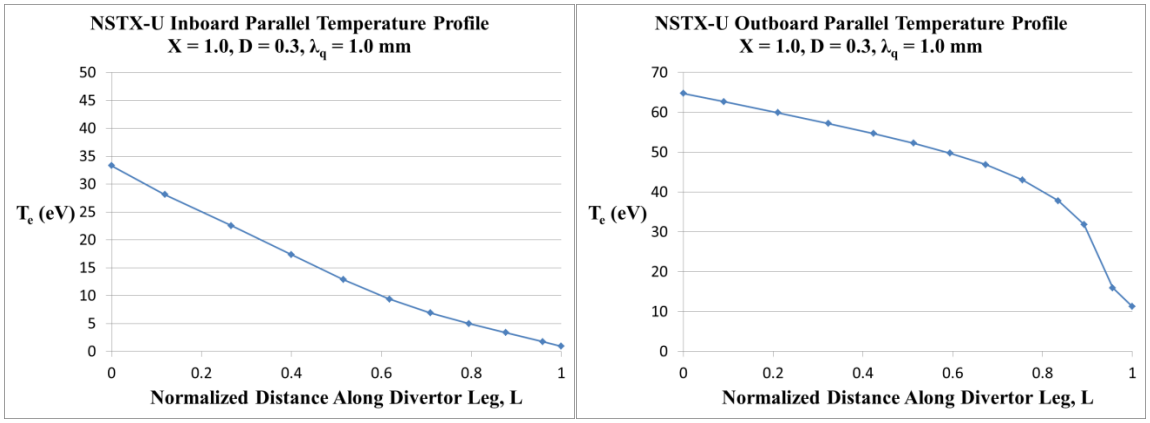

Figure 58: The parallel temperature profile of the inboard divertor (left), where $DI < 1$, is very gradual, indicating unrestricted cooling of the entire divertor leg. Meanwhile, the parallel temperature profile of the outboard divertor (right), where $DI > 1$, shows a noticeable gradient near the target, indicating more localized cooling.

One may also deduce from Figs. 57 and 58 that our fears about the onset of detachment at the inboard leg were also justified; there, the parallel temperature gradient declines gradually all the way back to the main x-point. Further gas puffing may result in a loss of core energy confinement. This observation is also consistent with our assertion of the role of the Divertor Index, where divertor legs with $DI < 1$ will be especially prone to upstream detachment front migration.

Nevertheless, flux expansion alone may be sufficient to mitigate the heat flux problem in NSTX-U, as the terrific flux expansion brought on by the X-Divertor successfully keeps the peak heat fluxes at the targets low, even against the pessimistic SOL conditions we've set forth (Fig. 59). It will be of future interest to explore higher gas puffing rates in order to observe the XD geometry in full detachment.

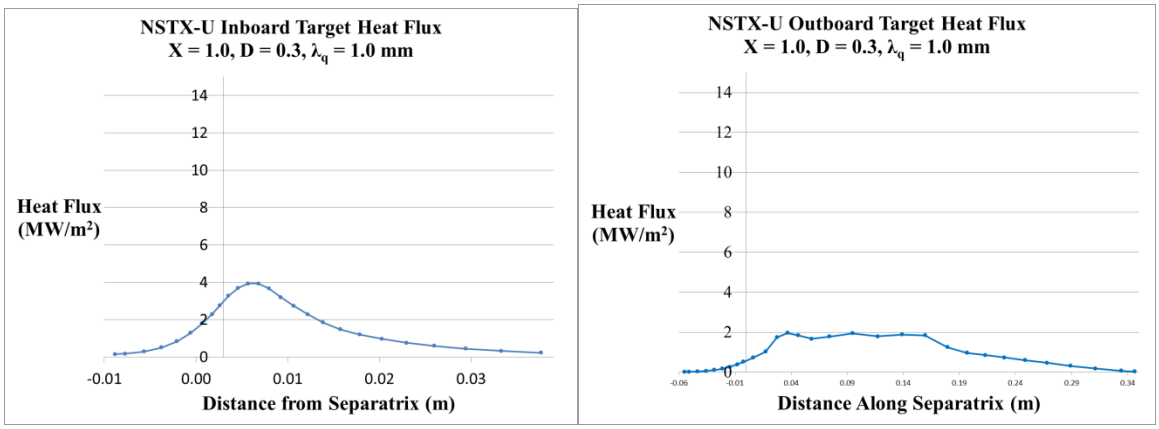

Figure 59: Both inboard (left) and outboard (right) heat flux profiles are well below the standard limit of 10 MW/m^2. Even though the outboard leg receives more of the SOL power and is still attached to the target, it shows greater reduction in heat flux at the target than the inner leg due to its immense flux expansion there.

Chapter 9:

Alcator C-Mod

9.1. The C-Mod Tokamak

Motivated by the promising results of the NSTX-U XD, we try our hand at an XD for a different tokamak, Alcator C-Mod, located at the Massachusetts Institute of Technology. Pictures of C-Mod and its plasma are shown in Fig. 60.

Figure 60: Alcator C-Mod, at the Massachusetts Institute of Technology. Photographs courtesy of *fusionfuture.org* [23].

A more conventional tokamak, C-Mod has recently been repurposed specifically for advanced divertor study. In this, C-Mod is well suited, having one of the most versatile PF coils systems this author has had the opportunity to work with (Fig. 61). That being said, at this stage, it is necessary for the PF coils, targets, and first wall to remain fixed in place, requiring that we work within the existing vacuum vessel space to create an X-Divertor, with the existing coils.

This represents a significantly harder constraint than that which NSTX-U presented us, given that the vacuum vessel space in C-Mod is very tight. The plasma edge may come as close as 1 cm to the first wall, but no closer. The existing targets are naturally optimized for a standard divertor, oriented very obliquely with respect to the SD legs. This is obviously beneficial for decreasing the angle of inclination between the target and the incident field, but it also creates problems for an X-Divertor. Because the target cuts so obliquely across the SOL flux tube, the benefits of flux expansion and flaring are quickly lost if the equilibrium experiences a vertical shift; the strike point quickly shifts along the target and away from the secondary x-point (Fig. 62). Thus, C-Mod requires a very narrow window for strike point control.

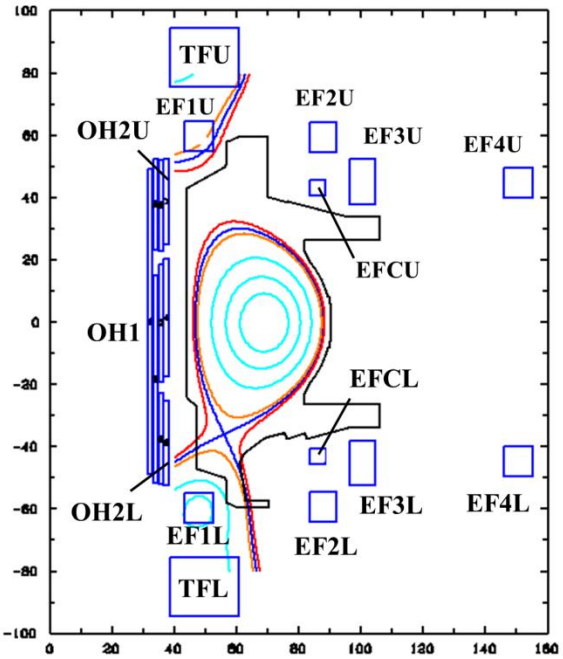

Figure 61: The C-Mod PF coil system is an incredibly versatile coil system. EF3U and EF3L are linked in series. EF4U and EF4L are linked in parallel. EFCU and EFCL are in anti-series, so they must carry equal and opposite currents.

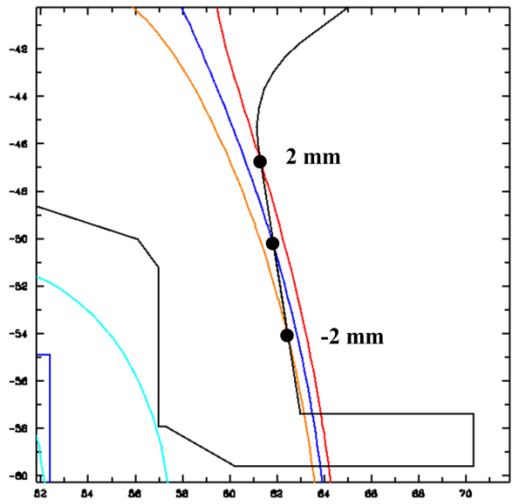

Figure 62: The outboard target of C-Mod is very oblique with respect to the incident field to increase the plasma-wetted area of a standard divertor. Even a range of only ±2 mm from the separatrix at the outboard midplane covers most of the area of the target downstream. This requires for XD design that strike point control is tight, or else the benefits of flux expansion and flaring from the secondary x-point are quickly lost.

The PF coils of C-Mod are highly adaptable; nevertheless, there are constraints on the ways in which they may run currents. The upper and lower EF3 coils are linked in series, so they must run the same current. The upper and lower EF4 coils are linked in parallel; for simplicity, similar resistances are assumed, and they too run the same current. Finally, in an interesting twist, the upper and lower EFC coils are linked in *anti*-series, so their currents must be equivalent and run in opposite directions.

The windings of the center solenoid are particularly unusual, as they are not bound in the usual rectangular casing. Instead, they are more or less free-form, consisting of four bundles on four independently controlled circuits. To simulate this properly, each of these bundles is represented in CORSICA by several rectangular coils whose relative currents must always be proportional to their respective number of turns.

One last quirk particular to C-Mod is a modest contribution of the TF coil to the PF current distribution. It is not unusual for a tokamak's TF coils to be coupled to the center solenoid at regular joints around the torus. For C-Mod, these joints have projections in both the poloidal and toroidal directions, meaning that a component of the TF current running through them will act as an effective PF current at their location, running in the same direction as the plasma current. Because this is a TF current, its component is fixed for fixed B_T, and it is represented in CORSICA by positive PF coils labeled 'TFU' and 'TFL' at the top and the bottom of the machine (Fig. 61).

The C-Mod plasma is a single-null, so there are only two divertor targets to consider. For this work, the plasma current is run at 0.45 MA, which is about half its usual value. This was done to match attributes with a pre-existing Snowflake Divertor designed by Stephen Wolfe at MIT. Consequently, if the plasma current were to be increased, one can expect PF coil currents to increase. The typical outboard power SOL width is about 1 mm [24].

9.2. AN X-DIVERTOR FOR C-MOD

Figs. 63 and 64 show the TEQ free-boundary equilibrium of an X-Divertor developed for C-Mod, using only planned PF coils and respecting coil current limits.

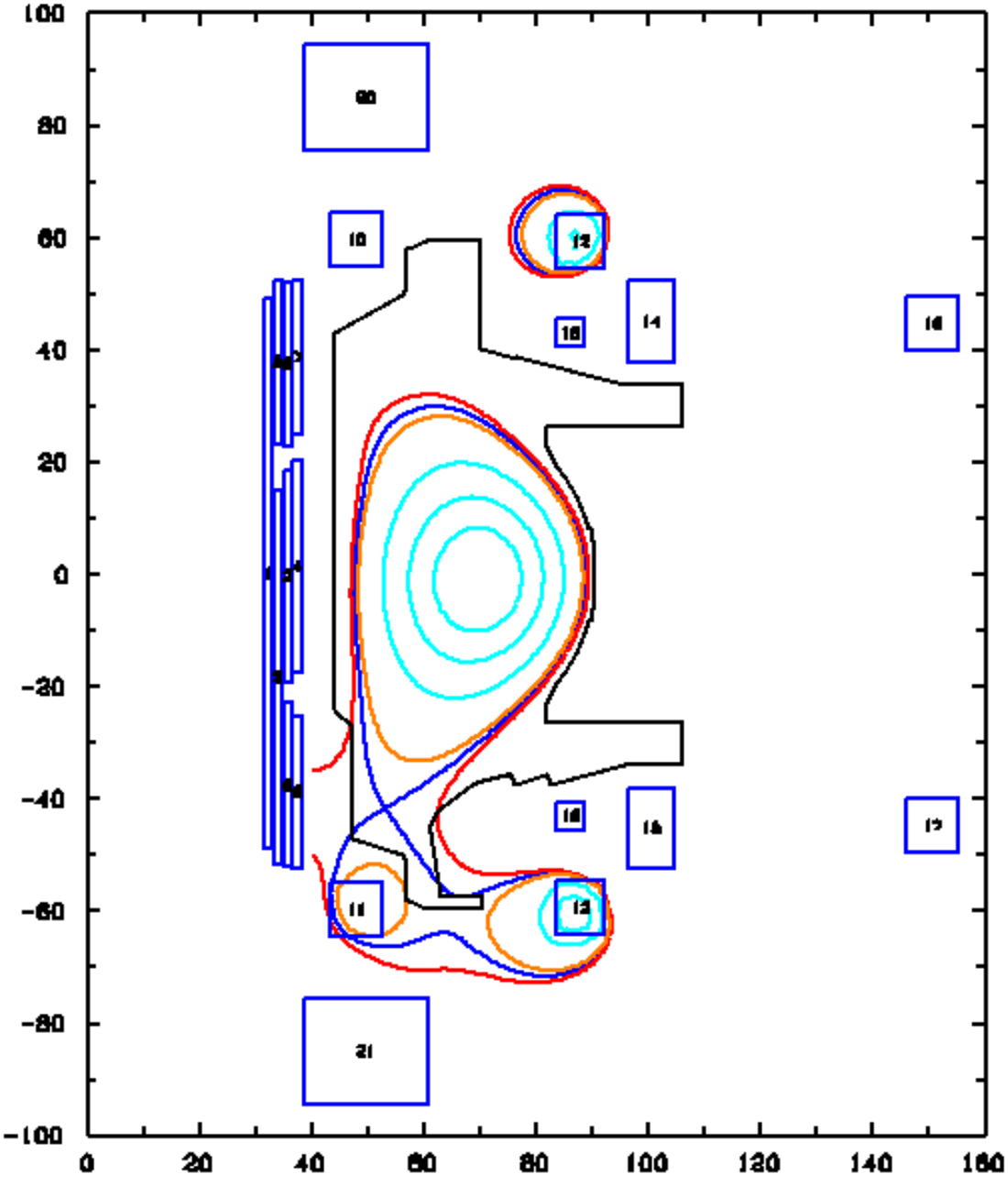

Figure 63: An X-Divertor for C-Mod, respecting all of the current restraints of the PF coil system.

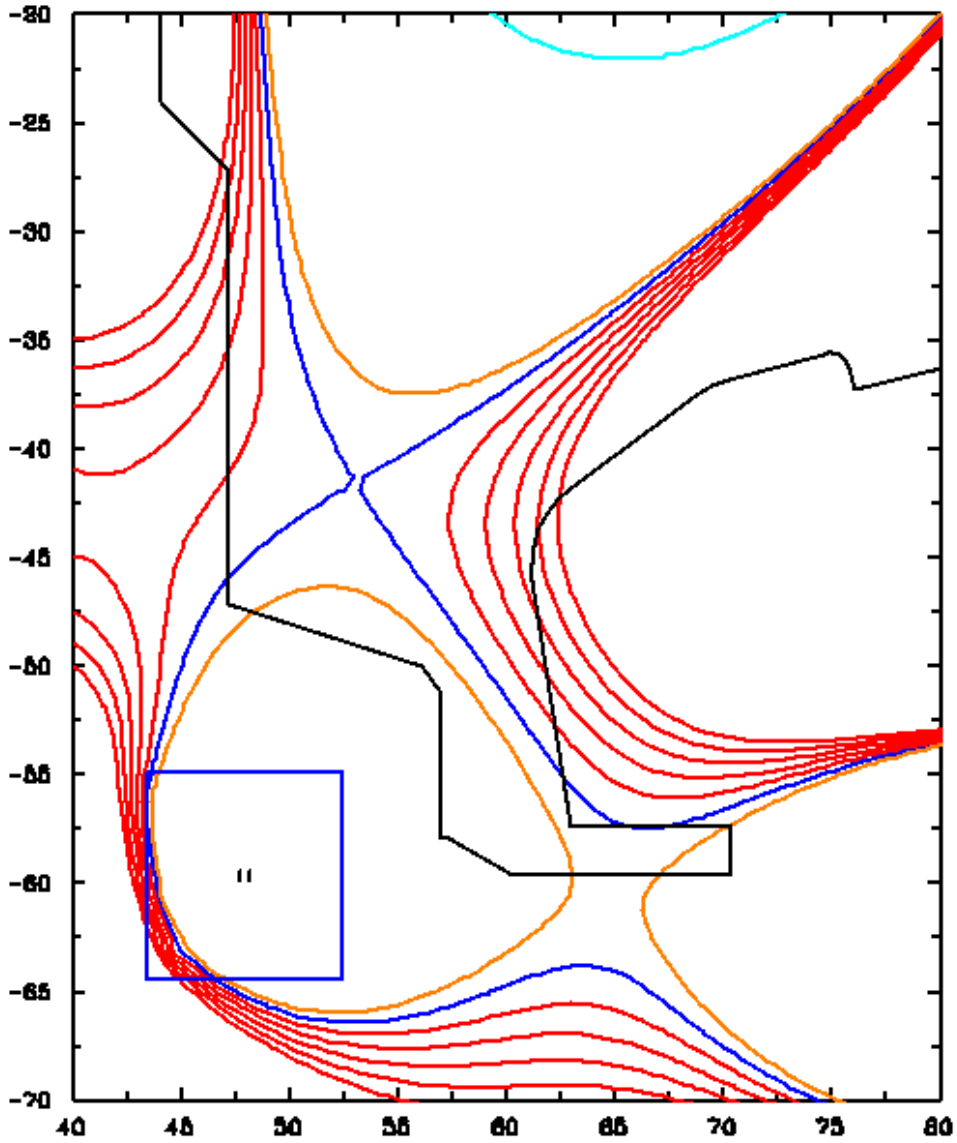

Figure 64: A close-up of the C-Mod X-Divertor. Each SOL flux surface (in red) represents a 1-mm increment in the outboard midplane width. Flux expansion and flaring here are much more modest than in the NSTX-U XD because the outboard strike point must be kept on an oblique target. However, in the C-Mod equilibrium, both inboard and outboard legs have flaring ($DI > 1$)

For C-Mod, we also have a standard divertor equilibrium, shown in Figs. 65 and 66, with which to directly compare the benefits of flux expansion and flaring in the XD.

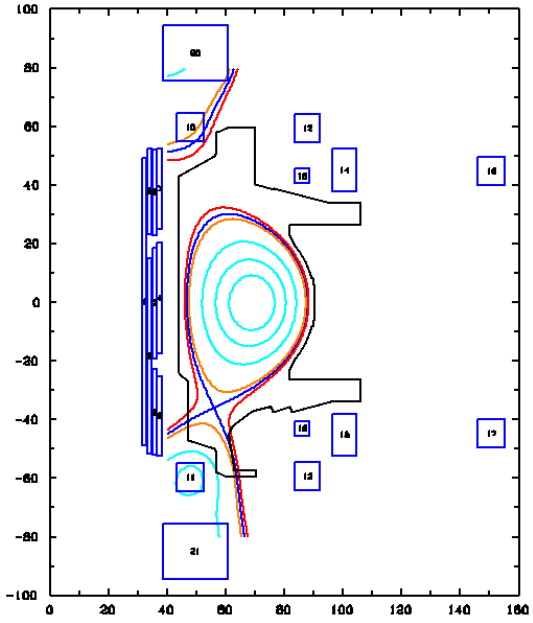

Figure 65: A standard divertor for C-Mod. The heat flux and temperature results from the equilibrium will be compared directly with the X-Divertor.

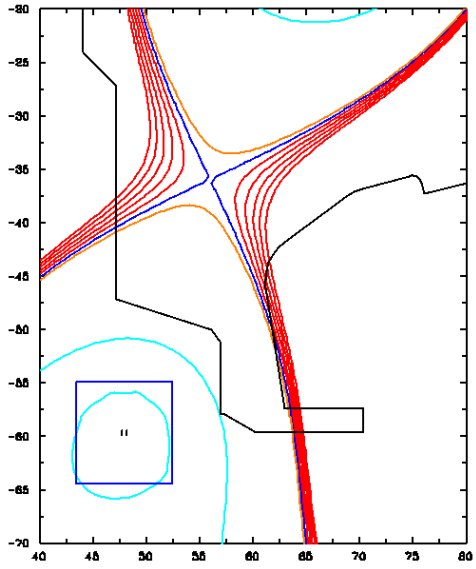

Figure 66: A close-up of the C-Mod standard divertor, our baseline case. Flux expansion at both targets is visibly much less than for the XD.

C-Mod Plasma Attributes		
	SD	XD
R_o (m)	0.67	0.68
a (m)	0.21	0.21
I_p (MA)	0.45	0.45
B_T @ R_o (T)	5.42	5.34
κ	1.60	1.72
δ	0.53	0.71
β_T	0.2%	0.2%
P_{SOL} (MW)	3	3
Inner flux exp.	2.8	16.8
Inner DI	0.91	1.26
Inner conn. length (m)	18.6	34.4
Outer flux exp.	1.6	10.3
Outer DI	1.05	2.49
Outer conn. length (m)	18.1	34.3

Table 2: Parameters for the C-Mod core plasma with both the SD and the XD. Flux expansion and flaring are reported for both inboard and outboard legs on both the SD and the XD. A small, secondary x-point was generated near the inboard target as well, raising *DI* there above 1. The great increase in connection length in the XD over the SD is also apparent.

As before, the SOL flux surfaces shown in red in Fig. 66 represent incremental outboard SOL widths from 1 mm to 5 mm, with the separatrix highlighted in blue. Unlike other tokamaks, plasma elongation and triangularity are incredibly important to advanced divertor design in C-Mod, due to the tight divertor space and limited strike point window. It is vital that the main x-point be placed low into the divertor region, and at high triangularity. This allows the outboard divertor leg to be made more perpendicular to the outboard target, getting the outboard strike point both lower on the target and closer to the secondary x-point nearby, as can be seen in Fig. 64. This improves flux expansion and flaring, as reported in Table 2, not to mention that more of the outboard SOL is

incident on the target this way. However, this may also restrict the inboard SOL to an undesirable degree; Fig. 64 shows how the 5-mm flux surface of the inboard SOL doesn't quite clear the inboard target. But since the power SOL width is so small, we don't expect much of the incident heat flux to strike the edge of the target, so we need only concern ourselves with the first few millimeters of SOL width.

A similar prescription to that of NSTX-U was used to develop the C-Mod XD. Here, the lobe of Coil EF1L forms an x-point with the plasma current lobe, and then EF2L forms the secondary x-point by joining lobes with EF1L. One will notice that unlike NSTX-U, the secondary x-point here resides inside the separatrix, rather than outside at the 1-mm surface, as we'd like. This was necessary to keep the strike point on the oblique outboard target; if the x-point is moved to the 1-mm surface, then the separatrix no longer terminates at the target. The direct result of this practical inconvenience is that flux expansion and *DI* at the outboard target are not as high as they could be, with the secondary x-point farther away from the strike point. Still, *DI* at the outboard target is 2.49 on the separatrix, and 1.66 on the 1-mm surface. Outboard flux expansion on the separatrix is 10.3, and 7.9 on the 1-mm surface.

We can see the effects of this modest increase in *DI* in the outboard divertor leg in Fig. 64. The flux surfaces just barely begin to flare before they terminate at the outboard target. In this way, we can see that the Divertor Index isn't necessarily about large, visible flaring, but merely flaring greater than that which the standard divertor offers, especially for *DI* only slightly greater than 1. What remains to be seen is what level of flux tube flaring is required to arrest the detachment front, and whether or not divertors like the C-Mod XD, with $DI \approx 2$, are sufficient to do it. One can be sure though that this answer will be tokamak-specific.

As it turns out, C-Mod also offers us a unique opportunity to test the rudiments of a dual X-Divertor, where secondary x-points are placed on both inboard and outboard legs simultaneously. Though not originally intended, the use of the lower solenoid coil winding, OH2L, to control plasma triangularity resulted in a small x-point being created near the inboard leg (Fig. 64), increasing flux expansion and flaring on the inboard SOL. *DI* at the inboard target on the separatrix is 1.26, and 1.48 on the 1-mm surface. Because the main x-point and inboard secondary x-point are in close proximity, inboard flux expansion is considerable: 16.8 on the separatrix, and 24.6 on the 1-mm surface.

9.3. HEAT FLUX HANDLING AND DETACHMENT IN C-MOD

The B2.5-Eirene meshes for both the C-Mod SD and XD are shown in Fig. 67.

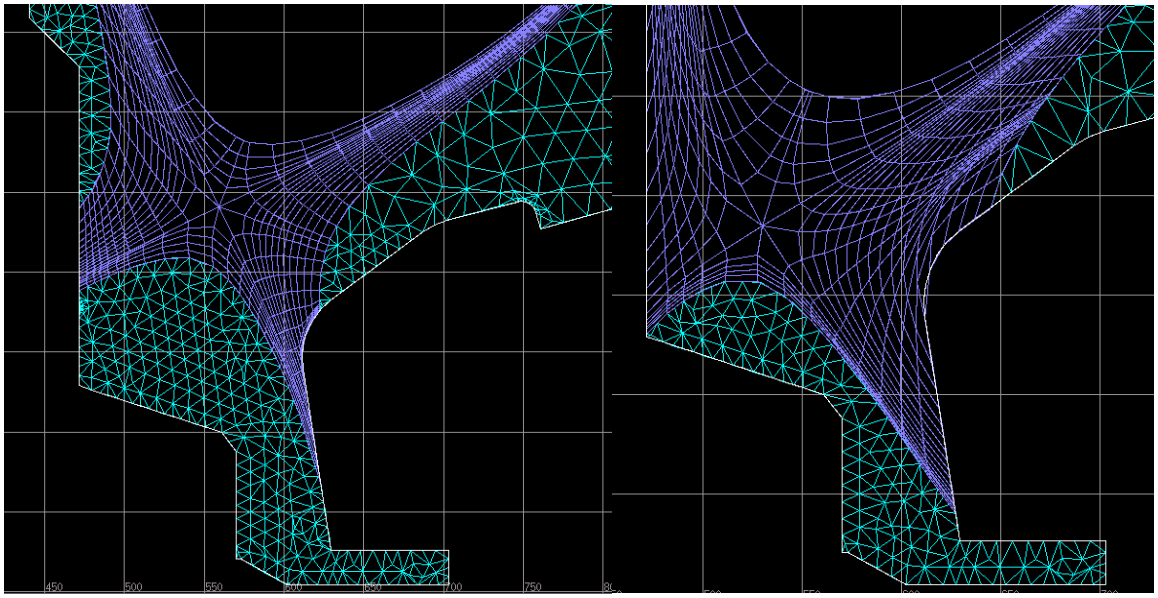

Figure 67: The B2.5 (violet) and Eirene (green) meshes for the C-Mod standard divertor (left) and the X-Divertor (right).

Because in C-Mod we have an SD and an XD to compare directly, every effort was made to standardize the modeling parameters (gas puff rate, impurity injection rate, etc.), so that any differences arising from the differing geometries could be observed, not just effects at the targets. Transport coefficients were also standardized once the power SOL width was matched to our expected value in the SD case. In this case, $X = 0.1$ (and $D = 0.03$) turned out to be the appropriate value of heat diffusivity to yield a power SOL width of 1.3 mm for the SD case. The same coefficients were then used in the XD case. Having a reliable source on the C-Mod SOL midplane density profile, 8×10^{19} m^{-3} was the appropriate edge electron density to shoot for with deuterium gas puffing. In the SD case, this was achieved almost exactly at 8.02×10^{19} m^{-3}. Interestingly, for the same gas puffing rate, the XD edge density was lower at 6.89×10^{19} m^{-3}.

For impurities, the ideal case would include carbon and molybdenum species, since these are the primary radiators in C-Mod. However, the atomic number of molybdenum is very high at $Z = 42$, and it is uncertain at this time whether SOLPS 5.1 can accurately model its atomic physics, not to mention the incredible computation time required to follow all of the charge states. Therefore, a decision was made to use argon as a generic, radiating impurity in C-Mod. Z_{eff} in the core was kept below 1.3, though argon is a weaker core radiator than molybdenum. For simplicity, chemical and physical sputtering models were turned off, so carbon was excluded as well. Consequently, it may then be very important to reassess at a later time the appropriate impurity physics to include in the C-Mod model. However, the results of this simpler model are still informative, as the temperature plots in Fig. 68 show:

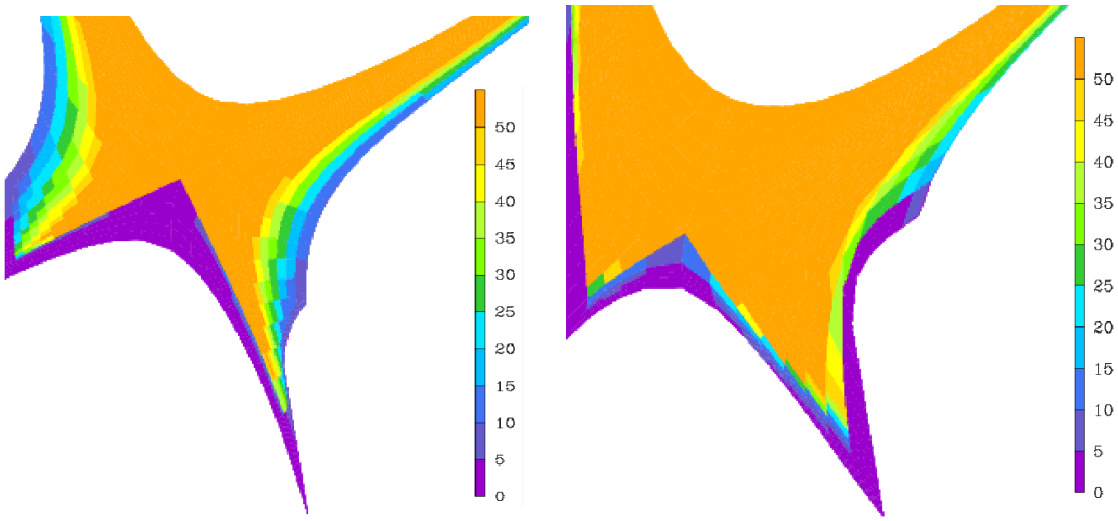

Figure 68: Electron temperature color plots (scale in eV) for the SD (left) and the XD (right). The stark drop in the parallel temperatures near the XD targets is striking, indicating that both legs have entered detachment and are so far stable. Under identical gas and impurity puffing conditions, the SD remains attached to the targets, implying that the flux expansion of the XD indeed encourages detachment.

The key observation to take away from Fig. 68 is the dramatic drop in the plasma temperature near the XD targets, and the violet region of low temperature that buffers the plasma at both targets – the divertor seems to be on the verge of arrested, full detachment in *both* inboard and outboard legs. Compare this result with the SD temperature plot in the same figure, where the outboard leg is still attached to the target, and the inboard leg may be in a phase of partial detachment. Recalling that gas puffing rates for the two equilibria are equal, these results would seem to indicate that the XD geometry does indeed hasten the onset of detachment via its flux expansion at the target plates. This result is even more striking when we remember that the upstream edge density for the XD case is *lower*, which should work *against* the XD detaching first. The contrast in the states of the equilibria also shows in the parallel temperature profiles shown in Fig. 69.

The sharp drop in plasma temperature as one approaches the XD targets is indicative of the establishment of a neutral buffer.

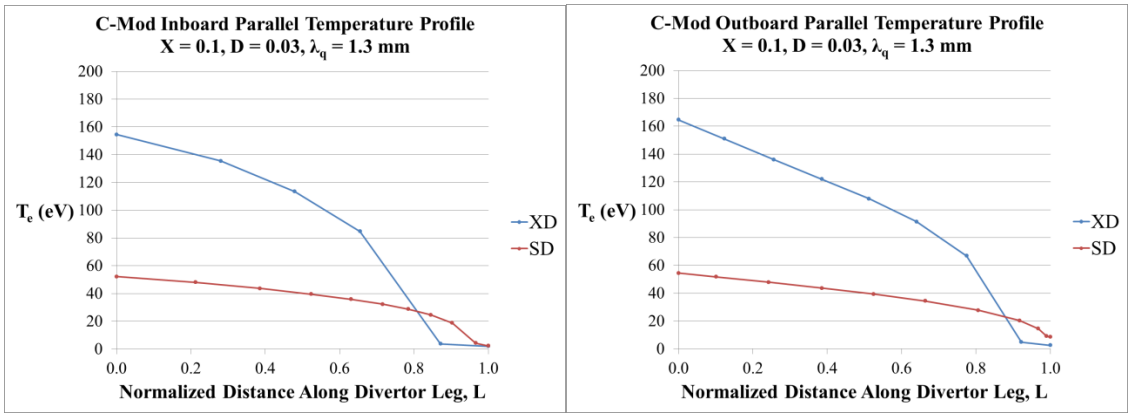

Figure 69: Both inboard and outboard legs, where $DI > 1$, of the XD show sharp parallel temperature gradients near the targets. Analogous profiles for the SD have no such gradient.

And while the temperatures at the plates in both cases are minimal (Fig. 70), one can see in Fig. 71 that the still-attached SD case has a significant heat flux at its *inner* target, and the XD heat fluxes are both small.

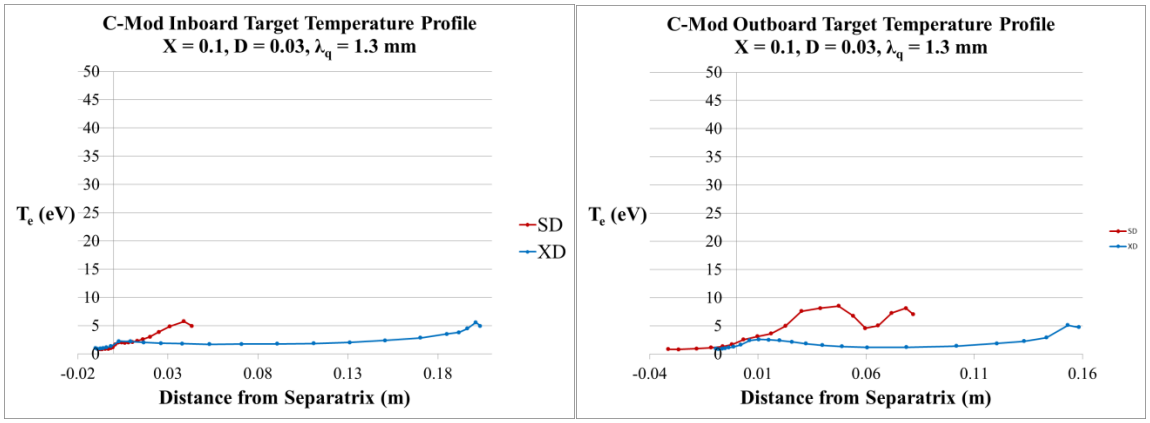

Figure 70: Target temperature profiles in both divertors have low peak values. The X-Divertor appears to be in detachment. Note the considerably larger target area spanned by the X-Divertor.

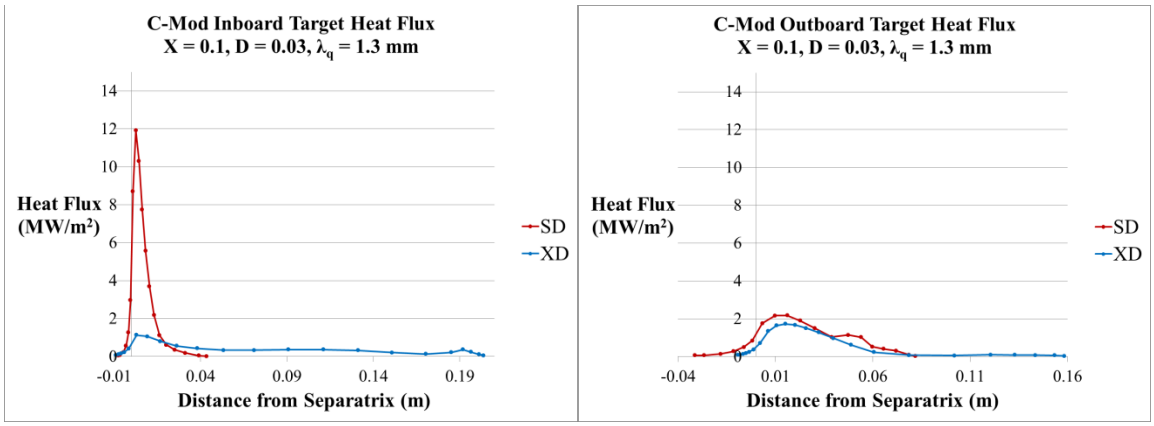

Figure 71: In the SD, the peak heat flux has shifted to the inboard target, resulting in an excessively high intensity. In the XD, both inboard and outboard heat fluxes are well mitigated.

Apparently, even modest increases in the Divertor Index from an SD to an XD can quickly yield positive results for increasing the plasma-wetted area on the targets and encouraging detachment. The next step in testing this highly promising, initial result will be to bring the SD equilibrium into full detachment, seeing if and where the detachment front can stabilize as well.

Chapter 10:

CFNS / FNSF

10.1. THE CFNS TOKAMAK

Changing direction from existing tokamaks, we take some time to examine the possibilities of advanced divertors on future tokamaks whose PF coil and target designs still have a lot of flexibility. In doing this, we can kill two birds with one stone by considering an equilibrium suitable for two different applications: a Compact Fusion Neutron Source (CFNS), and a Fusion Nuclear Science Facility (FNSF), conceptualized in Fig. 72. The former application serves as the fission-waste-destroying neutron source in the hybrid reactor scheme described in Sect. 2.2, while the latter is the next-generation tokamak to succeed NSTX-U and serve as a neutron science testing facility, mentioned in Sect. 8.1. In both of these tokamaks, the goal is the same: efficiently produce a $Q \leq 1$ plasma in a low-aspect ratio tokamak to act as a steady fusion neutron source. For simplicity, this tokamak will heretofore be referred to just as CFNS.

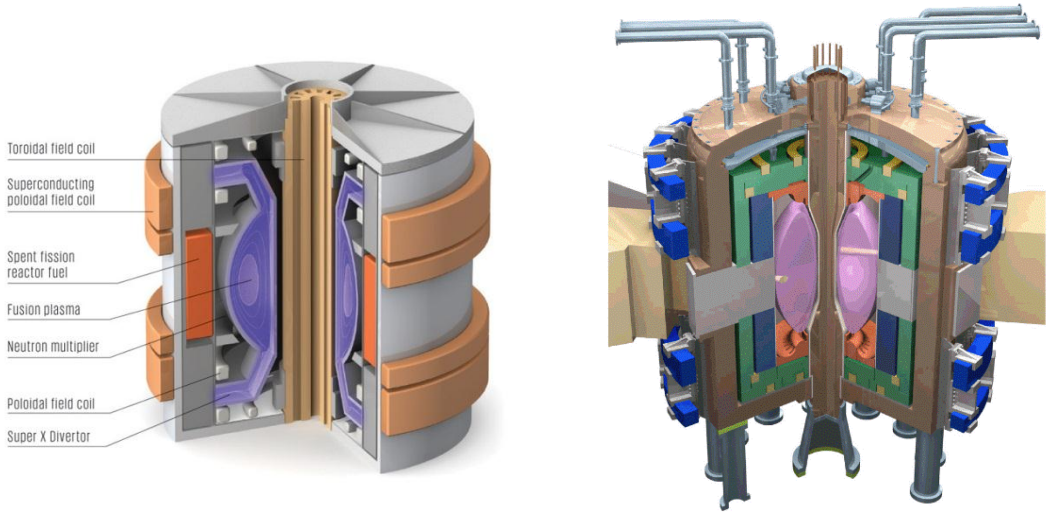

Figure 72: A Compact Fusion Neutron Source (CFNS, left) and a Fusion Nuclear Science Facility (FNSF, right) are two proposed applications for compact, low-aspect ratio tokamaks to advance neutron science.

But as we discussed with NSTX-U, the heat flux handling problem is exacerbated in low-aspect ratio tokamaks. Moreover, a CFNS plasma will operate at much higher power than NSTX-U, meaning that we can expect more power entering the SOL and higher heat fluxes at the divertor targets. Thus, we are motivated to consider the strongest option we have to mitigate heat fluxes, the Super X-Divertor. In existing tokamaks, the SXD is usually unfeasible because of the extra required space for its extended outboard divertor leg. However, for a future tokamak like CFNS, we can make design decisions from the ground up that allow for an SXD.

As with any advanced divertor, it is beneficial to have PF coils near the target plates, to locally manipulate the magnetic field and create flux expansion and flaring. This is especially true for the SXD, where the outboard strike point will not be able to benefit from the poloidal flux expansion of the main x-point from a much larger major radius. Therefore, we seek to include PF coils *inside* the vacuum vessel, to assist in

poloidal flux expansion at the SXD target, and also to help shape the plasma. These in-vessel coils are not able to be made superconducting, as there is not enough room in the vacuum vessel for the necessary liquid helium/nitrogen cooling systems. Therefore, the in-vessel coils will be composed of a conductive metal alloy, like a copper alloy, or perhaps aluminum, which can withstand neutron fluences better than copper. Resistive power losses in the in-vessel coils then become an issue to consider in the power economics of the reactor, and we are particularly motivated to minimize their currents, since $P_{Ohmic} \propto I^2$. Coils that we may employ outside of the vacuum vessel and the TF coil may still be superconducting.

Other restrictions on the PF coils have to do with the nuclear environment of CFNS. Because we seek to use the fusion neutrons from the core to either destroy fission waste or conduct experiments, we must leave a wide swath of space for this task at the outer midplane. This restricts us from the use of in-vessel PF coils near the midplane. To adequately protect the in-vessel PF coils from neutron fluences, it is estimated that at least 50 cm of shielding is required between any coil and the plasma. Accounting for the minimum distance the plasma will need to be kept from the first wall, this means that no PF coil we employ should be within 55-60 cm of the core at any point. This rules out virtually all of the inboard side, where there will be little shielding for the TF center post anyway.

We assume a double-null plasma for CFNS. As we're only interested in a first estimate of divertor heat fluxes, we keep the atomic physics in the CFNS model simple – deuterium plasma with injected argon impurities. Chemical and physical sputtering models are turned off as well. We seek transport coefficients that will assume a narrow SOL width of about 1 mm. Based on the current limits of target material engineering, the

goal of the SXD is to keep heat fluxes at the outboard targets below 10 MW/m^2. The inboard divertor, of course, must satisfy this limit as well.

Our desired edge density is 3×10^{19} m^{-3}, but the gas puffing rate to achieve this density must be of the order of 1×10^{22} particles per second or less, as the CFNS plasma is a D-T plasma. Tritium recycling demands dictate that retention in the vacuum vessel walls be minimal, requiring that the gas throughput be limited.

10.2. A SUPER X-DIVERTOR FOR CFNS

The TEQ equilibrium for the CFNS Super X-Divertor and associated PF coils are shown in Figs. 73 and 74.

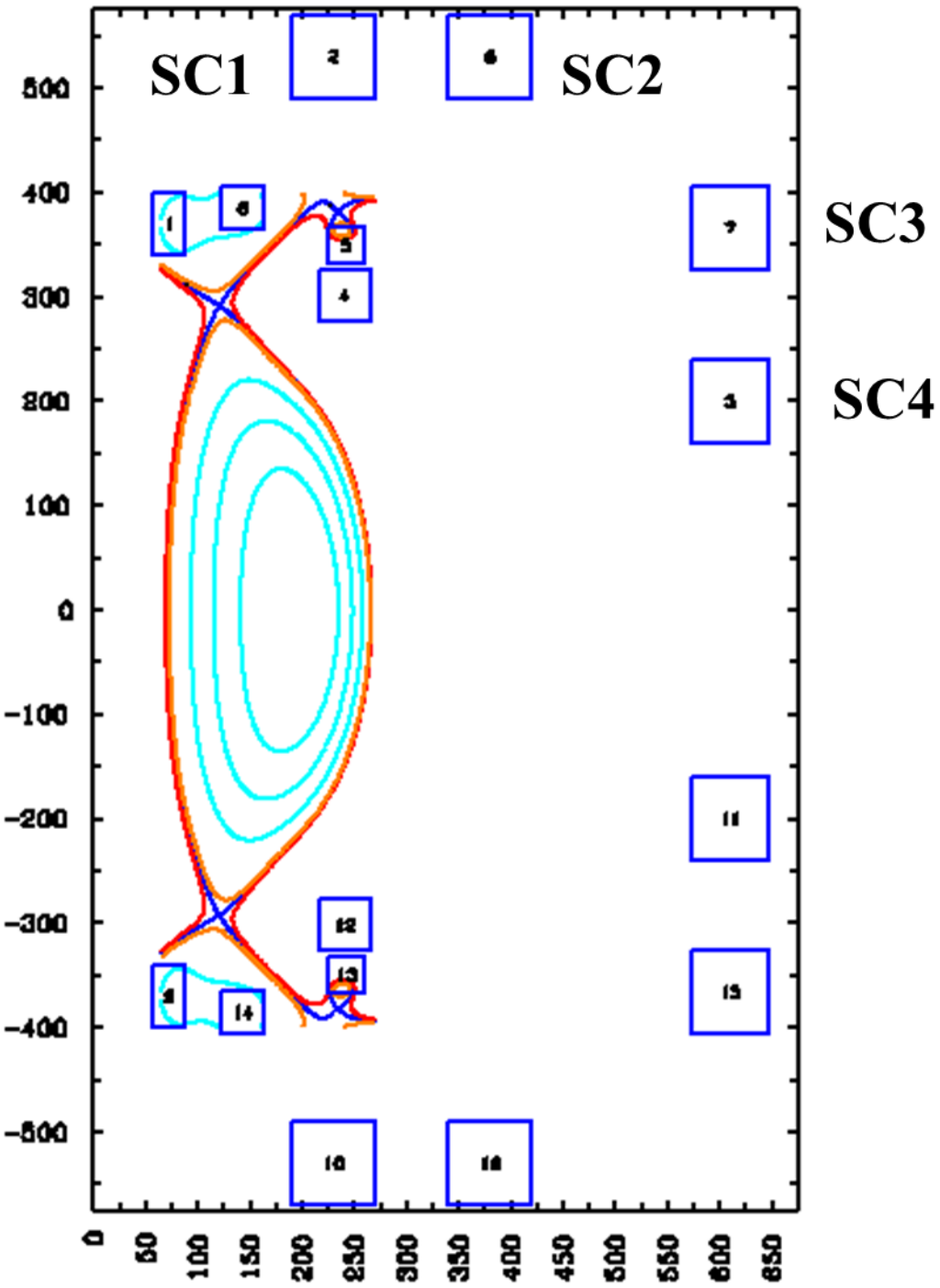

Figure 73: This hypothetical CFNS PF coil system utilizes in-vessel, copper/aluminum coils and external superconducting coils to create a Super X-Divertor. All coils are top-down symmetric.

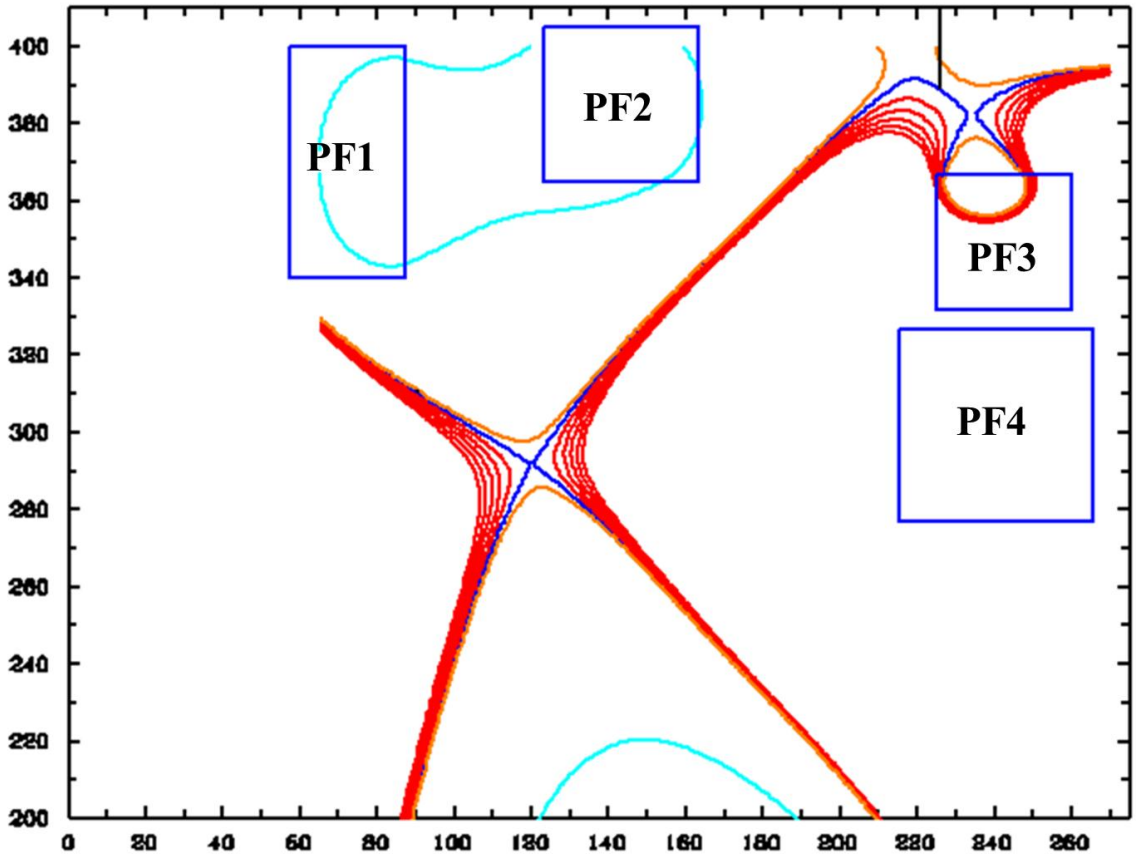

Figure 74: A close-up of the upper CFNS Super X-Divertor. The outboard leg is drawn out to a large major radius to create toroidal flux expansion, while in-vessel coils are used to create local poloidal flux expansion at the strike point.

CFNS SXD Plasma Attributes	
R_o (m)	1.69
a (m)	0.98
I_p (MA)	11.61
B_T @ R_o (T)	2.34
κ	2.97
δ	0.48
β_T	25.9%
P_{SOL} (MW)	50
Outer flux exp.	30.6
Outer DI	53.37
Outer conn. length (m)	26.6

Table 3: Parameters for the CFNS core plasma with an outboard SXD. SXD flux expansion and flaring are also reported. *DI* is incredibly high both because of a large increase in *d* to the outer target, and because of good poloidal flux expansion and a reduction in B_P at the outer strike point.

It's clear from Fig. 74 what makes this divertor a Super X-Divertor: multiple x-points in the outboard SOL create poloidal flux expansion and flaring at a strike point at a large major radius relative to the main x-point. Coils PF1 and PF2 work together to form a positive lobe that forms the main x-point with the plasma current lobe. Superconducting coil SC2 uses its large, positive current from outside the TF coils to draw out the outboard divertor leg, while SC1 uses a large, negative current to pinch the SC2 lobe and force the creation of a secondary x-point at large major radius. Then, to further broaden the low-field region near the outboard target, PF3 creates a tertiary x-point by linking positive lobes with SC2. Because the superconducting coils must act over large distances, the plasma becomes susceptible to their influence as well. Therefore, PF4 runs a negative current to push the plasma shape toward the inboard, effectively shielding the plasma from the strongest effects of the superconductors.

The resultant flux expansion at the outboard target on the 1-mm surface is 30.6, while *DI* is an incredible 53.37. This high value is due both to the increase in d_{target}, and the reduction of B_P with good poloidal flux expansion. Moreover, the toroidal field drops by about half going from the main x-point to the target plate, greatly increasing the plasma-wetted area in the toroidal direction. Other plasma attributes are listed in Table 3.

Unsurprisingly, the lack of an inboard, positive PF coil hurts the ability of the plasma to be pushed to higher triangularities. This has also severely hurt flux expansion of the inboard divertor leg, as there is no PF coil nearby to work to cancel out the local field. To improve the situation, it is of some great interest in the future to explore the possibility of machining a thread on a section of the TF center post, effectively creating a PF current on the inboard side. This concept would work in the same way that the TF coil joint in C-Mod creates a local PF current source at the top and bottom of the machine.

10.3. HEAT FLUX HANDLING AND DETACHMENT IN CFNS

Despite the unusual nature of the Super X-Divertor leg compared to a standard divertor, a mesh for B2.5-Eirene was able to be generated, shown in Fig 75. The outboard target was oriented using the target generator script, to keep the incident field angle at 1° near the separatrix, thereby avoiding target tile hot spots. The inboard target had to be oriented simply to prevent the inboard SOL from striking the first wall upstream, as space on the inboard side is tight. Everywhere, the divertor corridor is kept a narrow as possible, to encourage higher neutral pressures and better pumping efficiency at the outboard.

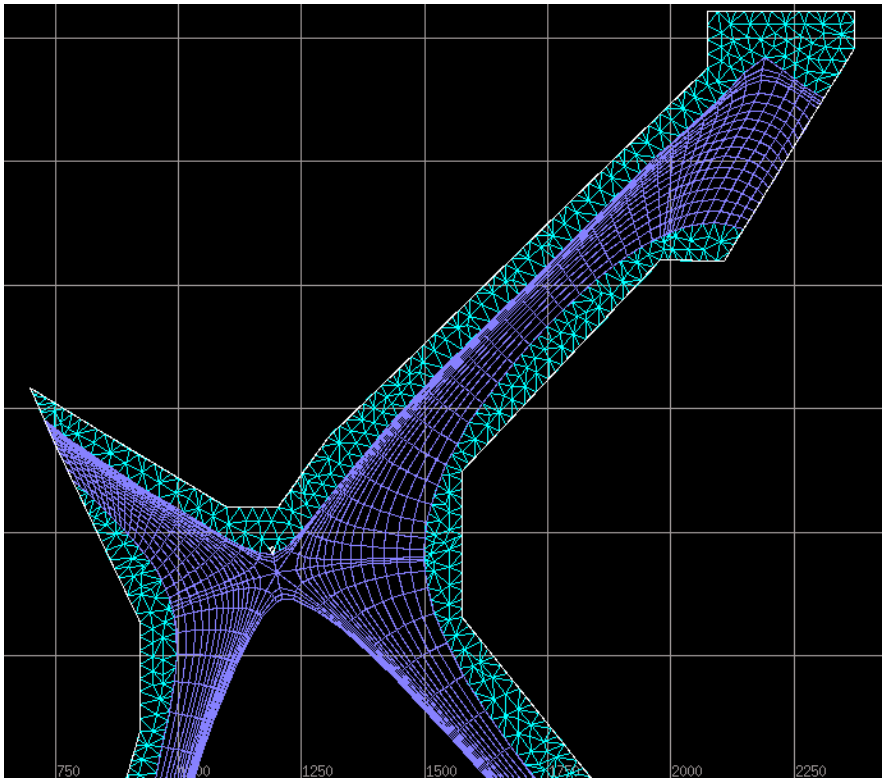

Figure 75: The B2.5 (violet) and Eirene (green) meshes for the CFNS Super X-Divertor.

The outboard power SOL width for this case was found to be 1.1 mm. With careful gas puffing on both the inboard and outboard sides, the edge density reached a steady-state value of 3.02 x 10^{19} m^{-3}, right at our desired value. Z_{eff} in the core is 1.6, slightly higher than desired. Despite the unfavorable inboard conditions, the resultant temperature plot in Fig. 76 is encouraging:

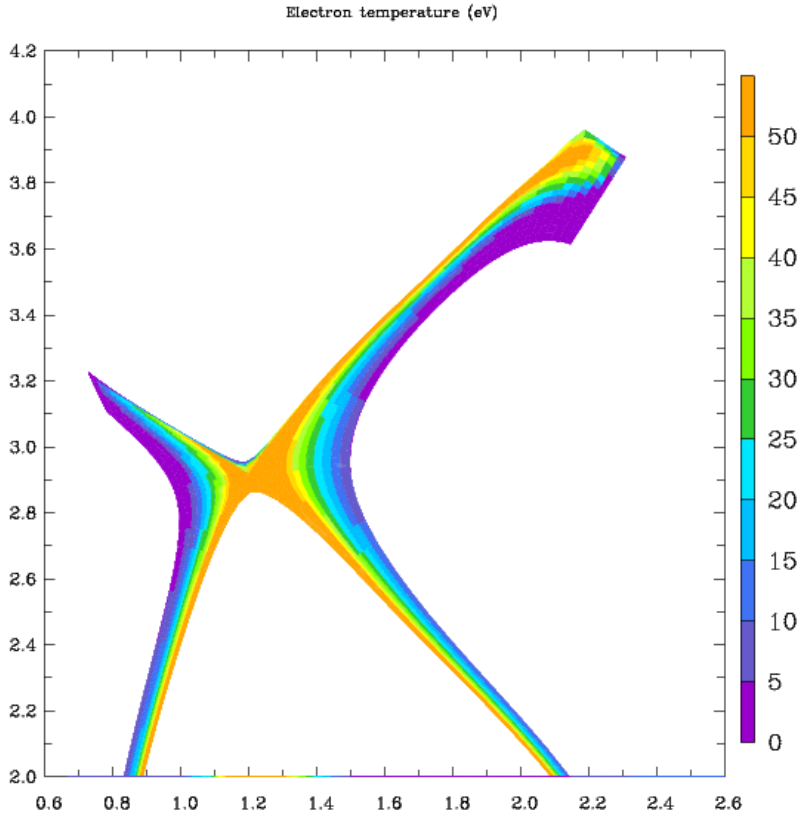

Figure 76: Both inboard and outboard legs are still attached to the targets, but temperatures at the plates are low.

At this gas puffing rate and edge density, the outboard leg is not quite detached; rather, it is partially detached, with small plasma temperatures at the target (Fig. 77). This appears sufficient, however, as the peak heat fluxes at both inboard and outboard targets stay well below 10 MW/m^2 (Fig. 78).

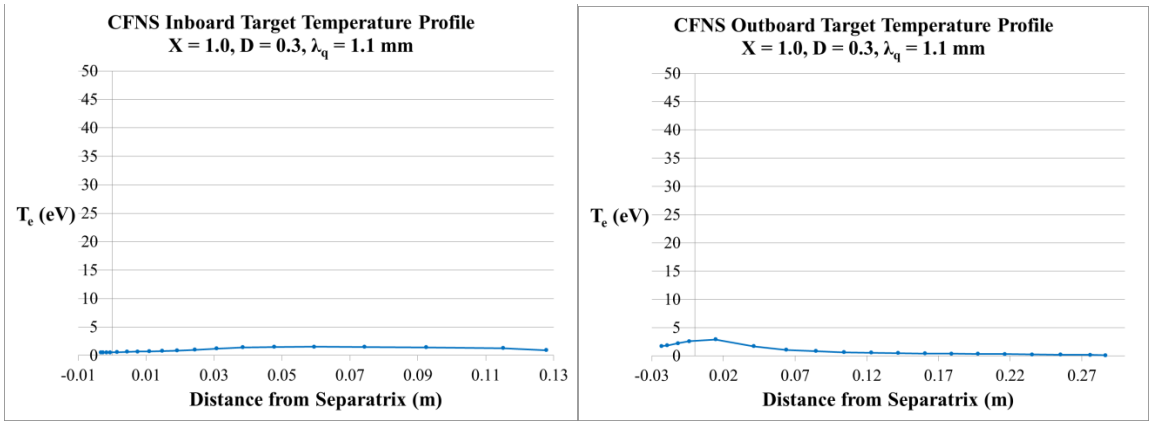

Figure 77: CFNS inboard and outboard target temperature profiles.

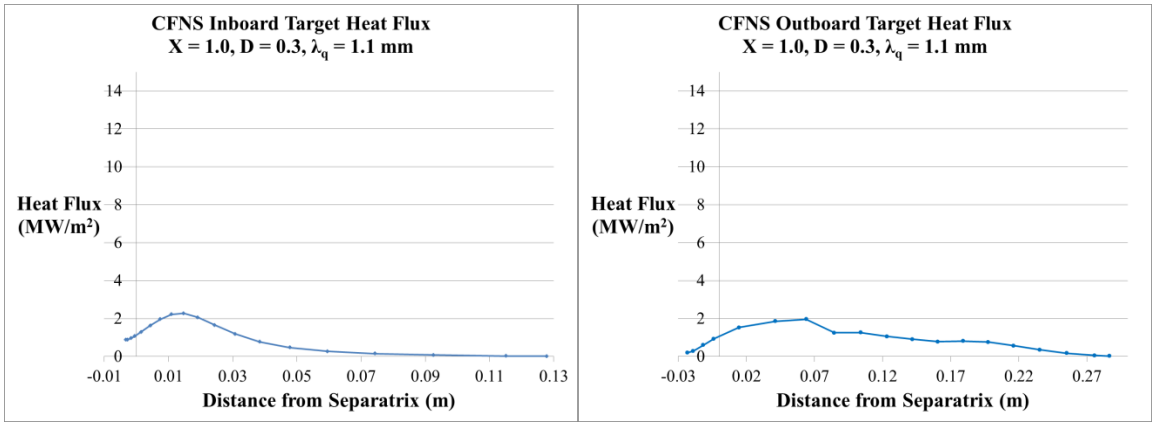

Figure 78: CFNS inboard and outboard target heat flux profiles.

And once again, the contrast in Divertor Index between the inboard and outboard legs is apparent via the parallel temperature profile, shown in Fig. 79. A steep temperature gradient exists near the target on the outboard SXD, while no such gradient exists on the inboard leg.

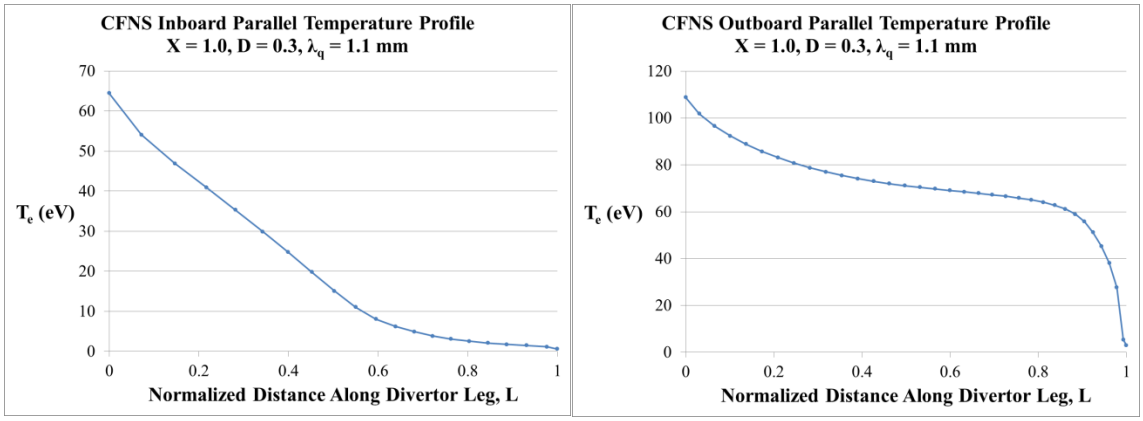

Figure 79: The parallel temperature profiles between the inboard and outboard divertor legs are indicative of their respective Divertor Indexes. A steep temperature gradient exists near the outboard target of the SXD, where $DI >> 1$.

This initial result indicates that the Super X-Divertor can handle the intense heat load demands of the CFNS and FNSF tokamaks, even with very narrow SOL widths, and almost three times the power going to the outboard targets compared to the inboard targets. However, more work needs to be completed before conclusions can be drawn. Despite the top-down symmetry of the double-null, in some cases, the outboard SOL power was observed to shift preferentially toward one target, resulting in peak heat fluxes over 20 MW/m^2. This asymmetry needs to be addressed.

Chapter 11:

ITER

11.1. The ITER Tokamak

So far, based on our successes creating advanced divertors for tokamaks both present and future, and the favorable heat flux results they have given in SOLPS, we are highly motivated to attempt to design an advanced divertor for the single-null plasma on ITER, the premiere, international tokamak project shown in Fig. 80. One perhaps couldn't envision a more highly constrained system, however; as a massive, multi-billion-dollar project under the oversight of seven governments, and with a construction timeline on the order of decades, there is virtually no leeway in any design specification, let alone room for consideration of a new type of divertor. Therefore, an advanced divertor must use only the planned PF coil and solenoid system, a system which was never designed for flexibility.

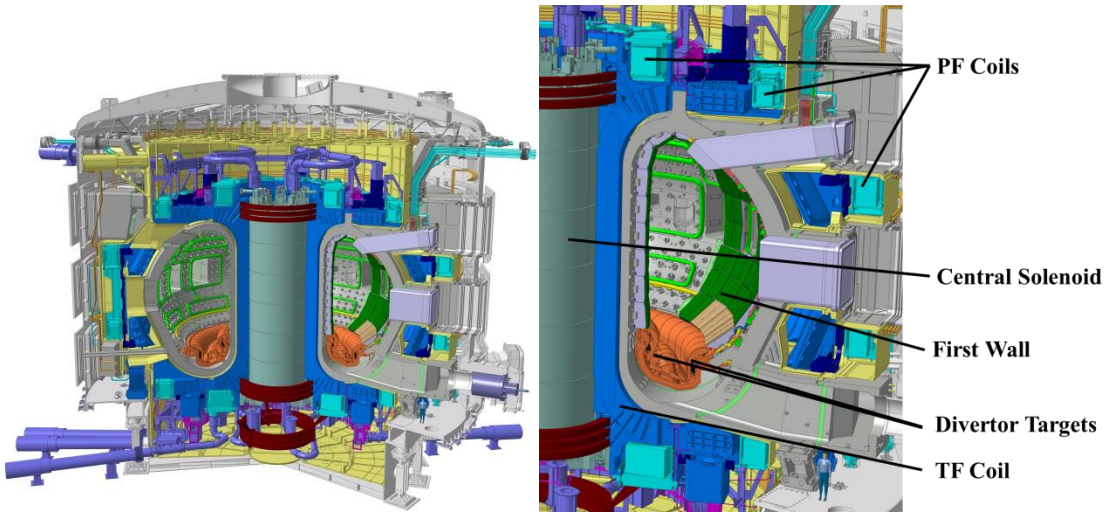

Figure 80: The design of the massive ITER tokamak [25] is heavily constrained.

Moreover, there can be no substantial changes to the plasma shape, as the first wall will be tightly conformal to the planned plasma. As a rule of thumb, the ITER plasma must be kept at least 15 cm away from the wall everywhere [26]. The dome structure, used as a baffle in the private region to increase neutral pressure in the divertor, cannot be made to intersect either the inboard or outboard divertor legs due to changes in the magnetic geometry we may wish to make. The divertor targets themselves are oriented to be at 2° with respect to the field of the standard divertor, and while the target tiles are staggered with respect to each other to prevent hot spots, a significant reduction in B_P will cause shadowing effects on the tiles, actually *decreasing* the plasma-wetted area (Fig. 81) [27]. This is assuming that any advanced divertor we design with improved flux expansion will keep its strike points on the planned targets, which, of course, will be required.

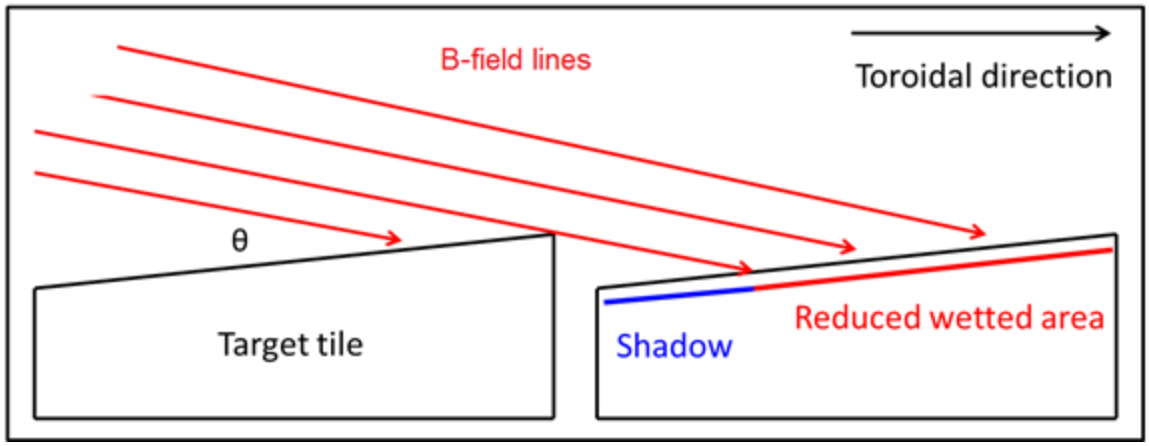

Figure 81: Counterintuitively, poloidal flux expansion in ITER eventually results in a reduction of the plasma-wetted area. Because the ITER target tiles are staggered to avoid hot spots, a reduction of the angle $\theta = tan^{-1}(B_P/B_T)$ creates shadows on the tiles, where no incident plasma can reach. Therefore, our interest is not necessarily with flux expansion, but with flaring enabling stable detachment. Note that the same target design would not incur the shadowing problem with an SXD, where both B_P and B_T are reduced.

The PF coil system consists of 6 superconducting coils evenly distributed along the outboard side, from top to bottom. Six more coils, stacked vertically on the inboard side, comprise the central solenoid (CS) for inductive plasma current drive. While the even distribution of the coils provides for a certain degree of versatility, the real difficulty of the ITER coil system is that all of the coils are located *outside* of the TF coil, far away from the interior of the vacuum vessel where we wish to manipulate the magnetic geometry. Therefore, we are forced to use large currents to influence the field at great distances, and it will be difficult to separate the tasks of divertor shaping and plasma shaping.

Having properly sobered ourselves on the immense challenge of advanced divertor design on ITER, we are justified in asking whether or not the potential benefits are worth the effort. That judgment depends largely on how much credibility one lends to

the extrapolation of Goldston's formula for ITER, first mentioned in Sect. 5.3. If λ_q is closer to 5 mm as originally projected, then SOLPS results performed by Andrei Kukushkin indicate that a standard divertor should succeed in keeping peak SOL heat fluxes below 10 MW/m^2. If, however, λ_q is closer to 2 or even 1 mm, then the question of whether or not advanced divertors are worth researching may become the question of whether or not ITER can afford to operate at long periods without one.

11.2. AN X-DIVERTOR FOR ITER

At this point, it becomes important that we take to heart the last comment of Sect. 4.2 – that the transition to an advanced divertor like an XD from an SD is *continuous*. Therefore, because of ITER's rigid constraints, we do not seek to start from scratch to create a powerful XD, but instead to perturbatively change the ITER standard divertor, seeing how much added benefit in flux expansion and flaring we can yield before we bump up against any one of our constraints. The two main constraints with which we have to contend are (a) coil current limits, and (b) keeping the core plasma away from the first wall. With this refocusing of our goal, the ITER advanced divertor problem becomes a lot more tractable, and all that remains is to see how much improvement in divertor performance we can achieve.

The TEQ results of our perturbative approach are shown side-by-side with an ITER standard divertor in Figs. 82 and 83.

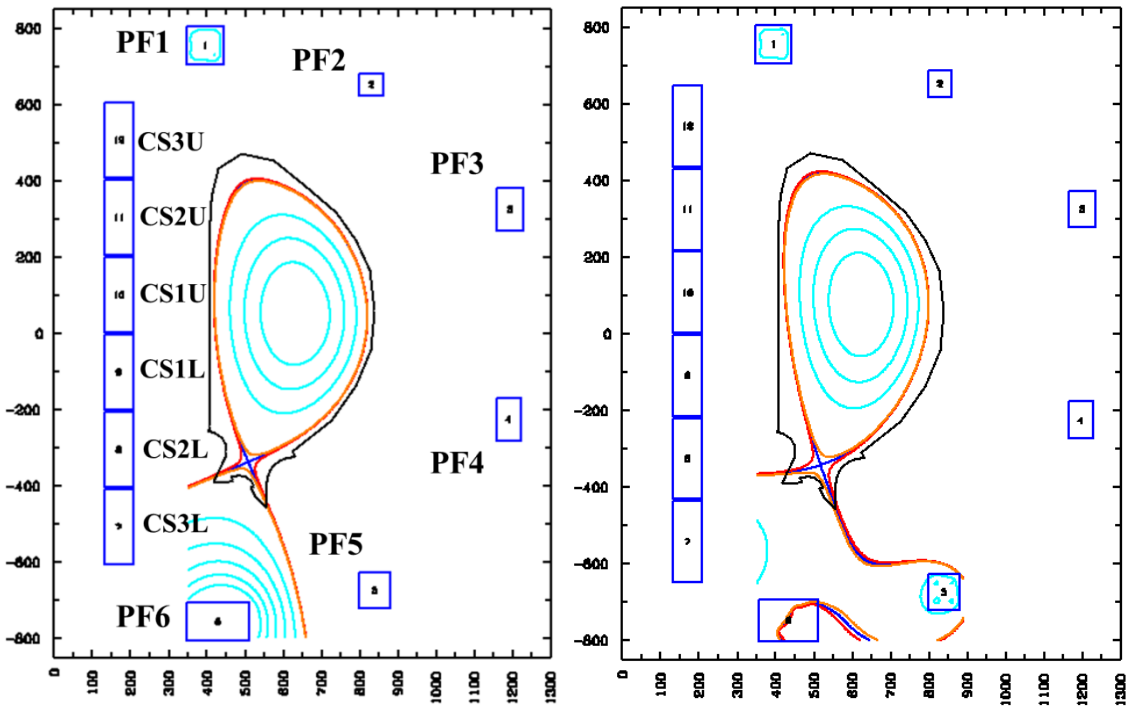

Figure 82: Using only the planned PF and CS coil sets, respecting coil current limits, and keeping the core plasma away from the first wall, an X-Divertor (right) can be transitioned perturbatively from a standard divertor (left), with a distant, secondary x-point on the outboard leg.

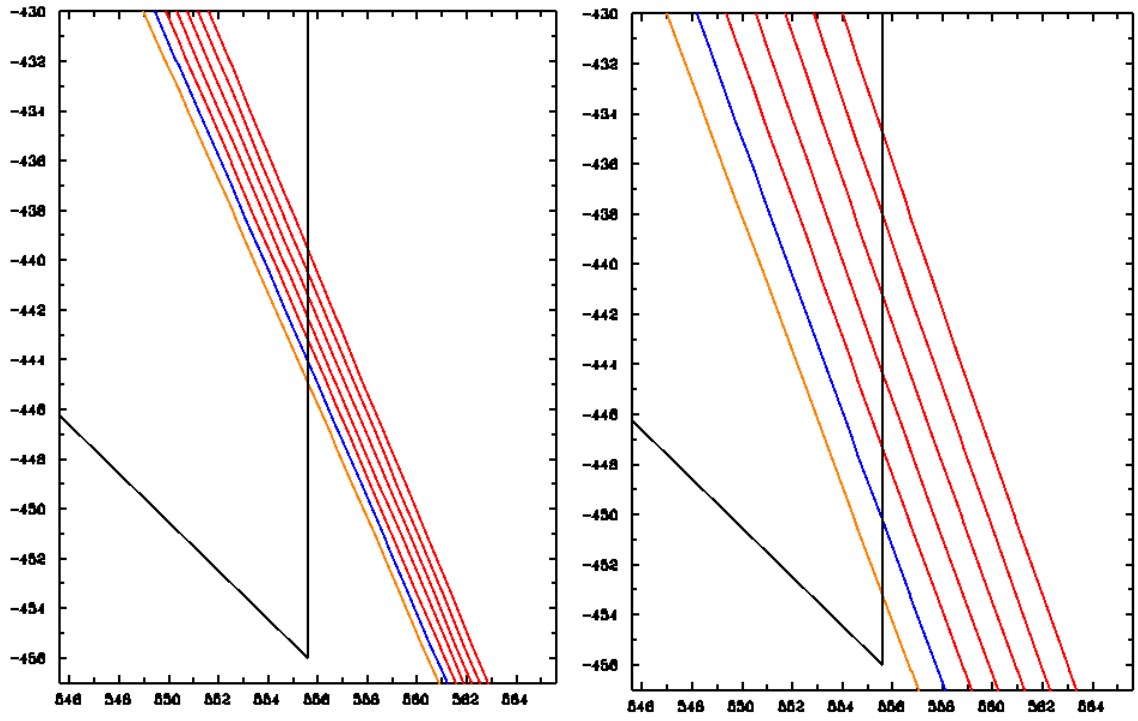

Figure 83: A close-up of the outboard strike point of the SD (left) and the XD (right). Flux surfaces shown (in red) represent 1-mm increments of the outboard midplane width. Flux expansion and flaring are underwhelming compared to results from NSTX-U and C-Mod, but perhaps even this level is sufficient to address the ITER heat flux concern.

We can see the effects of our perturbative approach on the magnetic field outside the vacuum vessel. While in the SD, PF6 was responsible for creating a positive lobe and an x-point with the plasma current, now in the XD, that job has been taken over by CS3L, the lowest coil on the center solenoid. PF5 then joins lobes with CS3L, forming a secondary x-point, and PF6 now actually runs a negative current, to push the x-point as close to the target as possible within coil current restrictions. PF4 runs a negative current to keep the main x-point in its place, preventing PF5 from attracting it downward.

Of course, we have insisted before that the magnetic field outside the region where the plasma exists is irrelevant, and rightly so. Taking a closer look at the outboard

targets of the ITER SD and XD in Fig. 83, we see an almost threefold increase in flux expansion (from 2.6 to 7.3) and a mild increase in flaring (*DI* from 1.07 to 1.76). And even though the secondary x-point is very far away, even the inboard target sees a noteworthy improvement in flux expansion (from 2.3 to 4.0).

The sum of the currents in the CS is roughly the same, preserving the net flux swing through the solenoid, but a force analysis between the coils with their new, XD currents has not yet been performed. We see that the XD core plasma is still contained within the original first wall, but at some cost to plasma volume; the minor radius had to be reduced from 200 cm to 186 cm. Fortunately, this has no adverse effect on the energy confinement time of the plasma, which actually increased from 3.00 s to 3.28 s according to the ITER98(y,2) scaling law [28]. While the loss of minor radius hurts confinement time, the bump in elongation more than makes up for it. What does become a concern, however, is the effect the increased elongation may have on the vertical stability of the plasma. Increased elongation is well known to increase the growth rate of vertical instabilities. Tests on the vertical stability of the ITER XD plasma are planned for the future.

ITER Plasma Attributes		
	SD	XD
R_o (m)	6.20	6.13
a (m)	2.00	1.86
I_p (MA)	15.00	15.00
B_T @ R_o (T)	5.30	5.36
κ	1.84	2.05
δ	0.52	0.48
β_T	2.5%	2.6%
P_{SOL} (MW)	100	100
Outer flux exp.	2.6	7.3
Outer DI	1.07	1.76
Outer conn. length (m)	86.1	128.1

Table 4: The attributes of the ITER SD and ITER perturbative XD are compared. The ITER XD sees a significant increase in flux expansion and flaring at the outboard target, but at the loss of some plasma volume, and an increase in elongation. The outer connection length is also greatly increased.

It is remarkable that we've been able to encourage significant flux expansion at the divertor targets without requiring any changes to the ITER hardware, but by simply rearranging the current distribution in the existing coil set. However, as we've previously alluded, poloidal flux expansion may actually serve to decrease the plasma-wetted area, due to the staggered target tiles. Our primary interest is in the benefits of flux tube flaring at the outboard target that the XD brings. While a *DI* of 1.76 may be underwhelming, it may be sufficient to enable the outboard divertor leg to come closer to detachment, which is the real goal. If the plasma current is reduced from 15 MA to 14 MA, slightly easing the PF and CS coil current burden and bringing the secondary x-point closer, *DI* can go up to 2.07. From our initial results in C-Mod, this gives us cause to hope that even mild XDs can open windows to stable detachment.

Unfortunately, due to the wide range of particle fluxes in ITER, spanning several orders of magnitude, SOLPS runs to model detachment take several months to converge. Heat transport results for the ITER XDs discussed here will be the subject of a future publication. At the onset, at least, we have reason for optimism that an XD experiment can be performed on ITER in its current incarnation, bolstered by the experimental results of smaller tokamaks like NSTX-U and C-Mod. If successful, access to higher degrees of detachment may go to great lengths to alleviate higher heat fluxes in ITER.

While these initial results in CORSICA and B2.5-Eirene for the XD and SXD are certainly encouraging, they must be continually refined to account for several ambiguities in the true tokamak environment.

As far as the magnetic equilibrium is concerned, while coil current limits have been observed, specifications on allowed magnetic forces between coils are not yet available. The stresses each coil induces on the others must be analyzed. For inductive plasmas, which rely on the central solenoid for driving a plasma current, it is important that the total magnetic flux through the solenoid remain roughly consistent.

As there is a clear emphasis on the outboard leg in X-Divertors and Super X-Divertors, we must make certain that power balance between the inboard and outboard legs is accurate. Aside from controlling the total SOL power via the core boundary condition, a ballooning factor can be introduced to preferentially send power to the inboard or outboard leg. Of course, the validity of this factor will only be corroborated in as much as it yields the experimentally observed power load ratio at the targets. After this correction, it could very well turn out that the inboard target develops the stronger heat

flux problem. The same problem could arise if flux expansion at the outboard target causes the SOL power load to shift preferentially to the inboard target. As the magnetic geometry itself of the advanced divertor may cause this phenomenon, it is critical that we first have a vetted standard divertor by which to determine an appropriate ballooning factor.

Furthermore, per the previous discussions in Sections 6.1 and 6.2, our given target heat flux results may be made more optimistic by our choice of flux limit factor and by our use of impurities, respectively. As previously stated, it's important that a parameter scan on flux limits be performed to assess how they affect target profiles. To properly account for radiation loads on the targets, a separate radiation calculation must be performed. Depending on the desired level of sophistication – including reflections and shadowing structures – this can be a complicated calculation.

Nevertheless, these initial results enthusiastically motivate research into all of these factors, as the XD and SXD have thus far shown remarkable resilience to heavy power loads and narrow SOL widths.

V. FINAL REMARKS

Even from the preliminary results presented in this dissertation, it seems clear that the X-Divertor and the Super X-Divertor hold great promise in not only expanding the area over which exhaust heat is deposited on the tokamak wall, but actually isolating the exhaust plasma from the wall entirely via flux tube flaring. Not only that, but XDs appear to be feasible on several existing tokamaks without requiring *any* changes to their hardware. That an advanced divertor like the XD can be created on a PF coil system for which it was never intended speaks to the versatility of the XD; that is perhaps the type of fortuitous discovery unseen since the H-mode was first stumbled upon.

It also speaks to how far we've come in our own understanding of advanced divertors, including how they're created, and how best to implement them. Advanced divertors like XDs can be made perturbatively from standard divertors, they can be made with reasonable coil currents, and their true worth may lie in flux tube flaring, not mere flux expansion at the divertor targets. If we take the time to appreciate the nuances of magnetic geometries now, we'll be in a better position to intelligently design the next generation of PF coil systems for flexibility.

All promise aside, the results presented in this work represent a beginning, not an end. XDs and SXDs need to be explored in CORSICA on as many working tokamaks as possible, to build a widespread knowledge base. Their results need to be compared directly with vetted standard divertor equilibria, requiring that the facilities that house these tokamaks collaborate closely. Hurdles in the mesh generation of Snowflakes need to be overcome so that the concept of the Divertor Index can be explored between advanced divertors of high contrast.

There are several improvements to be made to the numerical models as well. In CORSICA, our magnetic equilibria so far are exactly that – equilibria. Now that we are confident that the transition from SD to XD to SXD is continuous, time-dependent scenarios for the PF coils need to be developed to make that transition. Forces on the coils, changes in magnetic flux, power supply limitations – these are all factors that could cause complications in advanced divertor formation. Sensitivity studies need to be performed to test the relative resilience of advanced divertors to unexpected spikes in the plasma current. MHD stability studies need to be performed to analyze the types of modes that may be encouraged to propagate with advanced divertors.

SOLPS is another major source of model refinement. Code version alone is a point of some concern right now, with some versions of SOLPS having new physics that others don't, and vice versa. Once ballooning and power balance are decided upon, the heat transport results of B2.5-Eirene need to be checked for consistency with some appropriate power SOL width formula. Early results suggest that the XD and SXD can indeed slow the migration of the detachment front compared to the standard divertor, but to what degree? An empirical relationship between Divertor Index and the stability of the detachment front, if one indeed exists, needs to be established. One major expectation of detachment is that the total pressure along a field line will develop gradients as one crosses from the MHD regime to the neutral regime at the detachment front. This too needs to be established.

Other points of high interest not explored in this dissertation include helium pumping and ELM mitigation. If detachment can be arrested in an XD or SXD, then helium pumping efficiency is expected to improve dramatically, since neutral gas pressures near the targets will be high. We've already seen how XDs and SXDs can handle steady-state heat fluxes; perhaps they can also mitigate the transient heat fluxes of

ELMS as well. Fortunately, these studies need not be relegated to computational modeling alone. If the C-Mod and NSTX-U X-Divertor designs prove feasible, then they can test their meddle on the tokamaks directly. The MAST spherical tokamak at Culham is already incorporating SXD coils as part of its upgrade [29], so there are many potential experiments on the horizon by which to benchmark our numerical models.

It is truly exciting to be at the forefront of a possible solution to a problem as serious as the divertor "bottleneck" is to fusion energy. An advanced divertor may become to fusion energy what fusion energy is to energy policy; that is, it may be unfamiliar, as of yet unproven, and more complex than other options, but in light of the problems we face, we may soon find that it's the only option on the table actually poised to handle them. A day may come when we need fusion energy to move civilization forward; if so, another day much sooner may come when we need advanced divertors to move fusion forward.

Appendix A – The Motivation for Magnetic Confinement Fusion

A.1 The pursuit of fusion energy

Since the 1950s, there has been a conscious, international effort to harness the power of fusion, the nuclear process which powers the sun. Fundamentally opposite from its well-known analog, nuclear fission, fusion is the process by which the nuclei of two atoms combine, which can, counterintuitively, release a very large amount of energy per reacting nucleon. As with fission, this is readily explained by Einstein's famous energy-mass relation, $E = mc^2$. Careful measurement of the masses of the initial reacting nuclei and their final product nucleus in a fusion reaction reveal that, in fact, the larger product nucleus is *less* massive than the combined masses of its constituent nuclei. In this case, it would seem that the product is less than the sum of its parts. We are left to conclude, then, that the missing mass was converted into energy. It is the coveted goal of all nuclear power systems – both fission and fusion alike – to capture and use this free energy, albeit by very different means.

So if the splitting of heavy elements like uranium and plutonium via fission is well understood, and the technology to harness this process is already developed and available, what motivates further pursuit of a solution to the much more complex problem of combining the lightest elements, like hydrogen, via fusion? This question is of particular importance when considering that fission is a spontaneous process, merely needing to be concentrated and harnessed. Fusion, however, with its low reaction cross-section, requires significant reactant density and input energy for the nuclei to overcome the usually dominant electrostatic repulsion of their like charges.

The answer lies with the numerous attractive, practically utopian benefits that widespread fusion energy would afford us, benefits which often present themselves in stark contrast to the infamous drawbacks of fission:

1. While the amount of nuclear binding energy released per fusion reaction is actually smaller than a typical fission reaction, the amount of energy per mass of the reactant nucleons is many times greater. That is, the mass of fusion fuel (such as hydrogen isotopes like deuterium and tritium) one requires is a small fraction of the mass of fission fuel (such as uranium) needed to yield the same amount of energy. Practically speaking, this means that an entire city powered by efficient fusion energy could run on just grams of hydrogen per year, a staggering simplification of resource management. It's worth noting that while the point here focuses on the superior energy density of fusion over fission, both types of nuclear power are far more energy-dense than any type of fossil fuel energy source, the workhorse of the world today.

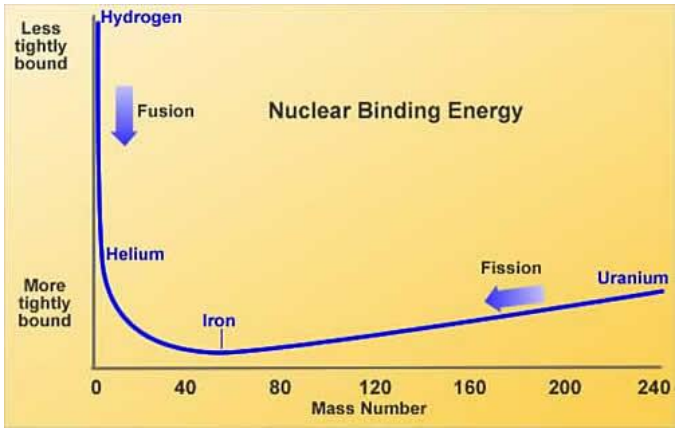

Figure A1: Isotopes lighter than Fe-56 can undergo fusion, while isotopes heavier than Fe-56 can undergo fission. The nuclear binding energy released per nucleon mass in the fusing of two hydrogen nuclei to form helium is much greater than the energy per mass released in any fission reaction. Figure courtesy of the EFDA [30].

2. As with fission, nuclear fusion has no air-polluting by-products. This, of course, is a major drawback to fossil fuel energy sources, and it is thought to be responsible for thousands of chronic respiratory diseases and deaths each year. Nuclear reactions in general avoid this problem because their products are not a result of chemical processes like combustion.
3. Nuclear reactions do, however, suffer from a different kind of waste problem, that of radioactive by-products. This waste is not only dangerous because its radiation can cause illness, but also because it can activate other inert matter, turning it radioactive as well. In the case of typical, high-Z fission waste products, this radioactivity can persist for thousands of years, creating great uncertainty in the waste's safe, long-term storage. By contrast, the deuterium-tritium (D-T) fusion reaction, the most easily attainable fusion reaction within laboratory plasma temperature range, creates no radioactive waste products, requiring only that the neutron

radiation from the reaction itself be mitigated with shielding. In fact, the only long-term radioactive substance present is the reactant tritium, which has a relatively short half-life of 12.3 years.

4. Because of the relative abundance and widespread availability of the hydrogen isotope deuterium in ordinary seawater, there is easily enough fuel to produce clean fusion energy for thousands if not tens of thousands of years. Thus, fusion resources would not be relegated to a few scarce locations for the benefit of only a portion of the global population; fusion technology would benefit all. Looking even further in the future, fusion technology would also be vital for deep-space exploration and colonization, given that it is estimated that nearly three-quarters by mass of the known matter in the universe is hydrogen.
5. Ironically, the very trait that makes fusion more difficult to achieve makes it far safer as a technology, compared to fission. The spontaneous nature of fission reactions, and thus their ability to chain-react, is what can lead to meltdown scenarios, in which the fissile fuel has become so hot that it melts uncontrollably and contaminates areas outside the reactor. This is the reason that cooling systems are so critical to fission safety; the reaction within the fuel takes place regardless of the state of the system. Fusion, by contrast, requires active heating to initiate, and, beyond the point of a self-sustained reaction, active fueling as well. Thus, the chance of a runaway fusion reaction is exactly *zero*. In the event of a catastrophic system failure, the reaction would simply stop, due to insufficient heating or fuel. Containment and cleanup of any mildly radioactive materials would thus be limited to the materials present at the time of the system failure.

6. Fusion energy technologies are wholly different from fusion weapon technologies, making discernment between the two unequivocal. Any nation could pursue a peaceful fusion energy program under the observation of the International Atomic Energy Authority (IAEA) without concern that the true motives were to build a weapon. By contrast, the process to enrich fissile material for a fission reactor is identical to that which creates material for a bomb, making the objective of fission programs more ambiguous.
7. While it is in many ways as ecologically friendly as "green" sources like wind and solar energy, nuclear fusion can guarantee base load power production in a way that wind and solar currently cannot. Fusion technology is not subject to external conditions that can affect its reliability to supply electricity.

Fusion research can thus be characterized as requiring considerable scientific and technological effort, but offering great rewards for society in return. In many ways, the debate over how to invest in our energy future becomes moot when we consider the dwindling supply of obtainable fossil fuels, anthropogenic climate change, limited fissile fuel, rapidly growing global demand for base load power, and the eventual need for space travel. Difficult or not, nuclear fusion is the only energy source on the horizon that can address all of these concerns.

A.2. Fusion Technology and Performance

Having properly motivated the pursuit of fusion over other sources of energy, we can examine the technologies developed over the last 60 years by which the achievement

of fusion is most promising. As the fusion of the nuclei of two atoms is probabilistic in nature, it is the necessary goal of fusion technology to make the odds sufficiently high so as to see a steady fusion process for an economical expenditure of effort. Unfortunately, as previously mentioned, the cross-section for a fusion event is relatively low. Intuitively, one can envision three ways to improve the odds for fusion: increasing the energy with which nuclei collide (temperature, T), increasing the number of collision events in a given volume (density, n), or increasing the time the energy stays in the entire system of nuclei (energy confinement time, τ_E). The product of these three quantities is known simply as the fusion triple product:

$$Triple\ product\ =\ nT\tau_E \tag{A1}$$

The triple product is the basis for characterizing *all* thermonuclear fusion technologies, no matter how different their mechanisms of operation. Some methods rely on pushing the fusion fuel to extreme densities only for a few nanoseconds, while other methods aim to confine the fuel at sparse density for minutes at a time. Either way, the triple product is the paramount figure of merit when pursuing conditions for fusion reactions – hotter, denser, longer.

It should be readily understood that, because the objective of fusion is for positively charged nuclei to overcome their electrostatic repulsion and fuse, the nuclei will have to have tremendous thermal kinetic energy, and thus the state of matter of the fuel *en masse* will always be that of a plasma. This is certainly the case for the sun, our solar system's natural fusion power plant. Achieving fusion then becomes synonymous with efficiently confining a hot, dense plasma for a sufficient period of time so that enough of its constituent atoms' nuclei fuse and release energy. Thus, most fusion

technology designs are described by their means of plasma confinement. Unfortunately, natural stellar fusion is unreproducible on Earth. The enormous mass of a star is enough to confine its plasma gravitationally at very high densities (~10^{32} m^{-3}), but gravity is far too weak an attractive force for laboratory-size plasmas. Moreover, nuclei in the sun can be confined for many years, a benefit which is also unattainable for a man-made reactor. Consequently, according to the triple product, a fusion reactor plasma must be significantly hotter than a solar plasma – near 100,000,000 K [31]– a fact that presents a great challenge to plasma heating.

Of course, one's choice of fusion fuel also greatly determines the rate of fusion reactivity, a rate that is strongly dependent on plasma temperature. It is clear from Fig. A1 that hydrogen fusion has the highest energy gain per nucleon, but that still leaves any permutation of hydrogen's three isotopes – protium (H-1), deuterium (H-2), and tritium (H-3) – from which to choose. As previously alluded, it turns out that the D-T reaction is most favorable to react in the plasma temperature range one can hope to achieve in a reactor, as shown in Fig. A2.

$$ {}_{1}^{2}H + {}_{1}^{3}H \rightarrow {}_{2}^{4}He\ (3.5\ MeV) + {}_{0}^{1}n\ (14.1\ MeV) $$

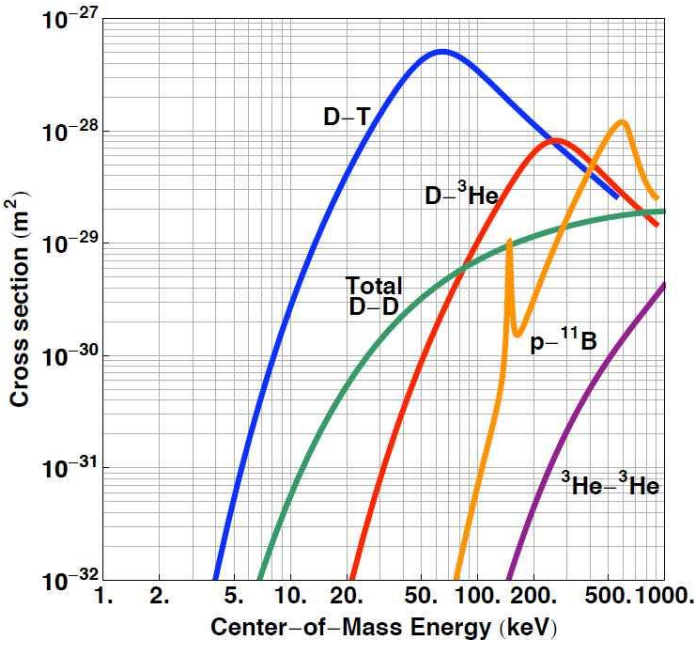

Figure A2: The fusion cross section, a measure of the probability that a fusion reaction will occur between two colliding nuclei, is highest for the D-T reaction at laboratory plasma temperatures [32].

A deuterium nucleus and a tritium nucleus fuse to release a He-4 nucleus at 3.5 MeV and a neutron at 14.1 MeV. The helium nucleus may be interchangeably referred to as an alpha particle, α, in the literature.

While the D-T reaction is the obvious benchmark reaction to achieve, it poses challenges for energy production. For one thing, tritium's short half-life, while beneficial to radiation safety, means that it cannot be found naturally on Earth in reliable quantities. Therefore, tritium breeding must be integrated into the fusion fuel cycle, namely by neutron bombardment of lithium, which is widely available in compound form:

$$^{6}_{3}Li + ^{1}_{0}n \rightarrow ^{3}_{1}H + \alpha$$

$$^{7}_{3}Li + ^{1}_{0}n \rightarrow ^{3}_{1}H + \alpha + ^{1}_{0}n$$

Fortunately, the high-energy neutrons needed to breed tritium are precisely the products of the D-T reaction, so the tritium problem in some sense solves itself: a lithium blanket within the reactor could capture product neutrons and breed tritium. Still, tritium breeding and supply management is very tightly controlled in the scientific community.

The other complication of the D-T reaction is the high-energy neutron itself, which poses challenges both in plasma heating and energy production. Because 80% of the fusion energy produced is the kinetic energy of the neutron (14.1 MeV), none of this energy will be re-deposited back into the plasma for self-heating, as neutrons cannot be confined. Therefore, only the remaining alpha particle can contribute to plasma self-heating, and more external heating will be required. The electric neutrality of neutrons also means that production of actual electricity from their energy is hindered by the same inefficiencies of a standard heat engine. That is, because the neutrons cannot directly draw a current themselves, they must first be absorbed by a blanket for thermal energy, a process which inevitably exhausts waste heat. Energy capture, therefore, becomes another inefficiency in the power economics of the reactor.

Despite these drawbacks, it is logical that the D-T reaction be the first milestone in fusion research, with the understanding that more difficult yet more efficiently harnessed fusion reactions can follow as the technology progresses. For the purposes of this work, any references to fusion power can be implicitly assumed to be a result of the D-T reaction unless otherwise specified.

To summarize, the goal of fusion technology is to create a plasma of fuel whose triple product (and thus reactivity) is high enough such that the fusion power produced is a significant factor times greater than the heating power required to heat the plasma. After all, even if fusion power is produced, if plasma heating proves too costly an

endeavor to produce it, then the technology becomes economically unattractive. A simple measure of fusion economy is the energy gain factor, Q:

$$Q = \frac{P_{fusion}}{P_{heat}} \tag{A2}$$

Where P_{fusion} is the amount of fusion power produced, and P_{heat} is the amount of heating power required by the device to heat the plasma. $Q = 1$ is known as the breakeven point. The upcoming ITER fusion project aspires for $Q = 10$. It is important to note that Q accounts for neither the energy capture efficiency of a real power plant nor the power losses of the plasma confinement system. It is estimated that a practical power plant would require Q to be between 15 and 25.

One could say the "holy grail" of fusion research is to attain a triple product high enough such that the heat from reaction products, such as alpha particles, is sufficient to compensate for the power losses of the plasma; that is, no further external heating is required to keep the plasma ions hot enough to fuse, and the fusion reaction becomes self-sustaining. This condition is known as ignition, and for the D-T reaction, it corresponds to a triple product of order 10^{24} eV·s/m^3 [33], where the temperature has been expressed in units of energy by way of the Boltzmann constant, k_B. From there, the plasma need only be supplied with new fuel and kept confined to continue to generate fusion power. In such a case, Q would effectively be infinite.

This concept is readily understood by analogy. When building a fire, another example of a plasma, it isn't enough to throw wood on a pile and light a match. Considerable, external effort from our primitive plasma physicist is needed to heat the wood for the combustion reaction to take place. Even still, more input energy is needed

before the combustion reaction is widespread enough to heat and burn the wood itself; a small flame will die out just as readily as it appeared. Once the fire reaches a critical threshold of reactivity, it will continue to burn as long as it is supplied fresh fuel, with no further external effort needed. This is the equivalent of fusion ignition.

A.3 MAGNETIC CONFINEMENT AND THE TOKAMAK

For the purposes of this research, we will focus solely on magnetic confinement fusion (MCF) – specifically, the tokamak – as it is one of the most widely studied and developed fusion technologies. To be sure, there is a diversity of fusion technologies across the triple product spectrum currently being studied, not the least of which includes inertial confinement, Z-pinches, magnetic mirrors, levitated dipoles, stellarators, reversed field pinches, and even magneto-inertial confinement. The interested reader can find an abundance of research on each of these confinement schemes.

The MCF method falls into the low-density (currently $\sim 10^{20}$ m^{-3}), high-confinement time (currently ~1 s) region of the triple product spectrum, using strong, closed magnetic fields to tightly confine a plasma long enough for fusion to occur. The plasma responds to this magnetic "bottle" because its constituent parts – free electrons and their associated ions – are charged particles, which execute gyrating orbits around magnetic field lines, restricting their motion (Fig. A3). In this way, the hot fusion plasma may be kept out of physical contact with the much colder vessel wall.

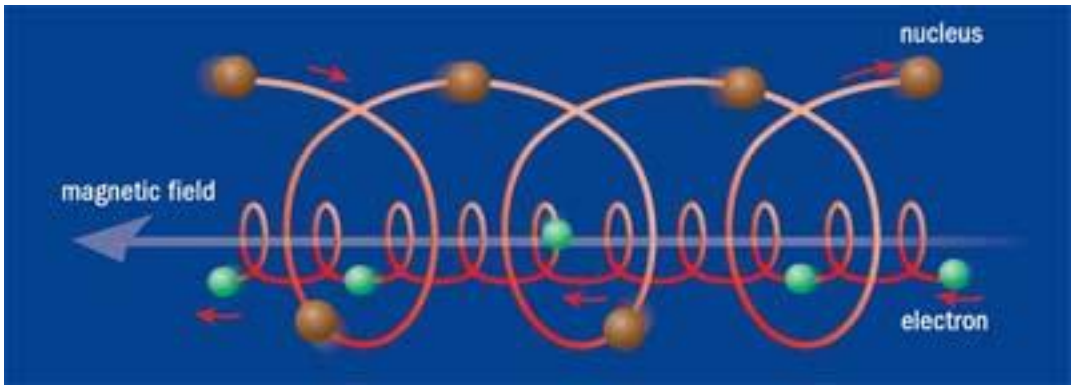

Figure A3: Due to the Lorentz force, the ionized nuclei and the electrons that comprise the plasma execute gyro-orbits around magnetic field lines.

The confinement is not perfect, however, and as experimental observation shows, the interaction between the plasma and the wall greatly affects the performance of an MCF-based device. Due to the collisionality of their electrons and ions, plasmas often exhibit fluid behaviors; the study of fluid-like plasmas under the influence of external magnetic fields, such as those found in MCF, is known as magnetohydrodynamics (MHD).

The tokamak is the most widely used MCF device design to date, due to its relative simplicity of design and demonstrable experimental progress. Its vessel consists of a hollow, axisymmetric torus, inside which plasma is confined along toroidal magnetic field lines. These magnetic field lines are produced by toroidal field (TF) coils, a series of thick, current-carrying conductors that loop around the outside of the torus in the poloidal direction, as in Fig. A4. For the purposes of heating and improved confinement, a toroidal plasma current is also induced, which generates its own poloidal magnetic field. Thus, the superposition of both toroidal and poloidal magnetic components results in helical field lines inside the torus (Fig. A5). Because it is highly beneficial to tokamak performance to

control the cross-sectional shape of the plasma, poloidal field (PF) coils also loop around the outside of the torus in the toroidal direction.

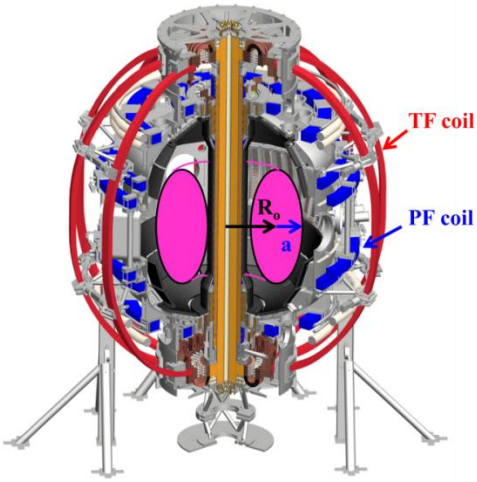

Figure A4: A cutaway of the NSTX tokamak [34]. PF coils, shown in blue, wind in a toroidal direction and produce poloidal magnetic fields. TF coils, shown in red, wind in a poloidal direction and produce toroidal magnetic fields. The distance from the center axis of the tokamak to the center of the plasma is the major radius (R_o), while the distance from the center of the plasma to its edge is the minor radius (a).

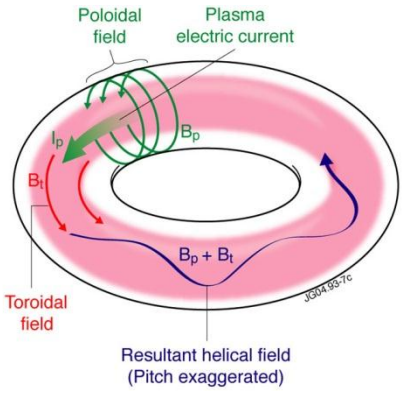

Figure A5: The combination of the poloidal field from the PF coils and the toroidal field from the TF coils creates a helical magnetic field that confines the plasma. Figure courtesy of the EFDA [35].

The radius from the axis of symmetry to the plasma center is known as the plasma major radius, R_o, while the radius of the plasma cross-section in the poloidal plane is the minor radius, a. The aspect ratio A of a tokamak is simply the ratio between these two radii, R_o/a. Typically, the aspect ratio is 2-3, but there is substantial interest in more economical, lower-aspect ratio tokamaks where A is closer to 1. Tokamaks with A approaching 1 are referred to as spherical tokamaks.

Fusion power increases with the square of the plasma pressure, but like any many-particle system, the plasma will expand with increased pressure, P. The external magnetic field must therefore exert its own "pressure," $B^2/2\mu_o$ (where μ_o is the usual permeability of free space), against the plasma. Then the most basic picture of a magnetically confined plasma in equilibrium is that of a force balance between the plasma and its magnetic "bottle." The dimensionless ratio of these two quantities is known as beta:

$$\beta = 2\mu_o \frac{P}{B^2} \tag{A3}$$

Beta is often the primary figure of merit in tokamak confinement efficiency, as it is a snapshot of the plasma pressure achieved for the amount of coil current needed to produce the confining magnetic field, often the costliest aspect of tokamak operation. It is important to note that neither P nor B are constant across the plasma volume, so there are several definitions of β. Usually, P is taken to be $\langle P \rangle$, the volume-averaged pressure of the plasma, and B as $\langle B \rangle$, the volume-averaged total magnetic field strength. However, we may also consider β_T and β_P, in which the total magnetic field is replaced by only the toroidal or poloidal components, respectively. Moreover, β is often normalized by the

plasma current I_P to give an indication of how close the plasma is to reaching the Greenwald density limit, n_G, the limit past which a plasma disruption is likely to occur:

$$\beta_N = \frac{aB}{I_P}\beta \tag{A4}$$

We have now established the first principles of plasma confinement, and we have identified the major figures of merit of fusion performance and economic attractiveness: the triple product and Q. The remainder of this study will revolve specifically around magnetic confinement and the tokamak. Accordingly, we introduced an additional figure of merit, β, as a measure of the efficiency with which a tokamak plasma is confined magnetically. It is clear from our knowledge of magnetic confinement and the fusion triple product that a tokamak plasma will have to be maintained for at least several seconds to yield significant fusion power, making it susceptible to a host of instabilities, disruptive events, power losses, and interactions with the plasma-facing walls.

It is this last complication of tokamak physics that will be the main thrust of this dissertation. Because of the extremely varied environments inside tokamaks, it is imperative that interactions between the super-hot plasma and the room-temperature wall be minimized, lest the plasma be cooled and the wall be damaged. As the fusion triple product is pushed further, this problem becomes less trivial, both scientifically and technologically.

Appendix B – Derivation of the Grad-Shafranov Equation

Stable magnetic equilibria balance the forces of the outward plasma pressure gradient and the confining magnetic field:

$$\nabla P = \vec{J} \times \vec{B} \tag{B1}$$

Formulations for axisymmetric tokamaks are elegantly expressed in cylindrical coordinates, *(R,z,φ)*, where *R* and *z* are rectangular coordinates in the poloidal plane, and φ is the toroidal coordinate. We begin the derivation of our mathematical foundation by evaluating the right hand side of Eq. B1, breaking up $\vec{J}$ and $\vec{B}$ into their toroidal and poloidal components:

$$\vec{J} \times \vec{B} = \left(\vec{J}_P + \vec{J}_T\right) \times \left(\vec{B}_P + \vec{B}_T\right) = \vec{J}_P \times \vec{B}_T + \vec{J}_T \times \vec{B}_P \tag{B2}$$

With the understanding that $\vec{J}_T \times \vec{B}_T = 0$ identically, and $\vec{J}_P \times \vec{B}_P$ must equal 0 to satisfy toroidal symmetry, as there can be no toroidal component of ∇P to balance this term. We pause now in our derivation to find appropriate substitutions for the components of $\vec{J}$ and $\vec{B}$. Starting with $\vec{B}$, we use the magnetic vector potential:

$$\vec{B} = \nabla \times \vec{A} = -\frac{\partial A_T}{\partial z}\hat{R} + \frac{1}{R}\frac{\partial}{\partial R}(RA_T)\hat{z} + B_T\hat{\varphi} \tag{9}$$

Where the R- and z-components comprise the poloidal field, and we have chosen to leave the toroidal field simply as $B_T\hat{\varphi}$, knowing *a priori* that it can be handled

separately later. A_T represents the magnitude of the toroidal component of the magnetic vector potential. With some clever algebra, $\vec{B}_P$ can be rewritten compactly as:

$$\begin{aligned}\vec{B}_P &= -\frac{\partial A_T}{\partial z}\hat{R} + \frac{1}{R}\frac{\partial}{\partial R}(RA_T)\hat{z} \\ &= \frac{1}{R}\left[-\frac{\partial}{\partial z}(RA_T)\hat{R} + \frac{\partial}{\partial R}(RA_T)\hat{z}\right] \\ &= \frac{1}{R}\left(-\frac{\partial \psi}{\partial z}\hat{R} + \frac{\partial \psi}{\partial R}\hat{z}\right) \\ &= \frac{1}{R}\nabla\psi \times \hat{\varphi}\end{aligned} \tag{B3}$$

Where we have defined the scalar function $\psi \equiv RA_T$. From this simplification, it is clear that $\vec{B}_P$ is everywhere perpendicular to $\boldsymbol{\nabla}\psi$; ψ therefore is an appropriate stream function for the poloidal field. This is a very valuable simplification of the representation of the poloidal field. The total field is now written as:

$$\vec{B} = \frac{1}{R}\nabla\psi \times \hat{\varphi} + B_T\hat{\varphi} \tag{B4}$$

Moreover, as previously noted, $\boldsymbol{\nabla}$P is perpendicular to $\vec{B}_P$, and P is constant along any given field line, so it follows that P is an explicit function of ψ, $P(\psi)$.

Using Ampere's Law, it is then straightforward to derive a similar substitution for $\vec{J}$. We are justified in using the magnetostatic version of the law because we seek steady-state equilibria (i.e., $d/dt \rightarrow 0$):

$$\begin{aligned}\vec{J} &= \frac{1}{\mu_o}\nabla \times \vec{B} \\ &= \frac{1}{\mu_o}\left[\nabla \times \left(\frac{1}{R}\nabla\psi \times \hat{\varphi}\right) + \nabla \times B_T\hat{\varphi}\right]\end{aligned}$$

$$= \frac{1}{\mu_o}\left[\left(-\nabla\cdot\frac{1}{R}\nabla\psi\right)\hat{\varphi} + \frac{1}{R}\nabla(RB_T)\times\hat{\varphi}\right] \tag{B5}$$

It is clear that the first term is $\vec{J}_T$, and the second term is $\vec{J}_P$. And once again, we find from our previous observation that because ∇P must be perpendicular to $\vec{J}_P$, and P is an explicit function of ψ, then the scalar function RB_T must also be an explicit function of ψ, $F(\psi)$. Having now found appropriate substitutions for $\vec{J}$ and $\vec{B}$, we continue our evaluation of the right-hand side of Eq. B2, enforcing toroidal symmetry along the way to eliminate terms:

$$\begin{aligned}\vec{J}\times\vec{B} &= \frac{1}{\mu_o}\left[\left(\frac{1}{R}\nabla\mathrm{F}\times\hat{\varphi}\right)\times B_T\hat{\varphi} - \left(\nabla\cdot\frac{1}{R}\nabla\psi\right)\hat{\varphi}\times\left(\frac{1}{R}\nabla\psi\times\hat{\varphi}\right)\right] \\ &= \frac{1}{\mu_o R}\left[-B_T\nabla\mathrm{F} - \left(\nabla\cdot\frac{1}{R}\nabla\psi\right)\nabla\psi\right]\end{aligned} \tag{B6}$$

Now a change of variables is justified to write $F(\psi)$ in terms of $\nabla\psi$. We can treat ∇P on the left-hand side of Eq. B1 similarly, meaning that all vectors ultimately drop out entirely, and we arrive at the Grad-Shafranov equation (Eq. B7):

$$\begin{aligned}\frac{dP}{d\psi}\nabla\psi &= -\frac{1}{\mu_o R}\left[B_T\frac{dF}{d\psi} + \left(\nabla\cdot\frac{1}{R}\nabla\psi\right)\right]\nabla\psi \\ -\mu_o R\frac{dP}{d\psi} &= \left[B_T\frac{dF}{d\psi} + \left(\nabla\cdot\frac{1}{R}\nabla\psi\right)\right] \\ -\mu_o R^2\frac{dP}{d\psi} &= F\frac{dF}{d\psi} + \Delta^*\psi\end{aligned}$$

$$\Delta^*\psi = -\mu_o R^2\frac{dP}{d\psi} - F\frac{dF}{d\psi} \tag{B7}$$

References

[1] S. Fietz et al., "Investigation of transport models in ASDEX Upgrade current ramps," *Nuclear Fusion,* vol. 53.5, 2013.

[2] D. Kacprzak, "Engineering Electromagnetics," University of Auckland, September 2001. [Online]. Available: http://homepages.engineering.auckland.ac.nz/~kacprzak/notes.htm.

[3] F. Wagner et al., "Regime of improved confinement and high beta in neutral-beam-heated divertor discharges of the ASDEX tokamak," *Physical Review Letters,* vol. 49, 1982.

[4] R. Goldston, "Heuristic drift-based model for the power scrape-off width in H-mode tokamaks," in *38th EPS Conference on Plasma Physics*, Strasbourg, France, 2011.

[5] M. Kotschenreuther et al., "Scrape off layer physics for burning plasmas and innovative divertor solutions," in *Proceedings of the 20th International Conference on Fusion Energy*, Vilamoura, Portugal, 2004.

[6] P. Valanju, M. Kotschenreuther and S. Mahajan, "Super-X divertors and high power density fusion devices," *Physics of Plasmas,* vol. 16, 2009.

[7] D. Ryutov, "Geometrical properties of a "snowflake" divertor," *Physics of Plasmas,* vol. 14.6, 2007.

[8] "Spherical Tokamaks," Culham Centre for Fusion Energy, 2012. [Online]. Available: http://www.ccfe.ac.uk/ST.aspx.

[9] P. Knight et al., "Controlled Thermonuclear Fusion: Clean, Safe Energy for the Future," University of Edinburgh, [Online]. Available: http://www.hpcx.ac.uk/highlights/thph1.html.

[10] "Fusion Energy: Magnetic Confinement," Department of Physics, University of York, 2013. [Online]. Available: http://www.york.ac.uk/physics/postgraduate/researchprojects/current-research-projects/plasmaphysics/fusionplasmas/.

[11] R. Nave, "Magnetic Field of Toroid," Hyperphysics, Georgia State University, [Online]. Available: http://hyperphysics.phy-astr.gsu.edu/hbase/magnetic/toroid.html.

[12] M. Kotschenreuther, "Magnetic geometry and physics of advanced divertors: the X-Divertor and the Snowflake," *Physics of Plasmas,* vol. 20, 2013.

[13] L. Schmitz et al., "Reduced electron thermal transport in low collisionality H-mode plasmas in DIII-D and the importance of TEM/ETG-scale turbulence," *Nuclear Fusion,* vol. 52.2, 2012.

[14] D. Coster et al., "SOLPS 5.0," 2010.

[15] A. Teller, "The Strange Controversy Surrounding ITER," ENS News, January 2007. [Online]. Available: https://www.euronuclear.org/e-news/e-news-15/listening.htm.

[16] J. Crotinger et al., "CORSICA: A Comprehensive Simulation of Magnetic Toroidal-

Fusion Devices," 1997.

[17] S. Wiesen et al., "The new SOLPS-ITER code package," 2014.

[18] "LONESTAR," Texas Advanced Computing Center, 2013. [Online]. Available: https://www.tacc.utexas.edu/resources/hpc/lonestar.

[19] K. Lackner and H. Zohm, "Calculation of realistic snowflake equilibria for next-step devices," *Fusion Science and Technology,* vol. 63.1, 2013.

[20] J. Menard et al., "Overview of the physics and engineering design of NSTX upgrade," *Nuclear Fusion,* vol. 52, 2012.

[21] "Timeline," Princeton Plasma Physics Laboratory, 2014. [Online]. Available: http://www.pppl.gov/about/history/timeline.

[22] S. Gerhardt, R. Andre and J. Menard, "Exploration of the equilibrium operating space for NSTX-U," *Nuclear Fusion,* vol. 52, 2012.

[23] "Alcator C-Mod," [Online]. Available: http://www.fusionfuture.org/world-fusion-experiments/about-alcator-c-mod/.

[24] S. Wolfe, Interviewee, [Interview]. May 2014.

[25] "Press Release Gallery," The ITER Organization, 2011. [Online]. Available: https://www.iter.org/gallery/com_image_download#397.

[26] C. Kessel, Interviewee, [Interview]. 2013.

[27] R. Pitts, Interviewee, [Interview]. 2013.

[28] E. Doyle et al., "Progress in the ITER physics basis chapter 2: plasma confinement and transport," *Nuclear Fusion,* vol. 47, 2007.

[29] S. Lisgo et al., "Super-X advanced divertor design for MAST upgrade," in *36th EPS Plasma Physics Conference*, Sofia, Bulgaria, 2009.

[30] "FAQs," [Online]. Available: http://www.efda.org/faq/how-is-it-that-both-fission-and-fusion-produce-power-if-splitting-a-large-atom-into-two-smaller-atoms-releases-energy-it-seems-that-combining-two-smaller-atoms-into-one-larger-atom-would-require-ene/.

[31] "The Tokamak," Culham Centre for Fusion Energy, 2012. [Online]. Available: http://www.ccfe.ac.uk/Tokamak.aspx.

[32] "Inertial Electrostatic Confinement Fusion," University of Wisconsin-Madison, 2012. [Online]. Available: http://iec.neep.wisc.edu/operation.php.

[33] "Lawson's Three Criteria," EFDA, [Online]. Available: http://www.efda.org/2013/02/triple-product/.

[34] Princeton Plasma Physics Laboratory, [Online]. Available: http://surface.pppl.gov/images/NSTX.png.

[35] "Ohmic Heating," EFDA, [Online]. Available: http://www.efda.org/fusion/focus-on/plasma-heating-current-drive/ohmic-heating/.